

Collected figures from HELIOPHYSICS III.
EVOLVING SOLAR ACTIVITY AND THE
CLIMATES OF SPACE AND EARTH

edited by
CAROLUS J. SCHRIJVER
Lockheed Martin Advanced Technology Center
and
GEORGE L. SISCOE
Boston University

*This document contains the figures from the published volume of Helio-
physics III as submitted to Cambridge University Press, prior to possible re-
visions in the graphics and captions during the copy editing process. This
collection is intended only as an aid to students and teachers for use in, e.g.,
lectures and study sessions.*

Contents

1	Interconnectedness in heliophysics	<i>page 1</i>
	<i>Carolus J. Schrijver and George L. Siscoe</i>	
2	Long-term evolution of magnetic activity of Sun-like stars	4
	<i>Carolus J. Schrijver</i>	
3	Formation and early evolution of stars and proto-planetary disks	21
	<i>Lee W. Hartmann</i>	
4	Planetary habitability on astronomical time scales	38
	<i>Donald E. Brownlee</i>	
5	Solar internal flows and dynamo action	45
	<i>Mark S. Miesch</i>	
6	Modeling solar and stellar dynamos	51
	<i>Paul Charbonneau</i>	
7	Planetary fields and dynamos	62
	<i>Ulrich R. Christensen</i>	
8	The structure and evolution of the 3D solar wind	73
	<i>John T. Gosling</i>	
9	The heliosphere and cosmic rays	90
	<i>J. R. Jokipii</i>	
10	Solar spectral irradiance: measurements and models	103
	<i>Judith L. Lean and Thomas N. Woods</i>	

11	Astrophysical influences on planetary climate systems	118
	<i>Jürg Beer</i>	
12	Assessing the Sun-climate relationship in paleoclimate records	137
	<i>Thomas J. Crowley</i>	
13	Ionospheres of the terrestrial planets	150
	<i>Stanley C. Solomon</i>	
14	Long-term evolution of the geospace climate	157
	<i>Jan J. Sojka</i>	
15	Waves and transport processes in atmospheres and oceans	173
	<i>Richard L. Walterscheid</i>	
16	Solar variability, climate, and atmospheric photochemistry	194
	<i>Guy P. Brasseur, Daniel Marsch, and Hauke Schmidt</i>	

1

Interconnectedness in heliophysics

Carolus J. Schrijver and George L. Siscoe

Interconnectedness in heliophysics

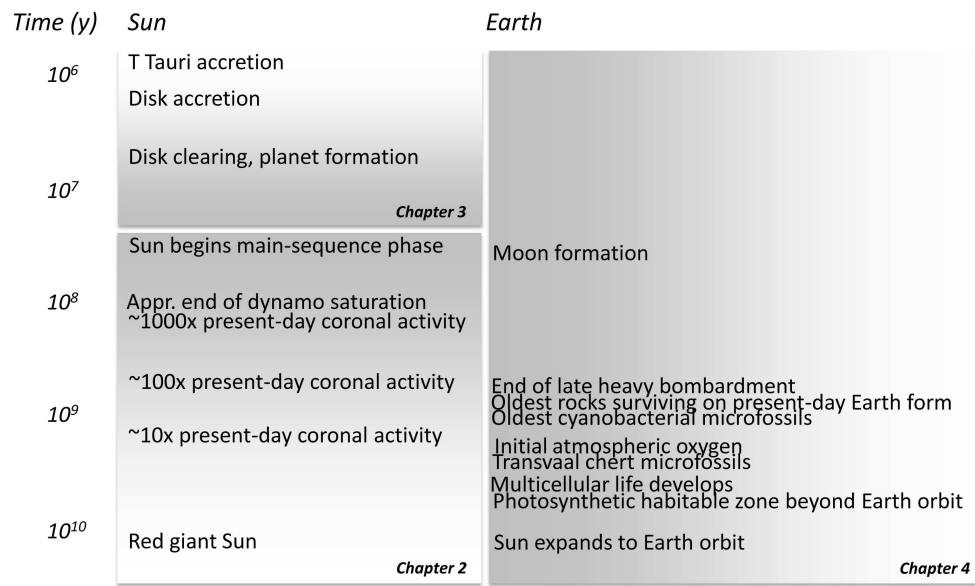


Fig. 1.1. Key events in the history of Sun and Earth, pointing to the chapters in this volume in which these are discussed.

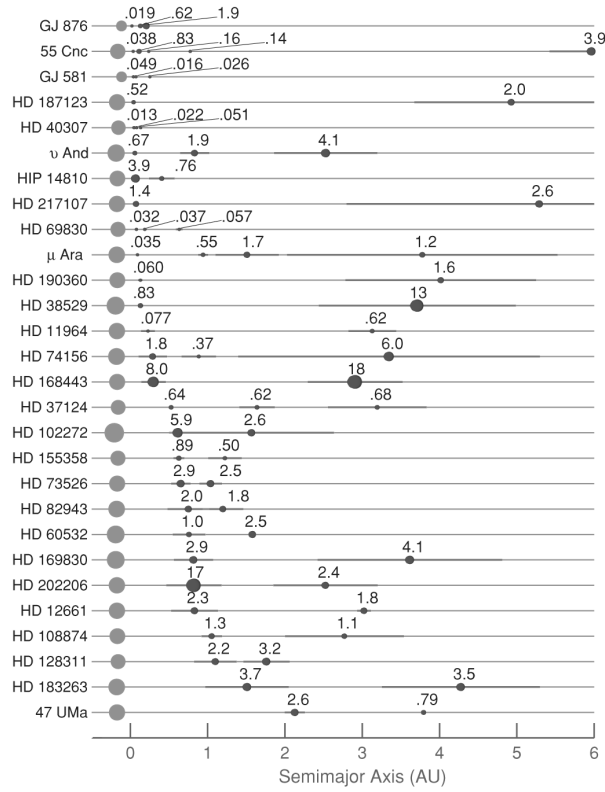


Fig. 1.2. Of some three hundred known planetary systems by 2009, at least $\approx 30\%$ are known to contain more than one planet. This diagram shows the semimajor axes (relative to the radius of the Earth's orbit around the Sun) and minimum masses (in units of Jupiter masses) for the planets in multiplanet systems. The diameters of the symbols for the central stars scale with the cube root of stellar mass. From Wright et al. (2009).

2

**Long-term evolution of magnetic activity
of Sun-like stars**

Carolus J. Schrijver

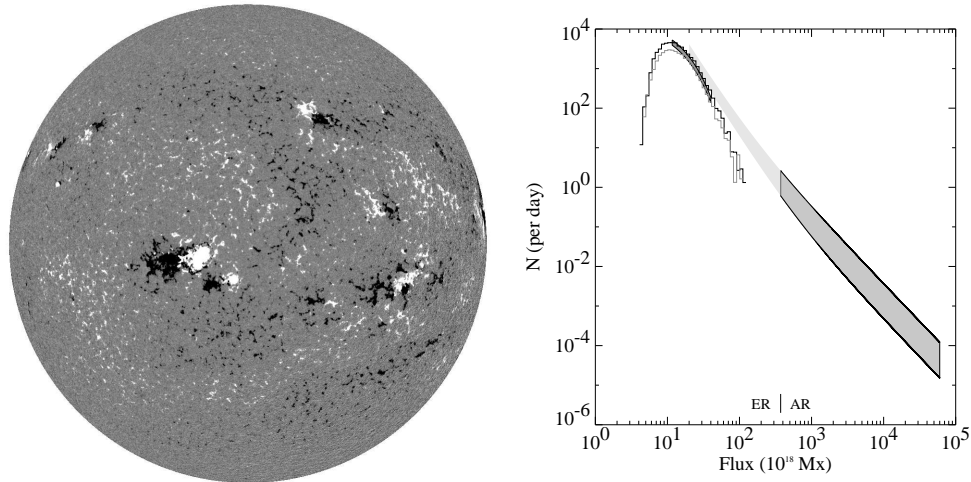


Fig. 2.1. *Left*: First solar magnetic map (magnetogram) of the current millennium, taken by SOHO's MDI on 2001/01/01 00:03 UT. The magnetogram (with white/black for negative/positive line of sight polarity) shows a variety of active regions, embedded in patches of largely unipolar enhanced supergranular network, mixed-polarity quiet Sun regions, and low-flux polar caps (weak at this near-maximum phase of the cycle, and weakened further in the line-of-sight flux map because of center to limb effects). *Right*: Distribution function of emerging magnetic bipolar regions on the Sun, showing the emergence frequency per day per flux interval of 10^{18} Mx, estimated for the entire solar surface. The shaded region on the right envelopes the range of the active-region spectrum for solar cycle 22 (for half-year intervals around sunspot minimum and maximum). The histograms on the left are for the ephemeral regions; the shaded band shows where observations are least affected by spatial (lower cutoff) and temporal (upper cutoff) biases. The spectrum for regions below $\sim 10^{19}$ Mx has yet to be determined; the cutoff here is caused by the limited resolution of the SOHO/MDI magnetograph. Figure from Hagenaar et al. (2003).

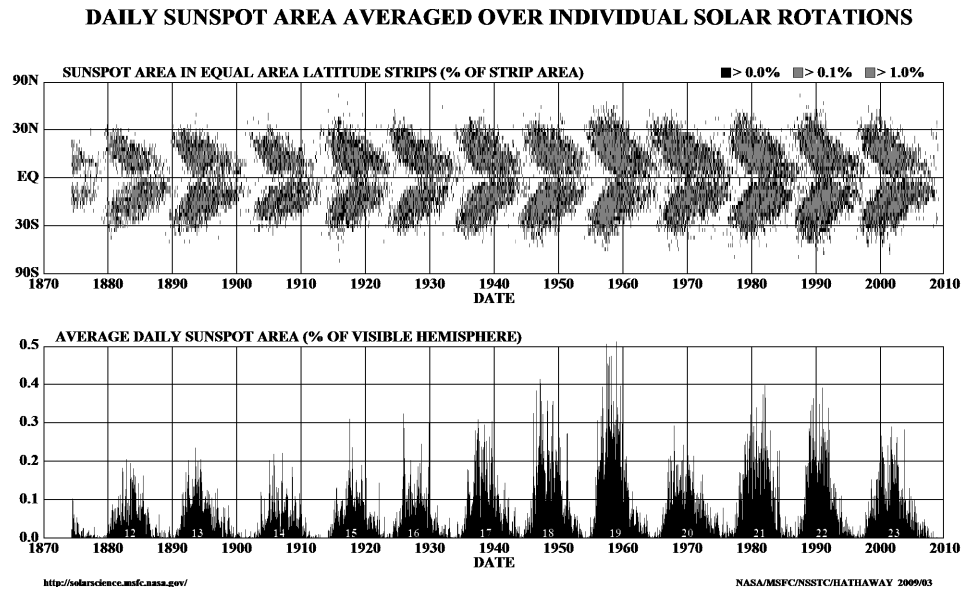


Fig. 2.2. Butterfly diagram showing sunspot latitudes (top) and total fractional area coverage (bottom) as a function time for the last six magnetic cycles. (Figure courtesy of D. Hathaway)

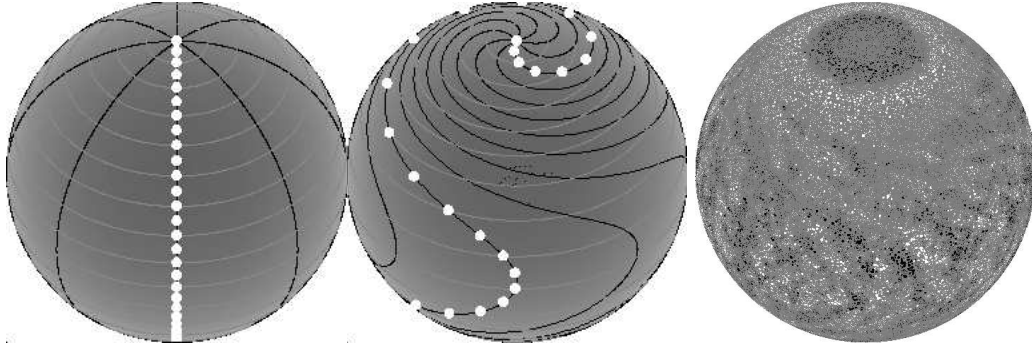


Fig. 2.3. *Left and center:* Visualization of the effects of differential rotation and equator-to-pole meridional flow for Sun-like conditions: lines of equal longitude (with markers) are distorted into a spiral pattern. The center panel shows the distorted lines after 3 months. *Right:* Simulated magnetogram for a star like the Sun, but with an active-region emergence rate 30 times larger, based on the model by Schrijver and Title (2001). The simulated star is shown from a latitude of 40° to better show the polar-cap field structure. Figures from Schrijver (2002).

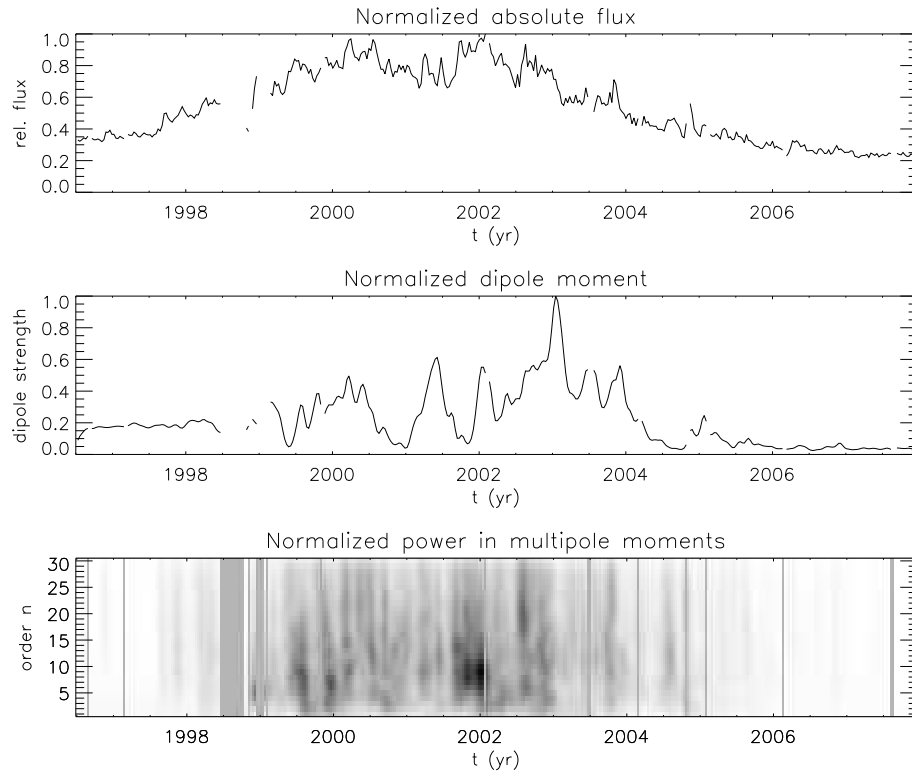


Fig. 2.4. The multipole components of the solar magnetic field. The top panel shows the normalized unsigned magnetic flux on the Sun, and the middle panel shows the strength of the dipole component at the solar surface, each sampled once every 10 days. The curves in these two panels are shown only for those times at which magnetogram data were available. The bottom panel shows the relative power in the multipole components for order n , normalized to the dipole strength ($n \equiv 1$), stronger for darker shading; light gray areas show intervals with missing data. Compare this diagram with Fig. 7.1.

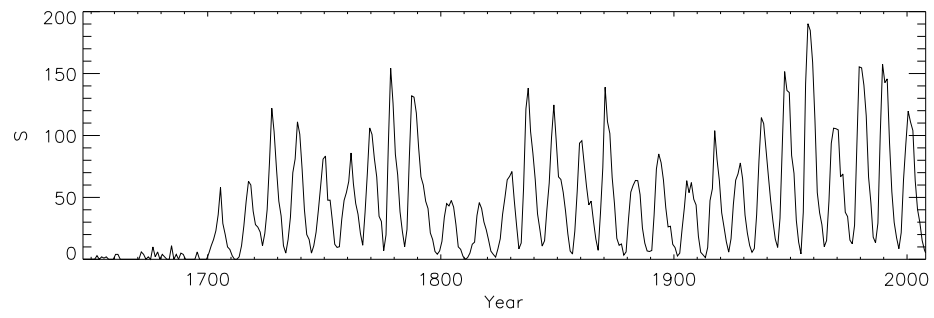


Fig. 2.5. Yearly-averaged sunspot numbers (data from <http://sidc.oma.be/>).

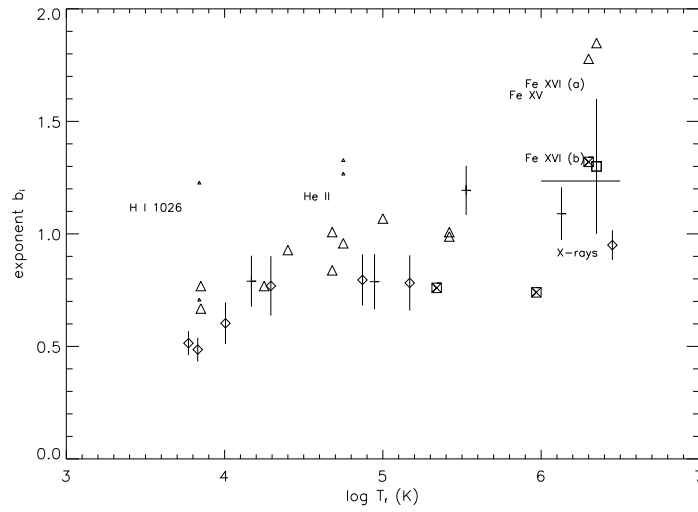


Fig. 2.6. Exponents b_i in the power-law relationships $F_i \propto |\varphi|^{b_i}$ between solar and stellar radiative flux densities and the photospheric magnetic flux density, as a function of the temperature of formation T_i of the radiative diagnostic of stellar magnetic activity. The exponents are derived from data either observed with some angular resolution or disk-averaged for the Sun as a star. Note that the optically-thick H I and He II lines deviate from the pattern formed by the other ions in this diagram. (Figure adapted after Schrijver and Zwaan, 2000, with added data from Fludra and Ireland, 2008)

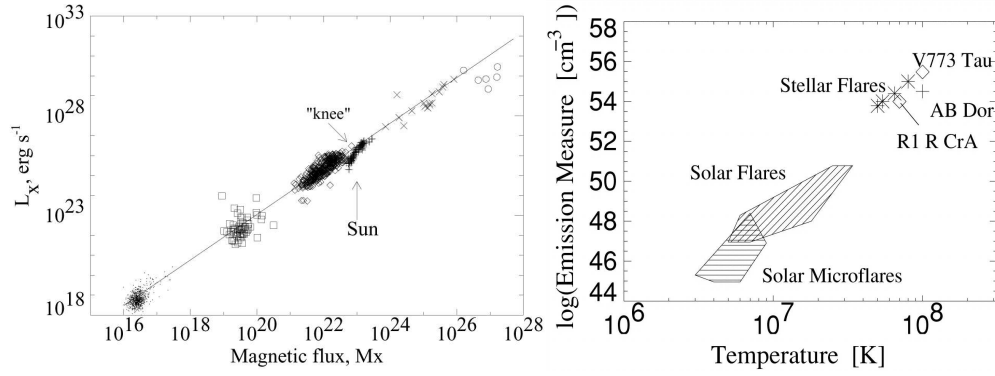


Fig. 2.7. *Left:* X-ray luminosity L_X vs. total unsigned magnetic flux for solar and stellar objects. Dots: quiet Sun. Squares: X-ray bright points (associated with small pairs of opposite polarity in quiet Sun, either over recently emerged ephemeral regions or over chance encounters of concentrations of flux of opposite polarity). Diamonds: solar active regions. Pluses: solar disk averages. Crosses: G, K, and M-type dwarf stars. Circles: T Tauri stars. Solid line: power-law approximation $L_X \propto \Phi^{1.15}$. From Pevtsov et al. (2003). *Right:* Emission measure, EM , versus electron temperature, T , of solar flares and, four stellar flares (asterisks), a proto-stellar flare (diamond), a T Tauri stellar flare (diamond), and a stellar flare on AB Dor (K0 IV zero-age main-sequence single star; plus sign). Figure from Shibata and Yokoyama (2002); see also Fig. 5.13 in Vol. II.

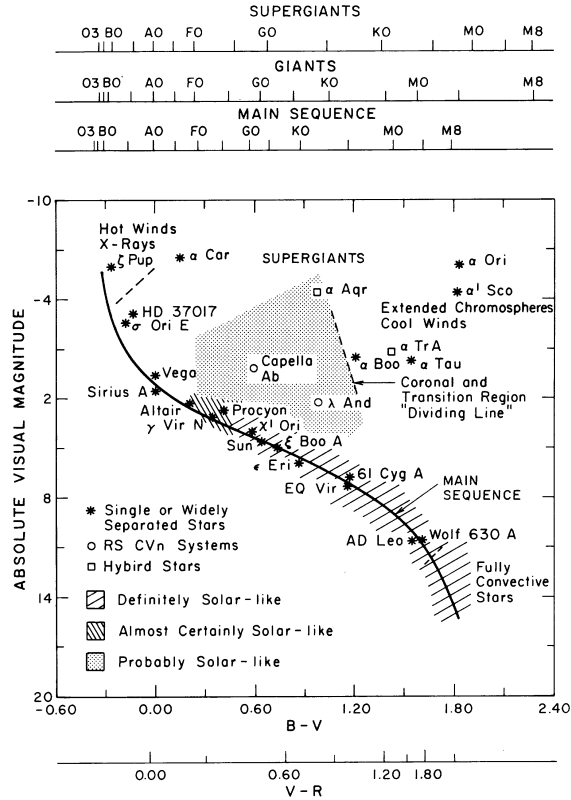


Fig. 2.8. A Hertzsprung-Russell diagram showing stars with substantial magnetic activity in shaded or hatched domains, which are distinguished in groups of solar-likeness as indicated in the legend (by Linsky, 1985). The main sequence where stars spend most of their life time fusing hydrogen into helium in their cores is indicated by a solid curve; well above that lies the domain of the supergiant stars, with the giant star domain in between. Also indicated is the region where massive winds occur and hot coronal plasma is apparently absent. Some frequently studied stars (both magnetically active and nonactive) are identified by name. The axes above the main panel show the spectral types for supergiant, giant, and main-sequence stars for the corresponding spectral color index $B - V$ or corresponding $V - R$ index.

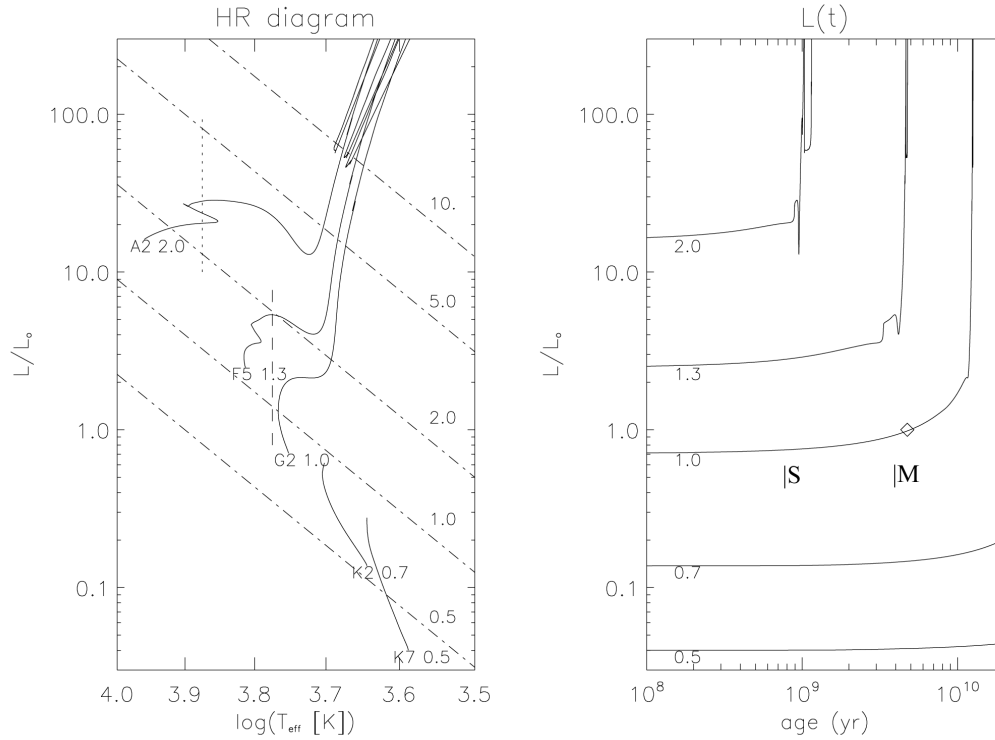


Fig. 2.9. Evolutionary diagrams for luminosity, surface temperature, and age from the mature, main-sequence phase onward. The diagram on the *left* relates the stellar luminosity (in present-day solar units) with the surface effective temperature (K) in a Hertzsprung-Russel diagram (data from Pietrinferni et al., 2004; for an initial helium of $Y = 0.2734$ and 'metal' abundance (i.e., everything heavier than helium) of $Z = 0.0198$). Evolutionary tracks start on the 'zero-age main sequence' (ZAMS), and are labeled with the spectral type on the main sequence and the stellar mass (in solar units). The dashed line segment indicates where dynamo action reaches its full strength; for shallower convective envelopes (warmer stars), the activity level weakens until it has dropped by a factor of 100 at the dotted line segment relative to a Sun-like star at the same angular velocity (from Schrijver, 1993). The slanted dashed-dotted lines indicate stellar radii, with labels in solar units. The diagram on the *right* shows the evolution of the stellar luminosity with stellar age (yr since ZAMS). The diamond shows the present-day Sun (see Fig. 4.5 for details on the Sun's red-giant phase). The approximate ages for which the oldest fossils of single-cell microbial life (S) and multi-cellular plants and animals (M) have been found on Earth are indicated (cf., Ch. 4).

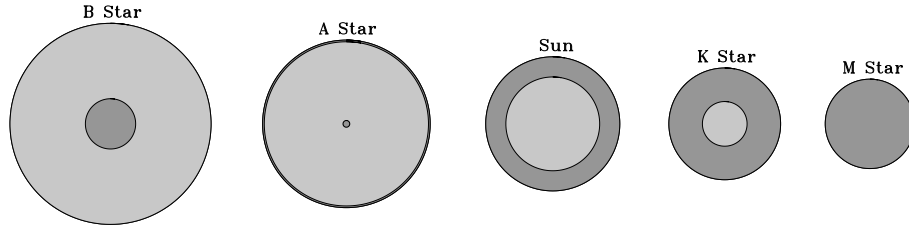


Fig. 2.10. Schematic representation of the radiative (light grey) and convective (dark grey) internal structure of main-sequence stars. The thickness of the outer convection zone for the A-star is here greatly exaggerated; drawn to scale it would be thinner than the black circle delineating the stellar surface on this drawing. Relative stellar sizes are also not to scale: a B0 V star has a radius of $\sim 7.5 R_{\odot}$, and an M0 V star has a radius of $\sim 0.6 R_{\odot}$, i.e., 12 times smaller.

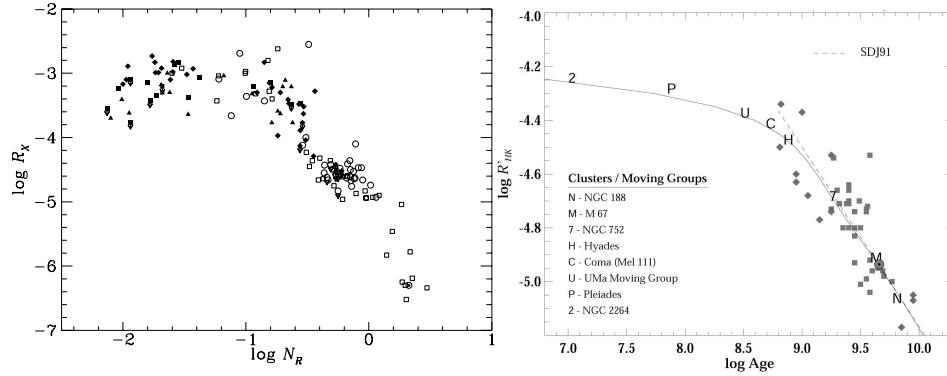


Fig. 2.11. *Left*: Relationship between coronal X-ray emission relative to the stellar luminosity, $R_X = L_X/L_{\text{bol}}$ - shown vertically - and Rossby number $N_R \equiv \mathcal{R}_o$ (Eq. 2.1) - shown horizontally - for F5 through M5 main-sequence stars in four clusters and a selection of field stars. Symbols: filled triangles for IC 2391 (~ 40 Myr), filled squares for α Per (~ 70 Myr), filled diamonds for Pleiades (~ 115 Myr), open circles for Hyades (~ 600 Myr), and open squares for field stars. The Sun (\odot) is located near the low end of the activity measure for the sample of stars in this figure. Figure from Patten and Simon (1996); cluster ages in the figure as in that work, in the caption as updated in the compilation by Denissenkov et al. (2009). *Right*: Activity-age relationship for main-sequence stars for the chromospheric Ca II H,K emission for field stars (diamonds and squares) and average properties for associations of young stars. Figure from Baliunas et al. (1998).

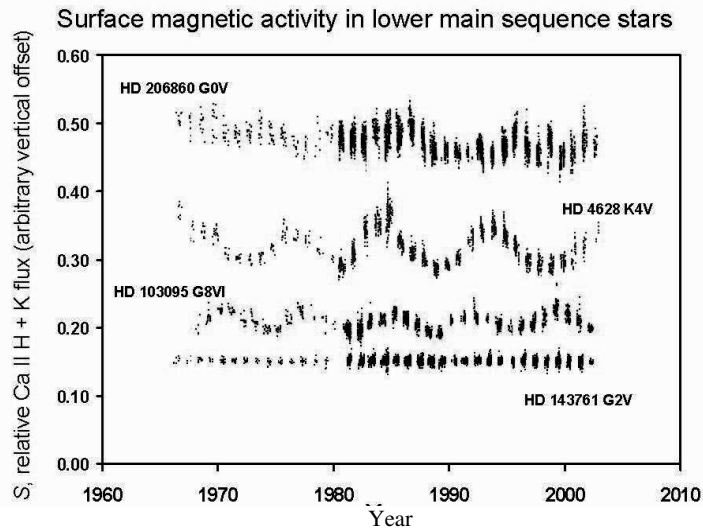


Fig. 2.12. Examples of chromospheric activity cycles (as observed in the H and K resonance lines of singly ionized Ca, or Ca II H+K). Surface magnetic activity records of four stars on or near the lower main sequence from a survey begun by O. C. Wilson in 1966 at Mount Wilson Observatory. Surface magnetism is measured as the ratio of the flux in the emission cores of singly-ionized calcium lines in the violet (the Fraunhofer H and K lines at 393.3 and 396.8 nm) and photospheric flux in nearby regions of the spectrum, necessarily integrated over the unresolved stellar disks. The strength of the H and K fluxes increases as the coverage by and intensity of magnetic surface features increases; on the sun the H and K fluxes vary nearly in phase with the sunspot cycle. The four records show the counterpart of the sun approximately 2 billion years ago (upper curve, HD 206860; $P = 4.7$ d), and then three Sun-like stars, which show records similar to the present-day sun, HD 4628 ($P = 38$ d), HD 103095 ($P = 31$ d, or $P = 60$ d [Frick et al., 2004]) and HD 143761 ($P = 21$ d). Both HD 4628 and HD 103095 display decadal periodicities similar to the sunspot cycle. The star HD 143761 may be in a state like the Sun's Maunder minimum. The star HD 103095 is an extremely old (approximately 10 billion years) metal deficient subdwarf, and is shown as an example of the persistence of decadal magnetic activity cycles in a star of extreme age compared to the Sun. The spectral types are listed next to each record's star name. Arbitrary vertical shifts in the average value of the H and K relative fluxes have been applied in order to show the records without overlap; the offsets are 0.0 (HD 143761), 0.02 (HD 103095), 0.09 (HD 4628) and 0.15 (HD 206860). Courtesy S. L. Baliunas.

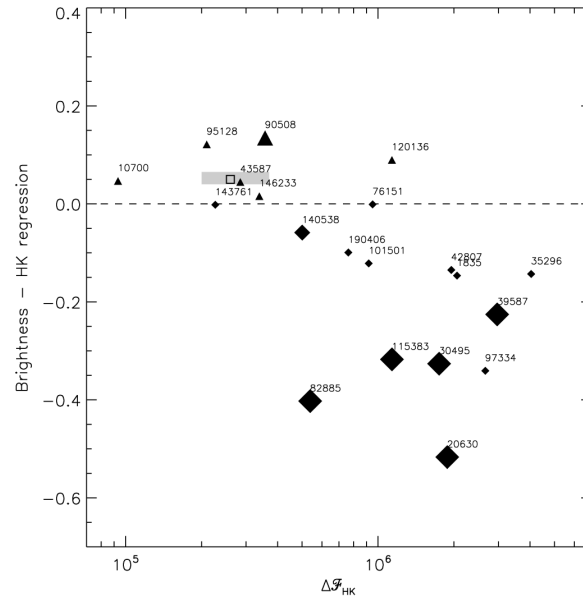


Fig. 2.13. Slope of the regression of photometric brightness variation versus chromospheric (Ca II H&K) emission variation, plotted as a function of average chromospheric activity level as measured by the Ca II H+K excess flux density: stars above the dashed line increase in brightness with activity (the Sun's range in activity is indicated by the shaded box; note that the vertical position of the Sun in this diagram is based on bolometric variations, whereas for the other stars it is based on the b and y Strömgren passbands), while stars below the dashed line decrease in brightness with increasing activity. The stars HD 10700 (τ Ceti, G8 V) and HD 143761 (ρ CrB, G2 V) are considered solar analogs in a state possibly like that of the Sun's Maunder minimum. Figure from Hall et al. (2009); see also Radick et al. (1998).

Sun-like stars of different ages

Name	Spectral type	P_{rot} (days)	Age (Gyr)
EK Dra	G1.5 V	2.7	0.1*
π^1 UMa	G1.5 V	4.9	0.3
χ^1 Ori	G1 V	5.2	0.3
κ^1 Cet	G5 V	9.2	0.7
β Com	G0 V	12.	1.6
Sun	G2 V	25.4	4.6
β Hyi	G2 IV	~ 28	6.7

* Järvinen et al. (2007) report an age of 0.03 – 0.05 Gy.

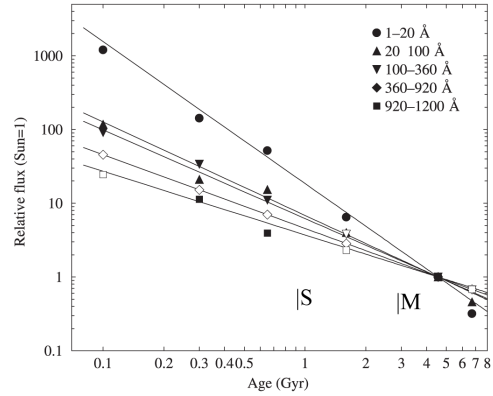


Fig. 2.14. Spectral radiance versus age of solar-type stars (identified in the table on the left, with spectral type, rotation period, and estimated age), in solar units. Measurements are shown by filled symbols; missing data (open symbols) are derived from power law fits (solid lines) for passbands from 1 to 1200Å. The approximate ages for which the oldest fossils of single-cell microbial life (S) and multi-cellular plants and animals (M) have been found on Earth are indicated (cf., Ch. 4). Figure adapted after Ribas et al. (2005).

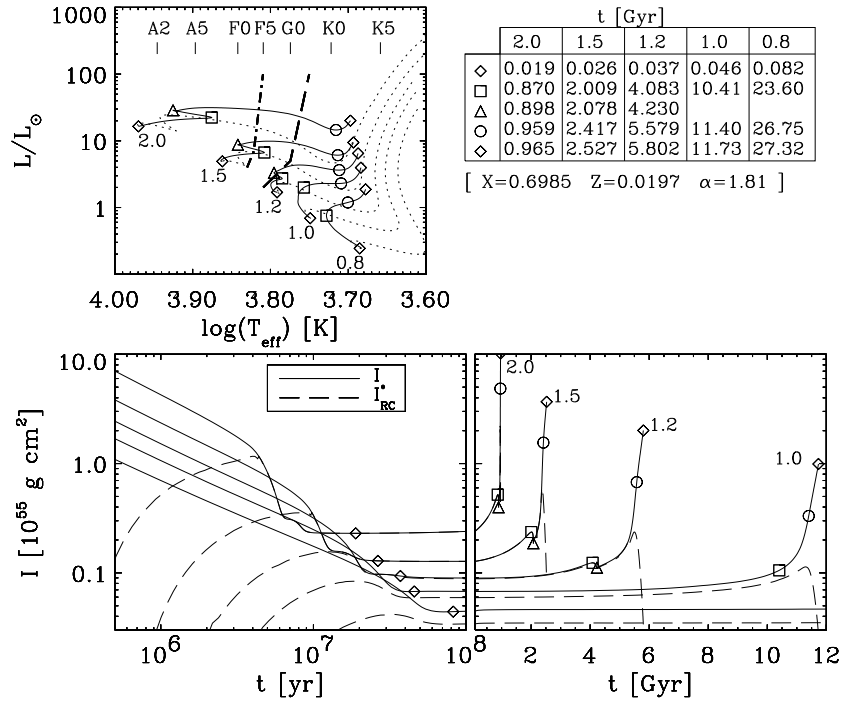


Fig. 2.15. Evolutionary tracks (top panel) for late-type stars of various masses, from the pre-main sequence to main sequence (dotted curves in the top panel), and from there to the base of the giant branch (solid curves in the top panel). The diamonds indicate the zero-age main sequence (at the lower-left end of the solid curves) and the end of model computations. Stellar masses are given in units of the solar mass. The dashed-dotted curve marks the onset of envelope convection. Ages at selected points along the tracks are listed in the table in the top right of this figure for stellar masses indicated in the top row. The evolutionary variations of moments of inertia of the entire star (solid curves) and of the radiative interior (dashed curves) are shown in the lower panels (figure from Charbonneau et al., 1997).

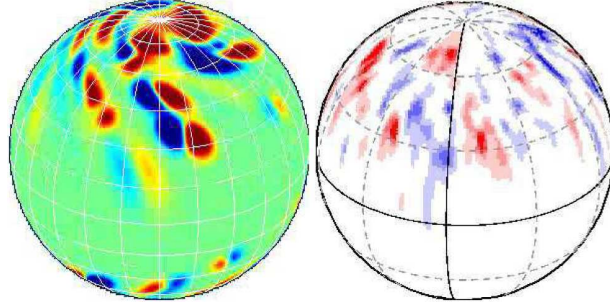


Fig. 2.16. *Left*: Radial magnetic field simulated with a surface flux transport models assuming solar-like transport parameters, but for a flux emergence rate that is $30\times$ solar, and a larger latitudinal range for flux emergence, combined with a meridional flow peaking at 100 m/s ($\sim 5\times$ solar). *Right*: Observed radial magnetic field distribution for the rapidly rotating star AB Doradus ($P_{\text{rot}} = 0.51\text{ d}$). From Holzwarth et al. (2007). In both panels, red and blue tones indicate oppositely-directed radial magnetic field strengths.

3

Formation and early evolution of stars and proto-planetary disks

Lee W. Hartmann

22 Formation and early evolution of stars and proto-planetary disks

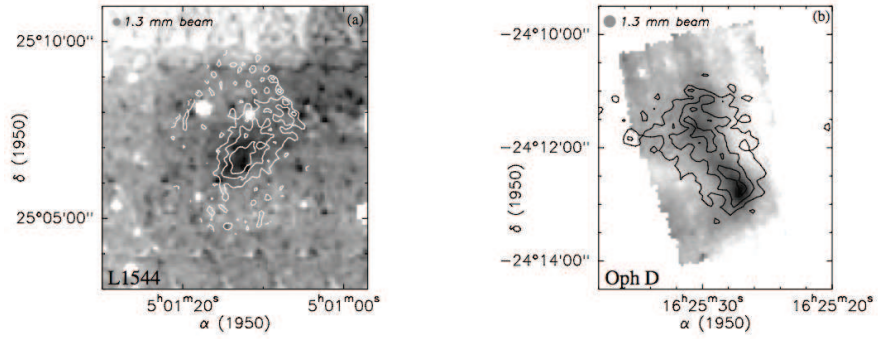


Fig. 3.1. Starless molecular cloud cores (protostellar clouds), as detected in mid-infrared extinction (grayscale) and 1.3 mm dust continuum emission (contours). From Bacmann et al. (2000).

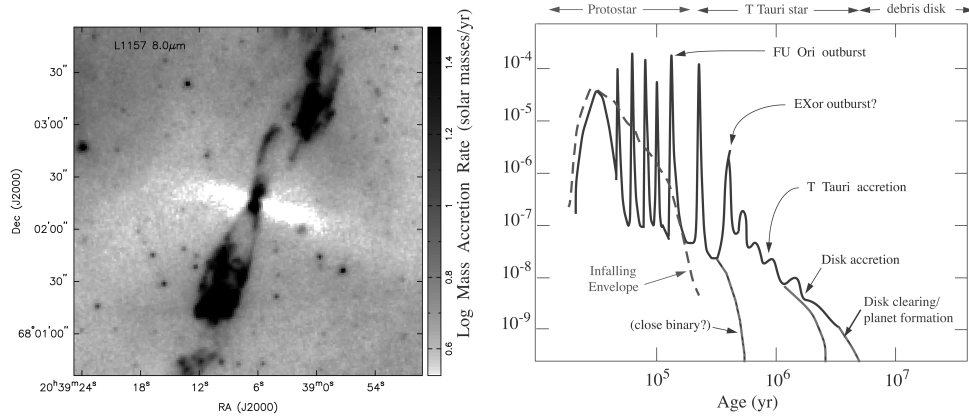


Fig. 3.2. *Left:* An $8\mu\text{m}$ image of an accreting low-mass protostar. The lighter, filamentary region running east-west (horizontally in the image) represents dust extinguishing the background radiation; this indicates that the densest, most massive region of the material falling in to make disk and star is far from spherically-symmetric. The dark regions running north-south (top to bottom) are due to protostellar continuum emission reflected from dust and molecular emission lines excited by a high-velocity, bipolar outflow thought to be driven from the innermost regions of the protostellar accretion disk. Courtesy John Tobin. *Right:* Schematic diagram of a likely accretional history of a typical low-mass star. The dashed curve indicates the expected rate of infall of matter from the protostellar envelope (e.g., dense region indicated in the left-hand panel). The solid curve suggests a possible variation of accretion through the protostellar disk onto the central star, which may be steady at the earliest times but is subject to strong variations in accretion (so-called FU Ori outbursts). In this picture, material piles up in the disk due to the infall rate being higher than the disk can smoothly pass on to the central star; this leads to episodic bursts of accretion which drain the excess disk mass. Finally, after infall ceases, slower, more steady accretion occurs during the T Tauri phase, which may cease because either a binary companion or planets accrete the remaining mass. This results in “clearing” the disk, i.e. removing most of the small dust and apparently most of the gas. Finally, secondary production of small amounts of dust can occur during the debris disk stage, when solid bodies collide and shatter. From Hartmann (2009).

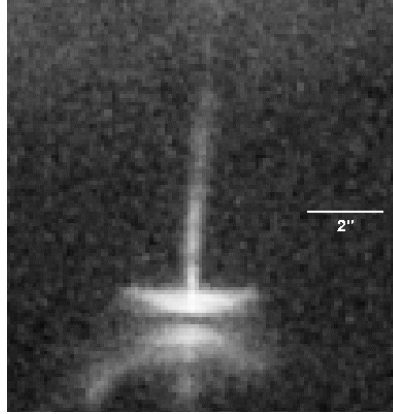


Fig. 3.3. Optical image of the accreting young star HH 30, showing the upper surfaces of its dusty disk in scattered light (the dark lane is due to dust extinction of the central star by the disk), along with an optical, high-velocity, bipolar jet. For scale, 2 arcsec = 280 Astronomical Units. From Burrows et al. (1996).

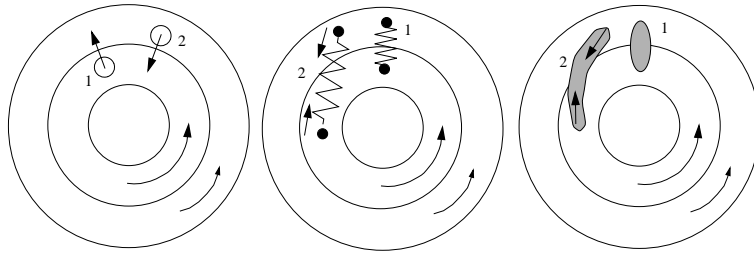


Fig. 3.4. Schematic treatment of angular momentum transfer in a shearing disk with angular velocity decreasing outwards. An initially radial field is perturbed radially (left panel); these radial perturbations grow due to the shear in the disk (middle panel). In the case of gravitational instability (right panel), an excess of material gets sheared out by the differential rotation; the gravitational attraction on the sheared excess (spiral arm pattern) exerts a restoring force in the same sense as the magnetic case, again transferring angular momentum outward. From Hartmann (2009).

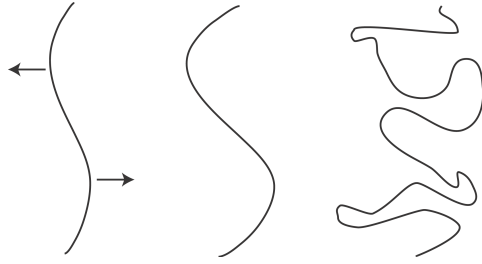


Fig. 3.5. Schematic development of an initially vertical magnetic field in the disk perturbed radially, as viewed in a meridional plane. The indicated perturbations result in the magnetic field becoming stretched radially as indicated in the middle part of the figure, as the field also becomes sheared by the disk angular velocity gradient (see the middle panel of Figure 3.4). Eventually the stretching and shearing of the field results in diffusion and reconnection, resulting in turbulence as indicated in the right-most part of the figure.

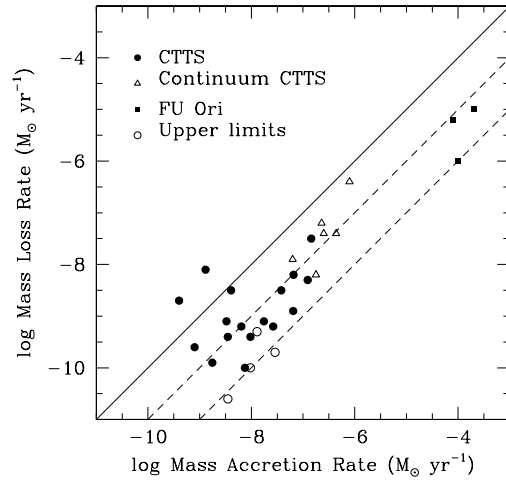


Fig. 3.6. Mass accretion rates in young stars vs. mass loss rates. Errors are probably factors of three or more in each coordinate. The solid line is $\dot{M}(\text{wind}) = \dot{M}(\text{accretion})$; the dashed lines are wind mass loss rates of 10% and 1% of the mass accretion rate. Overall, the observations indicate that mass ejection is about 10% of the mass accretion rates, consistent with energetic requirements of driving the mass loss by accretion energy (see text). Taken from Calvet (1998).

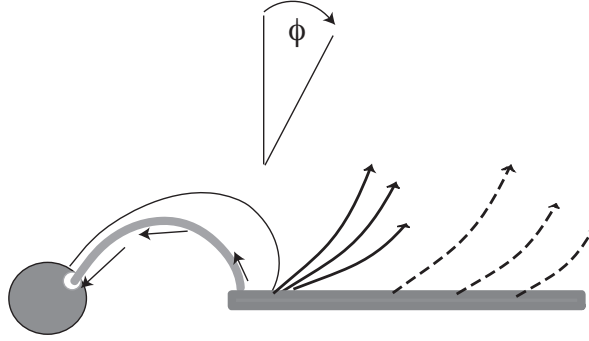


Fig. 3.7. Schematic structure for a connected system of accretion disk, stellar wind, and stellar magnetosphere. Magnetic fields which penetrate the disk inside the corotation radius (where the angular velocity of the rotating disk matches the angular velocity of the star) allow material to accrete (gray curves); fields penetrating the disk outside of corotation help provide a spindown torque (solid dark curve). In the X-wind model (Shu et al., 1994), the wind arises from the disk just at corotation (arrows), while disk wind models involve mass loss from a wider range of disk radii (dashed arrows). Magnetic field lines pitched at angles $\Phi_e > 30^\circ$ allow for rapid, cold mass loss (see text).

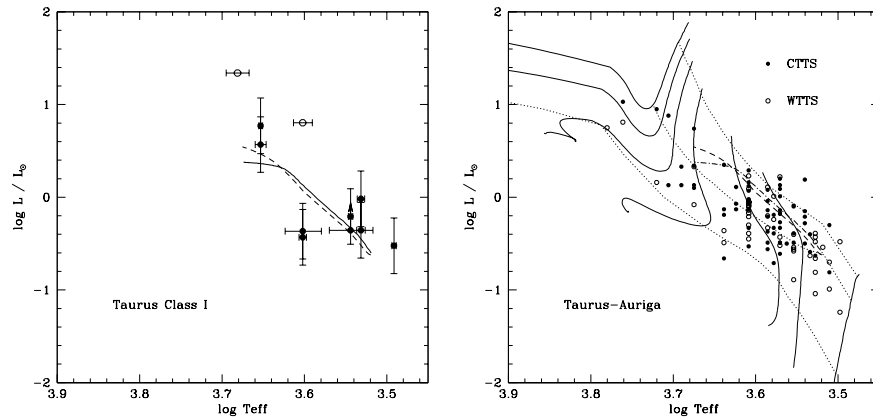


Fig. 3.8. Hertzsprung-Russell diagram positions of Taurus protostars (left) and young (T Tauri) stars (right). These plots of two observed quantities - the stellar luminosity L (in solar units) and the effective temperature T_{eff} - can be used directly to infer the stellar radius R via the equation $L = 4\pi R^2 \sigma T_{eff}^4$, and indirectly the stellar mass via evolutionary tracks. *Left*: Solid and dashed curves correspond to theoretical estimates of initial protostellar radii (“birthlines”) as a function of effective temperature (which corresponds roughly to mass). The open circles denote objects in which most of the luminosity derives from accretion, not stellar photospheric radiation. The agreement between theory and observation is reasonably satisfactory given the uncertainties, showing that low-mass protostars do indeed begin their existence with radii only a few times larger than that of the Sun’s (see text). *Right*: Standard stellar evolutionary tracks compared with observed HR diagram positions of T Tauri stars in the Taurus–Auriga star-forming region. The dashed lines show approximate isochrones for 1×10^6 y, and 1×10^7 y, assuming contraction from very large radii, along with the birthlines of the left-hand panel. Ages of young solar-type stars are thus determined by the amount they have descended in the HR diagram from the birthline, due to gravitational contraction (see text). From Hartmann (2009).



Fig. 3.9. Inferred magnetic field structure of the classical T Tauri star BP Tau. Surface shading shows photospheric magnetic field strength; the three figures from left to right show estimated near-field closed, far-field closed, and open magnetic field lines. Red and blue tones indicate oppositely-directed radial magnetic field strengths. From Gregory et al. (2008).

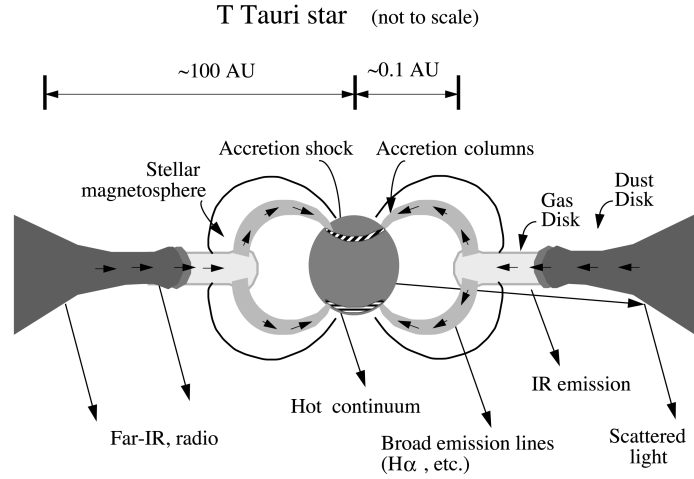


Fig. 3.10. Schematic representation of magnetospheric/disk interaction in low-mass, pre-main sequence (T Tauri) stars, with diagnostics of specific regions labeled. From Hartmann (2009).

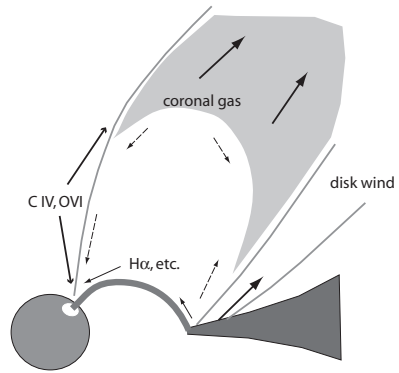


Fig. 3.11. Twister model of magnetic coupling and ejection in a star-disk system. From Hartmann (2008).

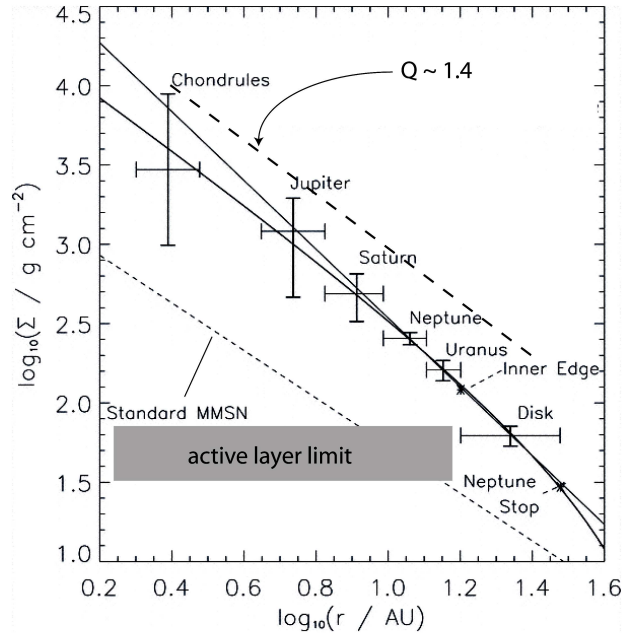


Fig. 3.12. Two estimates of the minimum mass solar nebula. The lower, light-dashed curve indicates the usual estimate, derived from the current position of the giant planets and accounting for the missing light elements; the solid curves show a higher estimate based on the initial positions of the giant planets assumed in a model which has substantial outward migration of the giant planets. Limits on the expected MRI-active surface density due to non-thermal ionization and on the surface density expected for a marginally gravitationally-unstable disk (the dashed line showing the condition for the critical value of the “Toomre Q ” parameter; see Eq. (3.9) are also shown. Modified from Desch (2007).

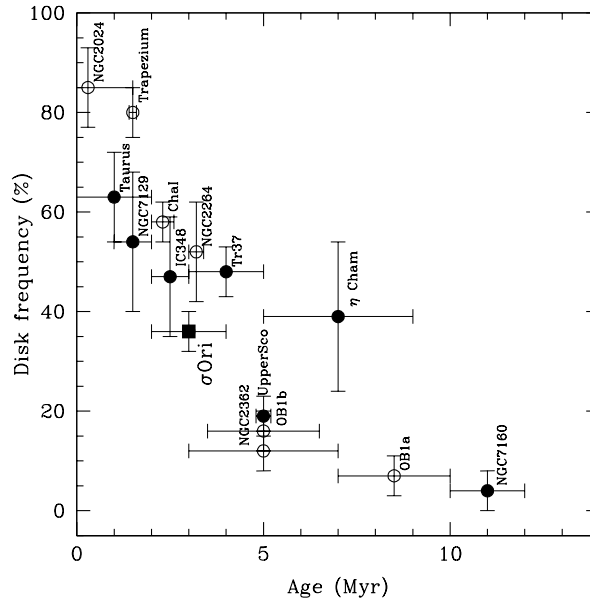


Fig. 3.13. Fraction of stars with near-infrared disk emission as a function of the age of the stellar group. Open circles represent the disk frequency for stars in the T Tauri mass range, derived using observations out to $2\text{--}3\ \mu\text{m}$; solid symbols represent the disk frequency as measured to $8\ \mu\text{m}$ or beyond. Modified from Hernández et al. (2007); also Hartmann (2009).

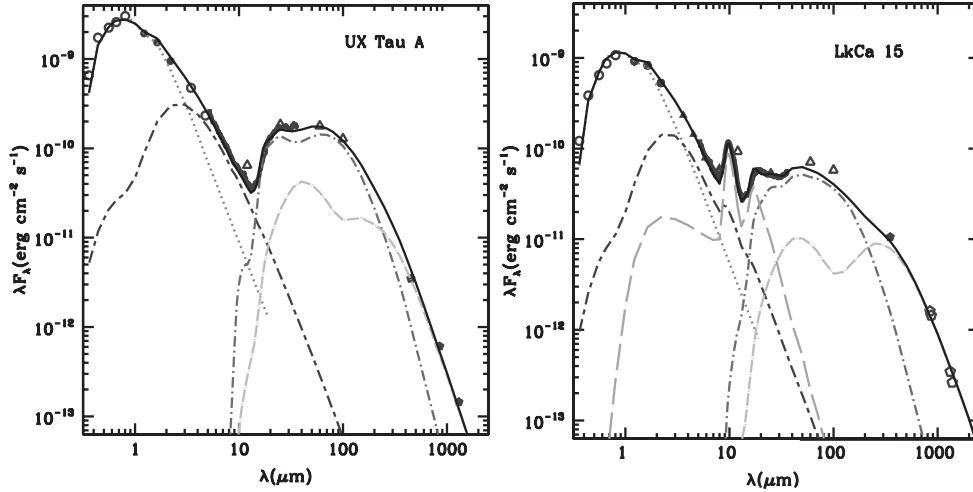


Fig. 3.14. Spectral energy distributions of two T Tauri stars which appear to have mostly optically-thick dust disk emission, but with inner gaps, as indicated by the dip(s) in emission at wavelengths of $\sim 10\mu\text{m}$. The estimated size for UX Tau A of the gap is ~ 50 AU; LkCa 15 has a small amount of optically thin dust within a gap of outer radius of about 46 AU, consistent with mm-wave interferometry. The solid curves are total model fluxes to compare with observations; moving sequentially to longer wavelengths, the dotted curves show the stellar photosphere, long dot-long dash curves inner disk dust emission, dot-dash curves emission from the disk “wall” facing the star, and light dot-dash curves outer disk emission. Modified from Espaillat et al. (2007).

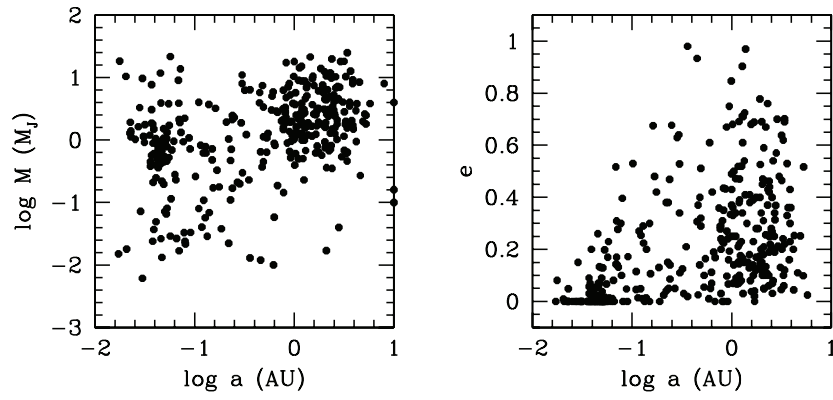


Fig. 3.15. Mass (left; in Jupiter masses) and orbital eccentricity (right) for known exoplanets vs. semi-major axis. From <http://exoplanet.eu>.

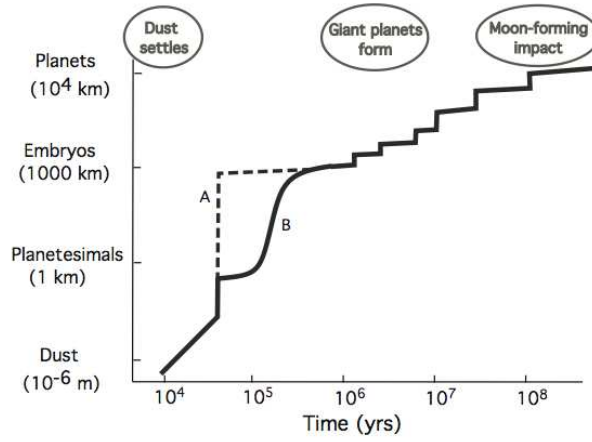


Fig. 3.16. Schematic scale-age diagram for major stages of planet formation. From Lunine *et al.* (2009).

4

Planetary habitability on astronomical time scales

Donald E. Brownlee

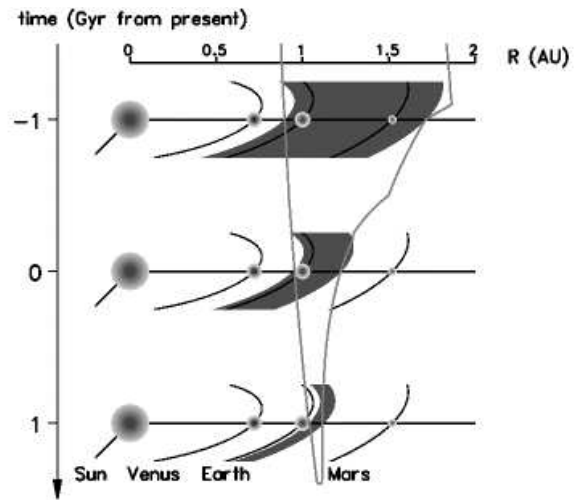


Fig. 4.1. The photosynthetic habitable zone (pHZ) over time, from 1 Gyr in the past to 1 Gyr in the future. The inner edge of the pHZ moves outwards as the Sun becomes brighter with age and the outer edge moves inwards as surface warming leads to decline of CO₂ in the atmosphere to the point where photosynthesis is not possible. Figure from von Bloh et al. (2002).

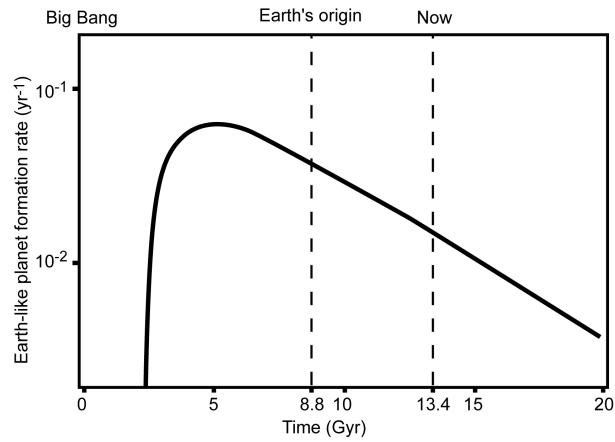
Planetary habitability on astronomical time scales

Fig. 4.2. The estimated formation rate of Earth-like planets in the Galaxy over time. The optimum time to form habitable planets like Earth peaked in the first half of the current age of the Universe. Figure adapted from Lineweaver (2001).

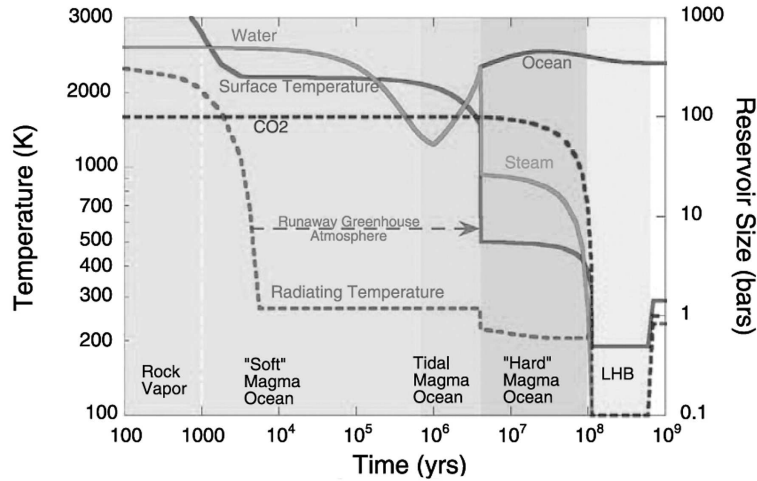


Fig. 4.3. The Earth's surface temperature and above-surface reservoirs of water and carbon dioxide after the Moon-forming collision. The water dip after $\sim 10^6$ y occurs because of storage of water in Earth's short-lived magma ocean. The surface temperature drops below 1000 K after a few million years when Earth's steam atmosphere condenses, and it drops below 500 K to habitable conditions after about 100 million years when most of the atmospheric CO₂ is incorporated into the mantle. Figure from Zahnle et al. (2007).

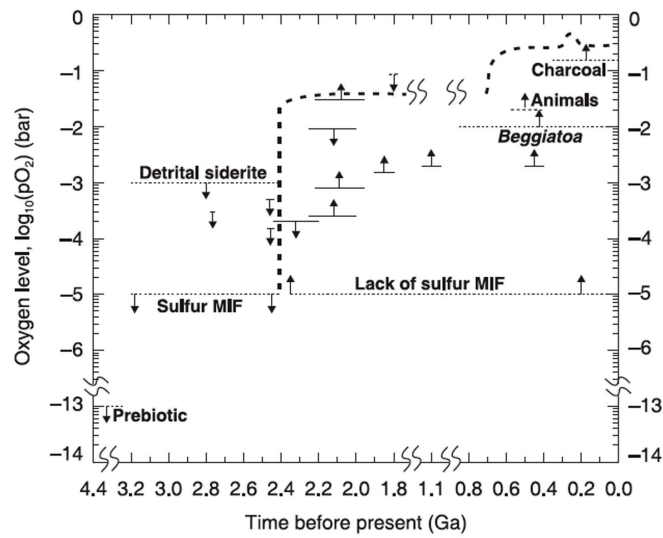


Fig. 4.4. Estimates of the evolution of Earth-atmospheric oxygen implied by various biological and mineralogical indicators. The presence of mass-independent fraction (MIF) of sulfur isotopes before 2.4 Gy ago is the best determinant of the time marking the rise of oxygen and the decline of atmospheric methane. Figure from Clair et al. (2006).

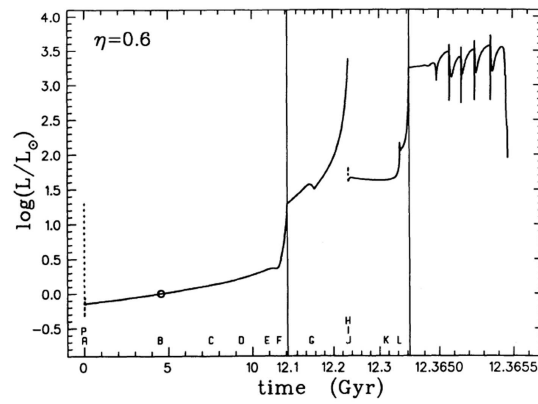


Fig. 4.5. Evolution of the luminosity of the Sun over its full life span. The first 12 billion years show the gradual brightness as hydrogen is depleted in the core of the the Sun's main-sequence life time as a hydrogen-burning star (cf., Fig 2.9). The large luminosity increases and pulses that follow this period include both the red-giant and asymptotic giant branch (AGB) phases when the Sun swells in size and loses appreciable mass to space. Figure from Sackmann and Boothroyd (1993).

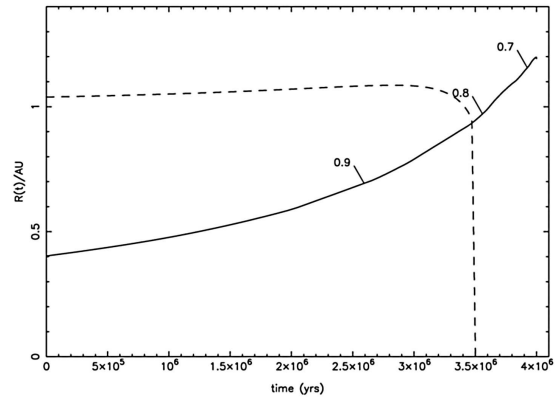


Fig. 4.6. The diameter of the red-giant Sun (solid; in AU) and the size of Earth's orbit (dashed) during the 4 million years leading up to the phase when the Sun reaches maximum brightness. Earth's orbit expands slightly as the Sun loses mass but the Sun expands to the point where tidal drag causes Earth's orbit to decay and intersect the Sun's upper layers. These calculations by Schroder and Smith (2008) predict that Earth will be destroyed in the Sun's atmosphere 7.59 billion years from present.

5

Solar internal flows and dynamo action

Mark S. Miesch

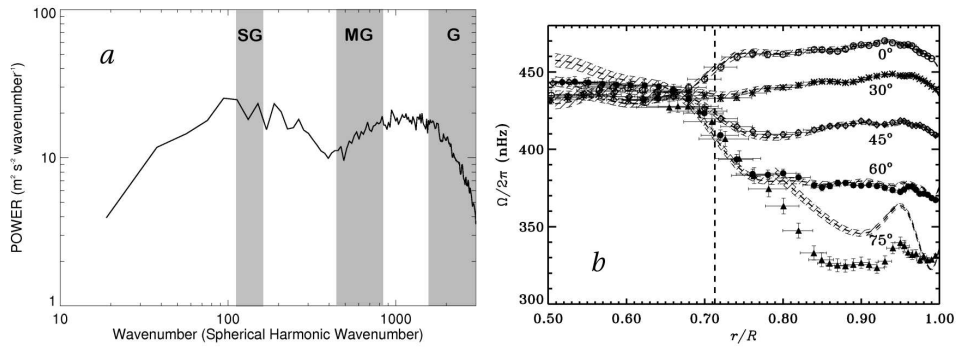


Fig. 5.1. Panel *a*: Power spectrum of the convective velocity field in the solar photosphere obtained from Doppler measurements, plotted as a function of spherical harmonic degree ℓ (from ?, ?). Mean flows and p -modes are filtered out. The falloff beyond $\ell \sim 1500$ reflects the resolution limit of the Michelson Doppler Imager (MDI) instrument onboard the SOHO spacecraft from which these data were obtained and is therefore artificial. Shaded areas indicate the approximate size ranges of supergranulation (SG), mesogranulation (MG) and granulation (G). Note that the expected granulation spectral peak at $\ell \sim 4400$, corresponding to $L \sim 1$ Mm, is not resolved. Panel *b*: The solar internal rotation profile inferred from helioseismic inversions (from ?, ?). Angular velocity $\Omega/2\pi$ is shown as a function of fractional radius r/R_\odot for several latitudes as indicated. Symbols and dashed lines denote different inversion methods, known as subtractive optimally localized averages (SOLA) and regularized least squares (RLS) respectively. Vertical $1\text{-}\sigma$ error bars (SOLA) and bands (RLS) are indicated and horizontal bars reflect the resolution of the inversion kernels. The vertical dashed line indicates the base of the convection zone.

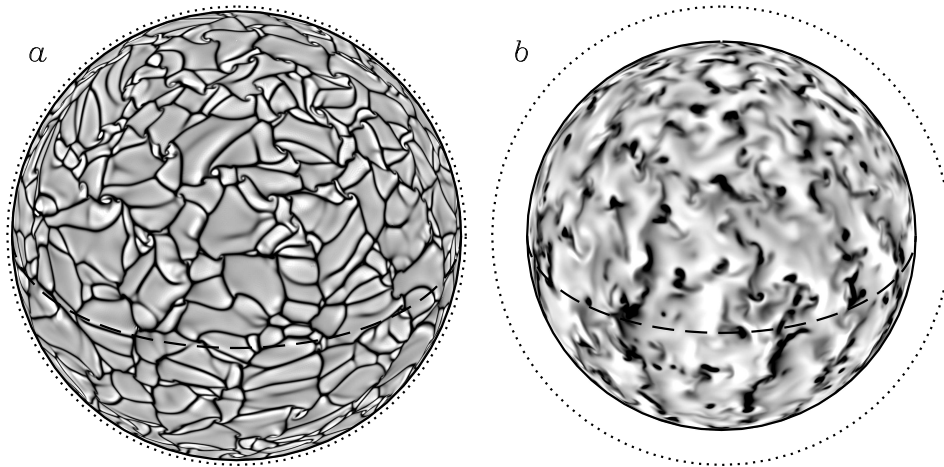


Fig. 5.2. Radial velocity patterns in a global simulation of solar convection are shown on two horizontal surfaces: Panel *a* lies within the thermal boundary layer near the outer boundary of the computational domain ($r = 0.98R_{\odot}$) and panel *b* lies in the middle of the convection zone ($r = 0.85R_{\odot}$). Both images are orthographic projections with the north pole tilted 30° toward the line of sight. The equator is indicated by a dashed line and the solar surface (outside the computational domain) is indicated by a dotted line. Bright tones denote upflow and dark tones downflow. The range of the gray scales is (*a*) $-30 - +20 \text{ m s}^{-2}$ and (*b*) $-200 - +100 \text{ m s}^{-1}$. From ? (?).

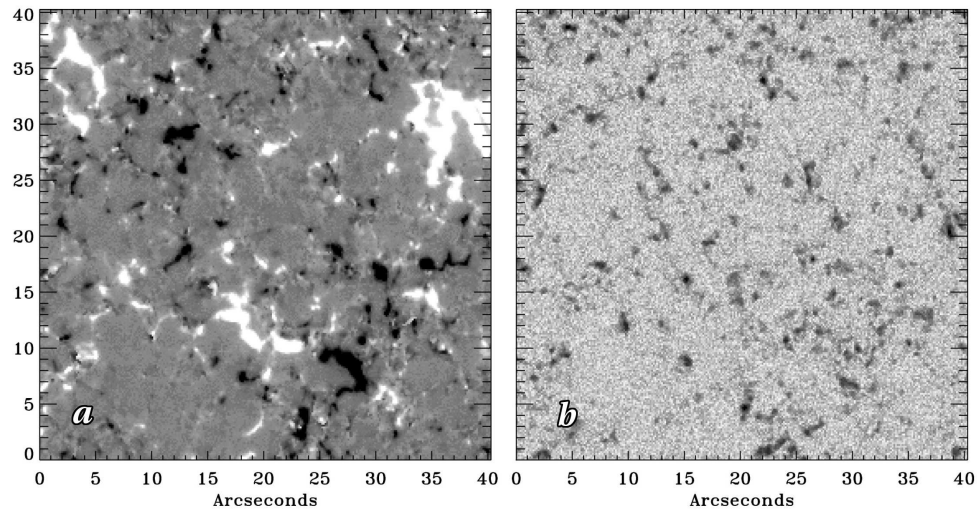


Fig. 5.3. The apparent flux density for the (a) vertical and (b) horizontal magnetic field components in the quiet Sun at disk center obtained from the solar optical telescope spectro-polarimeter (SOT/SP) onboard the Hinode spacecraft (from ?, ?). In panel *a* black and white denote inward and outward flux respectively and the grey scale saturates at $\pm 50 \text{ Mx cm}^{-2}$, with an average amplitude of 11 Mx cm^{-2} . In panel *b* dark tones denote high values, with a saturation level of 200 Mx cm^{-2} and an average value of 55 Mx cm^{-2} . For reference, the typical size of a granule is about $1.4''$ which corresponds to 1 Mm. Note that the values for the apparent flux density are related to the intrinsic field strength in Gauss but the precise relationship is subject to uncertainty associated with the nature and sensitivity of the measurement, the calibration, and the spatial, temporal, and spectral averaging (from Lites, 2008).

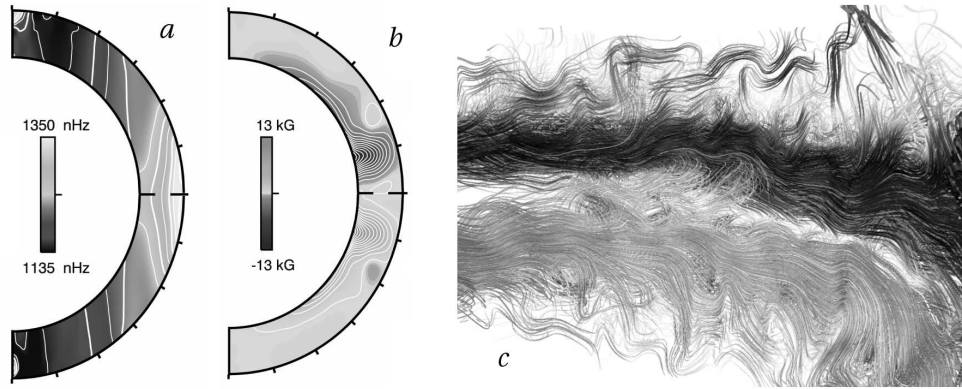


Fig. 5.4. Rotational shear and toroidal fields in a global 3D dynamo simulation of a solar-type star rotating at three times the solar rate (from ?, ?). (*a*) Angular velocity Ω and (*b*) toroidal field $\langle B_\phi \rangle$, averaged over longitude and time. Panel *c*): A 3D rendering of magnetic field lines in a portion of the convection zone, spanning about 50° in longitude. Grey (red) and black (blue) lines denote positive and negative B_ϕ respectively. The view is radially outward from a vantage point under the convection zone and slightly above (north of) the equator. See also the color plate section

Solar internal flows and dynamo action

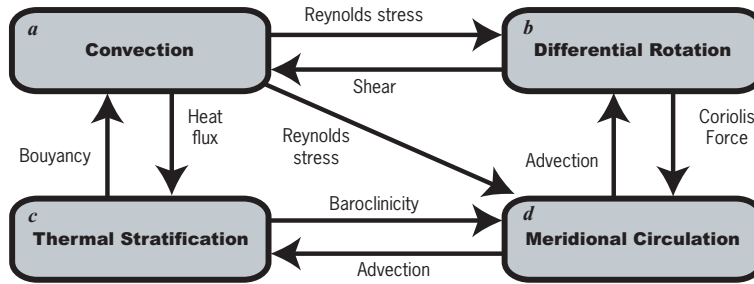


Fig. 5.5. Diagram illustrating the maintenance of mean flows in stellar convection zones (from ?, ?).

6

Modeling solar and stellar dynamos

Paul Charbonneau

Modeling solar and stellar dynamos

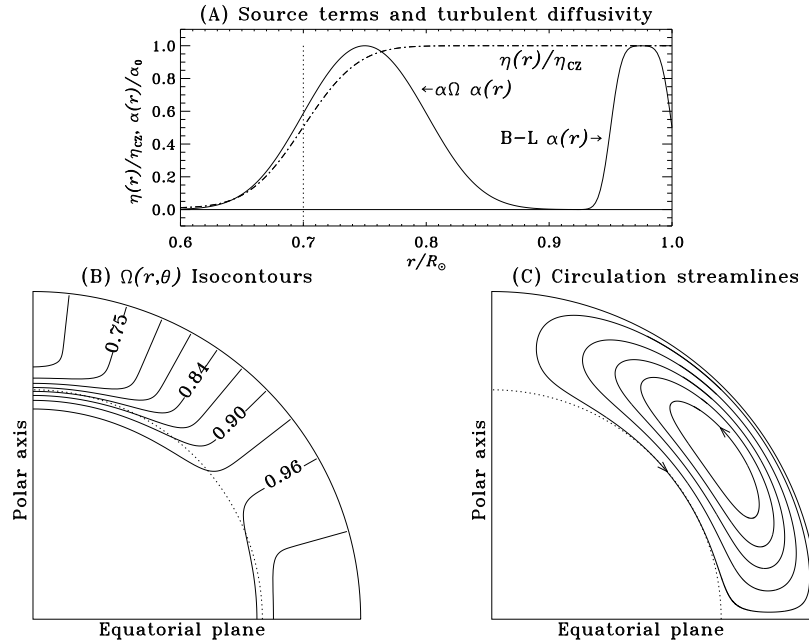


Fig. 6.1. Various “ingredients” for the dynamo models constructed in this chapter. Part A shows radial profiles of the total magnetic diffusivity and poloidal source terms. Part B shows contour levels of the rotation rate $\Omega(r, \theta)$ normalized to its surface equatorial value. The dotted line is the core-envelope interface at $r/R = 0.7$. Part C shows streamlines of meridional circulation, included in some of the dynamo models discussed below.

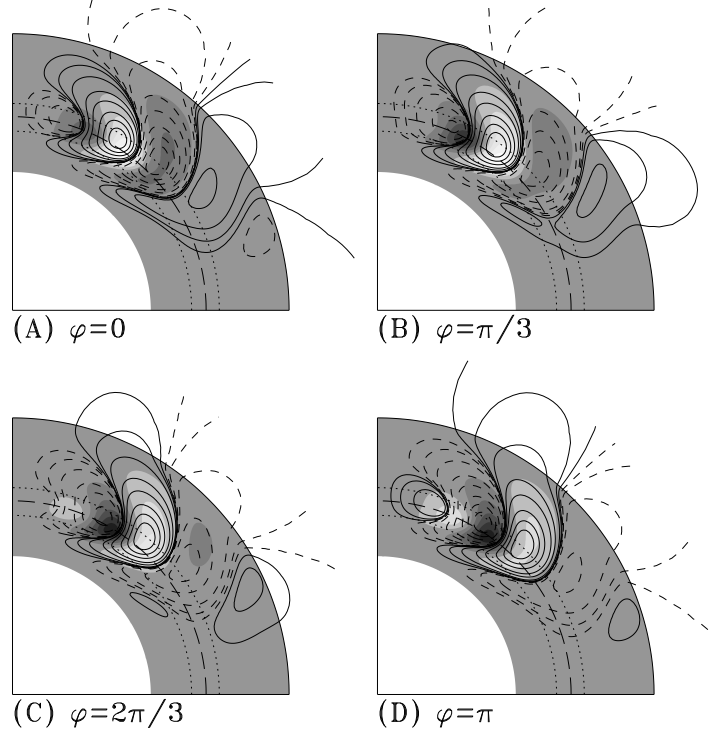
BaseCZ $\alpha \sim \cos\theta$ $C_\alpha = +5$ $C_\Omega = 25000$ $Rm = 0$


Fig. 6.2. Four snapshots in meridional planes of our minimal linear $\alpha\Omega$ dynamo solution with defining parameters $C_\Omega = 25000$ (see Eq. 6.11), $\Delta\eta = 0.1$ (see Eq. 6.12), $\eta_e = 5 \times 10^7 \text{ m}^2 \text{ s}^{-1}$. With $C_\alpha = +5$, this is a mildly supercritical solution, with oscillation frequency $\omega \simeq 300 \tau^{-1}$. The toroidal field is plotted as filled contours (gray to black for negative B , gray to white for positive B , normalized to the peak strength and with increments $\Delta B = 0.2$), on which poloidal field lines are superimposed (solid for clockwise-oriented field lines, dashed for counter-clockwise orientation). The long-dashed line is the core-envelope interface at $r_c/R = 0.7$.

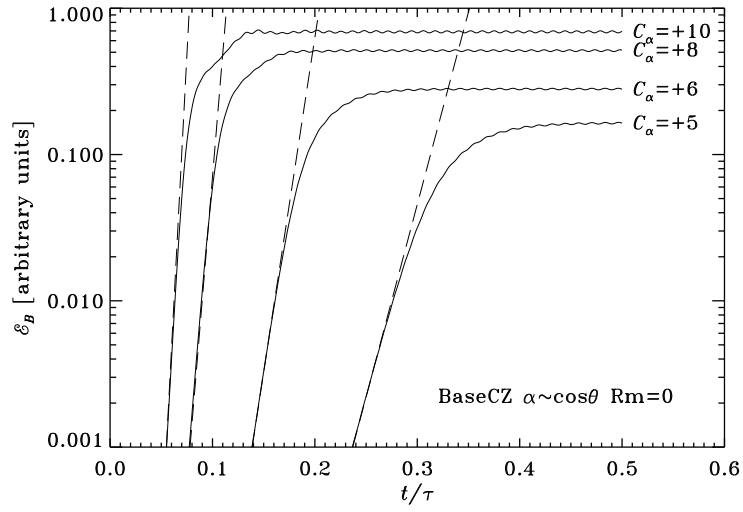


Fig. 6.3. Time series of magnetic energy for a set of $\alpha\Omega$ dynamo solutions using our minimal $\alpha\Omega$ model including algebraic α -quenching, and different values for dynamo number C_α (Eq. 6.11), as labeled. Magnetic energy is expressed in arbitrary units; time is expressed in units of the diffusion time scale (Eq. 6.8). The dashed line indicates the exponential growth phase characterizing the linear regime.

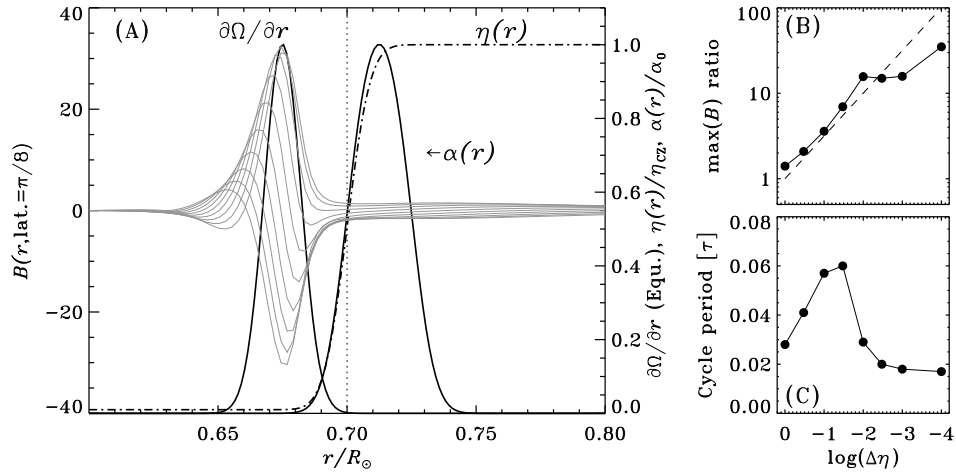


Fig. 6.4. A representative interface dynamo model in spherical geometry. This solution has dynamo numbers $C_\Omega = 2.5 \times 10^5$ and $C_\alpha = +10$ (see Eq. 6.11), and a core-to-envelope diffusivity contrast of 10^{-2} . Panel (A) shows a series of radial cuts of the toroidal field at latitude 15° (grey lines). The (normalized) radial profiles of magnetic diffusivity, α -effect, and radial shear are also shown, again at latitude 15° . The core-envelope interface is at $r/R = 0.7$ (dotted line), where the magnetic diffusivity varies near-discontinuously. Panels (B) and (C) show the variations of the core-to-envelope peak toroidal field strength and dynamo period with the diffusivity contrast, for a sequence of otherwise identical dynamo solutions.

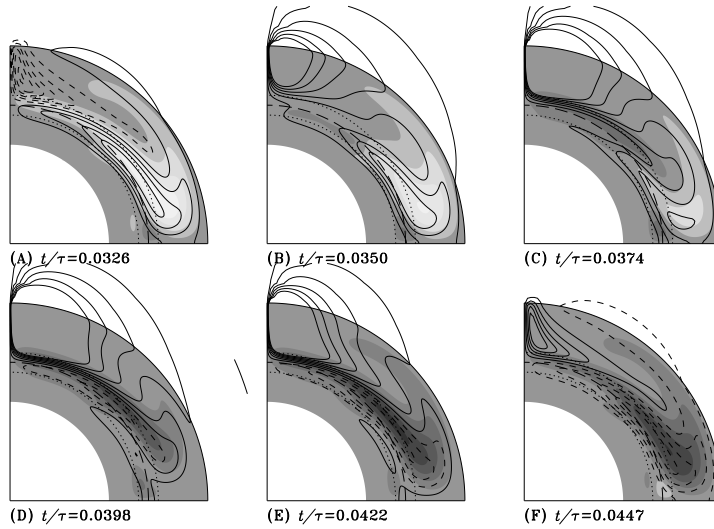


Fig. 6.5. Snapshots covering half a cycle of an $\alpha\Omega$ dynamo solution including meridional circulation, starting at the time of polarity reversal in the polar surface field (time in units of the diffusion time scale in Eq. 6.8). The grey-scale coding of the toroidal field and poloidal field lines is as in Fig. 6.2. This α -quenched solution uses the same differential rotation, diffusivity, and α -effect profiles as in Fig. 6.2, with parameter values $C_\alpha = 0.5$, $C_\Omega = 5 \times 10^5$, $\Delta\eta = 0.1$, $R_m = 2500$. Note the strong amplification of the surface polar fields, the latitudinal stretching of poloidal field lines by the meridional flow at the core-envelope interface.

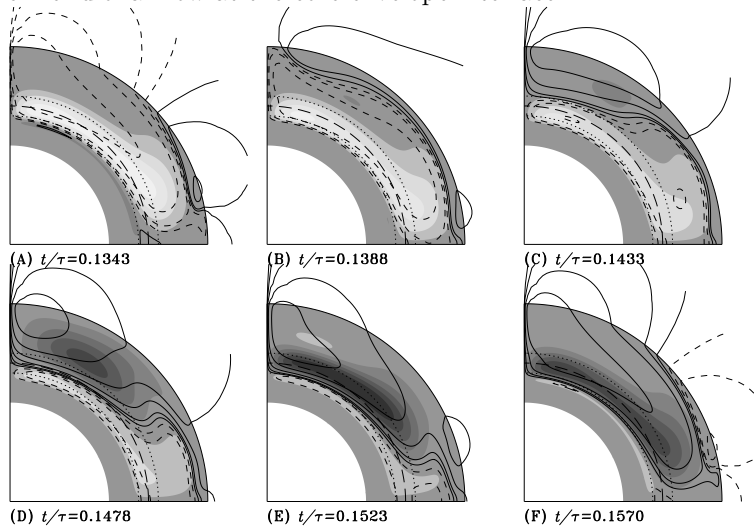


Fig. 6.6. As Fig. 6.5 for a Babcock-Leighton dynamo solution. This solution uses the same differential rotation, magnetic diffusivity and meridional circulation profile as for the advection-dominated $\alpha\Omega$ solution of Sect. 6.2.1.4, but now with the non-local surface source term defined through Eq. (6.21), with parameter values $C_\alpha = 5$, $C_\Omega = 5 \times 10^4$, $\Delta\eta = 0.003$, $R_m = 840$. Note again the strong amplification of the surface polar fields, and the latitudinal stretching of poloidal field lines by the meridional flow at the core-envelope interface.

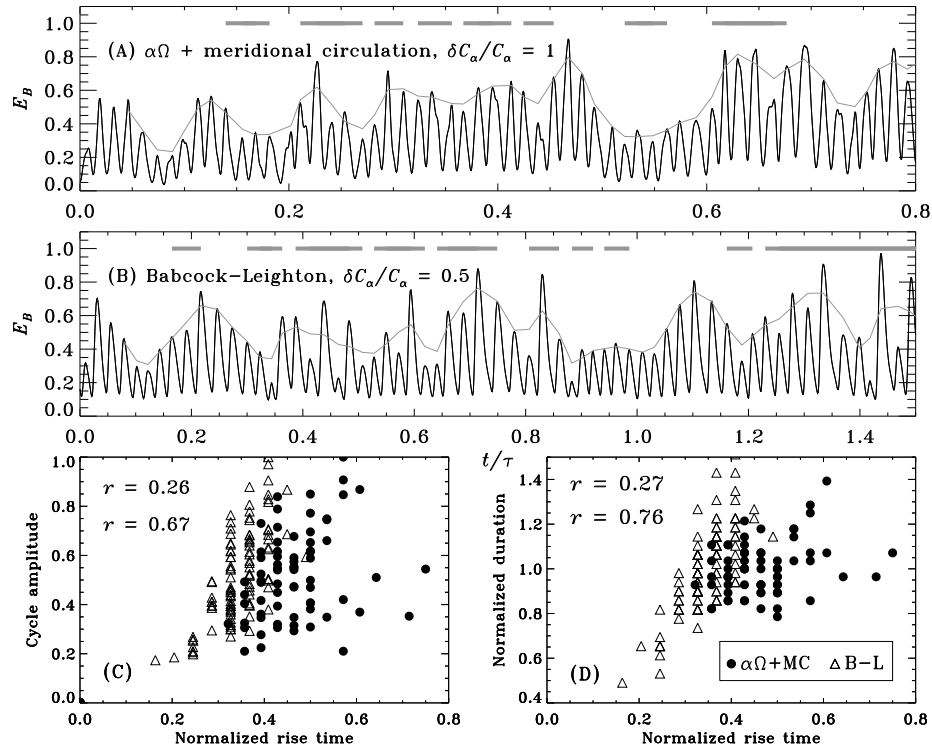


Fig. 6.7. Impact of stochastic fluctuations of the C_α dynamo number (Eq. 6.11) on the behavior of the advection-dominated mean-field $\alpha\Omega$ solution of Fig. 6.5, with 100% forcing of the poloidal dynamo number, and of the Babcock-Leighton solution of Fig. 6.6, with 50% fluctuation of the surface source term. In both cases the coherence time is $\sim 5\%$ of the cycle period. Panels A and B shows a time series for the magnetic energy (thick solid line), together with a 1-2-1 running mean of the peak amplitudes (grey line). The horizontal grey bars indicate epochs where a Gnevyshev-Ohl-like pattern holds. Panels (C) and (D) are Waldmeier-Rule-like correlation plots between cycle peak, rise time and duration with cycle peak and duration normalized to the corresponding values in the parent non-fluctuating solution.

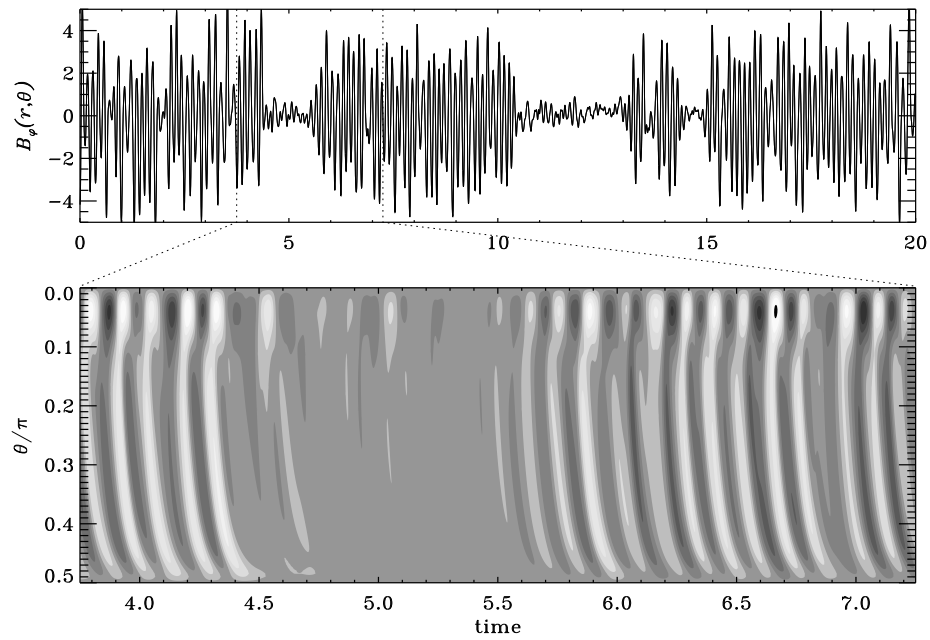


Fig. 6.8. Intermittency in a dynamo model based on the Babcock-Leighton mechanism (cf. Sect. 6.2.2). The top panel shows a trace of the toroidal field sampled at $(r, \theta) = (0.7, \pi/3)$. The bottom panel is a time-colatitude diagram for the toroidal field at the core-envelope interface (with positive and negative toroidal field strengths shown lighter or darker, respectively, relative to a grey zero point).

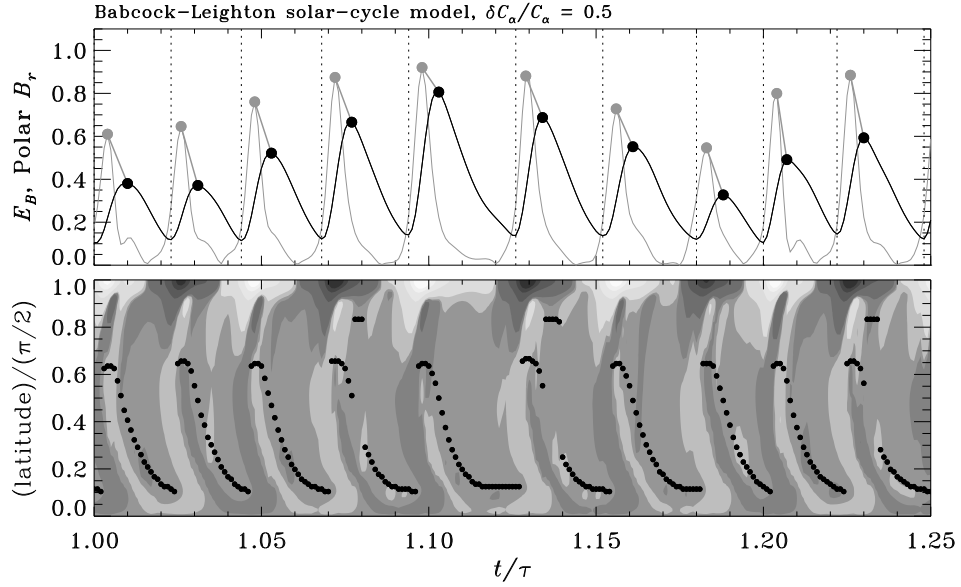


Fig. 6.9. Portion of a simulation run of a Babcock-Leighton model, with fluctuations at the $\pm 50\%$ level imposed in the magnitude of the surface source term. The unperturbed reference solution is that illustrated in Figure 6.6. The top panel shows time series of the surface radial magnetic field sampled at the pole (grey), together with a time series of the total magnetic energy (black), used here as a proxy for the sunspot number. The dark grey line segment joins the peak poloidal field at (or near) “sunspot minimum” with the peak in the sunspot number proxy for the following cycle. The bottom panel is a time-latitude diagram of the the surface radial field, and the black dots trace the latitude of peak toroidal field strength at the core-envelope interface at the corresponding time.

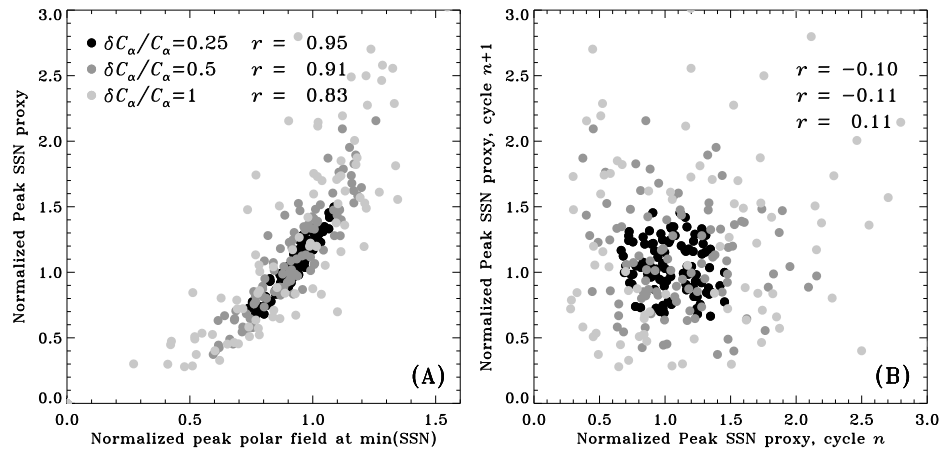


Fig. 6.10. (A) Correlations between peak sunspot number (SSN) and surface poloidal field strength in the stochastically-forced Babcock-Leighton solutions of Fig. 6.6, for three different level $\delta C_\alpha / C_\alpha$ of forced stochastic fluctuations in the surface source term, grey-coded as indicated and listing the corresponding linear correlation coefficient r . The red dots corresponds to the simulation run illustrated in Fig. 6.9. (B) Scatter diagram between the peak in sunspot number proxy for successive pairs of cycles. All amplitudes are normalized to those characterizing the non-fluctuating parent simulation.

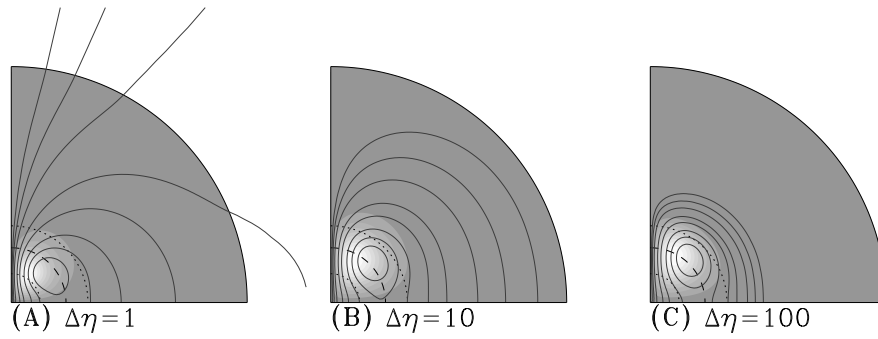


Fig. 6.11. Three antisymmetric steady α^2 dynamo solutions, computed using increasing magnetic diffusivity ratios between the core and envelope. The solutions are plotted in a meridional quadrant, with the symmetry axis coinciding with the left quadrant boundary. Poloidal field lines are plotted superimposed on a grey scale representation for the toroidal field (dark to light is weaker to stronger field). The dashed line marks the core-envelope interface depth r_c , and the two dotted lines indicates the depths $r_c \pm w$ corresponding to the width of the transition layer between core and envelope.

7

Planetary fields and dynamos

Ulrich R. Christensen

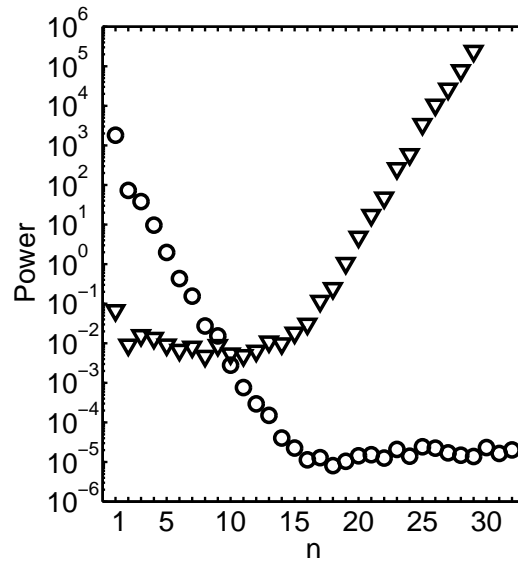


Fig. 7.1. Spatial power spectra of the geomagnetic field in 2004 according to the POMME model Maus et al. (2006) as function of spherical harmonic degree n at Earth's surface (circles) and at the core-mantle boundary (triangles; offset in amplitude). Note that structures of the core field corresponding to $n > 13$ are veiled by the crustal magnetic field, and that the apparent rise in the power spectrum does not reveal the properties of the deep geomagnetic field. Units are μT^2 for the surface field and mT^2 for the core field.

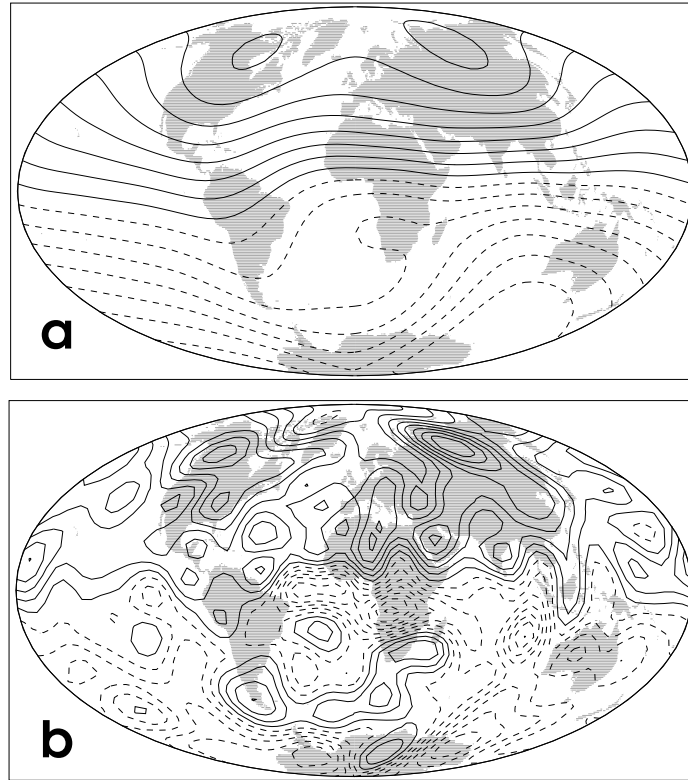


Fig. 7.2. Radial component of the geomagnetic field at the Earth's surface (a) and at the core-mantle boundary (b). Full lines for inward magnetic flux and dashed lines for outward flux. Contour intervals are arbitrary and different in the two panels.

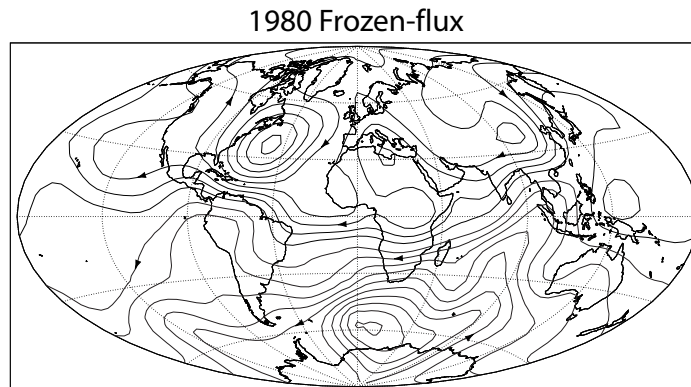


Fig. 7.3. Streamlines of the flow at the surface of the Earth's core inferred from the geomagnetic secular variation under the frozen flux assumption for the year 1980. Adapted from Amit and Christensen (2008).

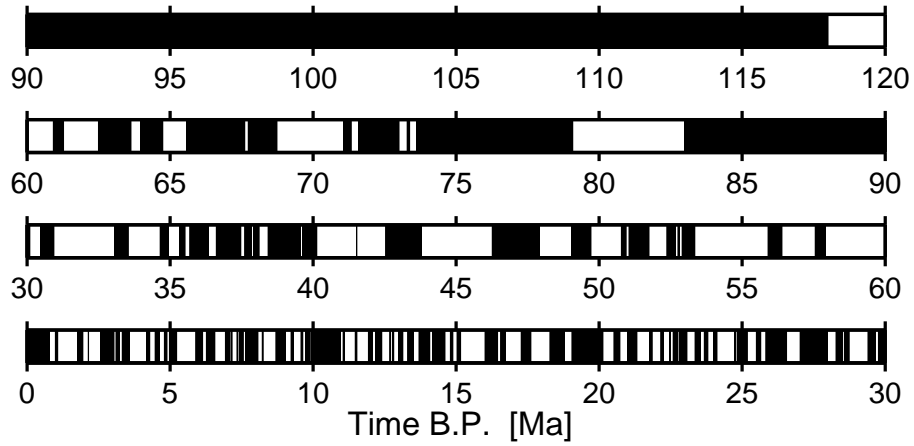


Fig. 7.4. Polarity of the geomagnetic magnetic field for the past 120 million years, with time running backward from left to right in each row (before present - B.P., i.e., 1950 - in units of millions of years). Dark regions indicate times when the dipole polarity was the same as today, in white regions it has been opposite.

Planetary fields and dynamos

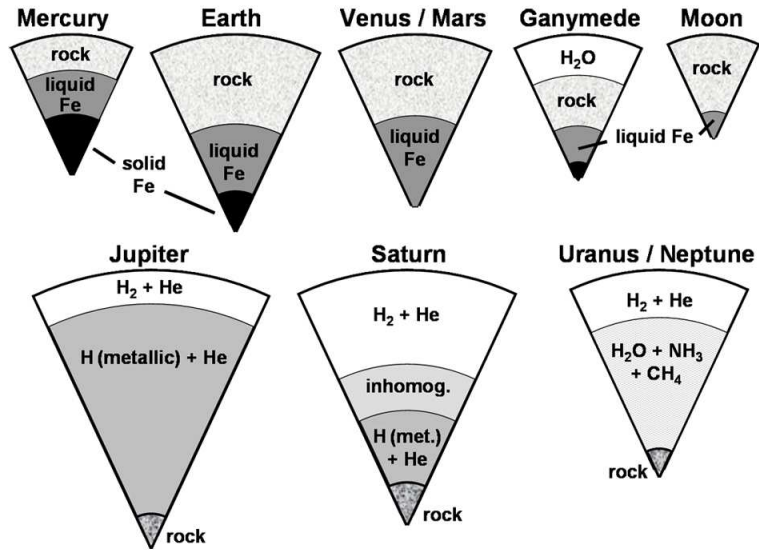


Fig. 7.5. Interior structure of planets with active or extinct dynamos. The top row shows the rocky (terrestrial) planets, and the bottom row the much larger gas planets. Larger planets are shown slightly larger, but relative sizes are not drawn to scale.

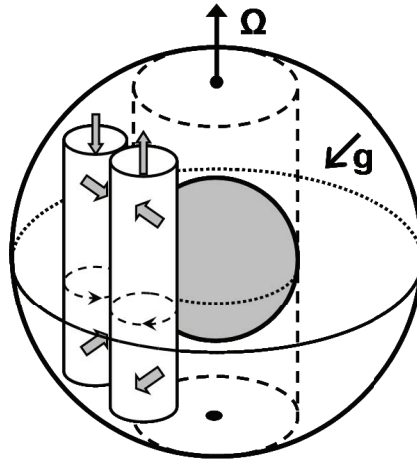


Fig. 7.6. Columnar convection in a rotating spherical shell near onset. The inner core tangent cylinder is shown by broken lines. Under Earth's core conditions the columns would be much thinner and very numerous.

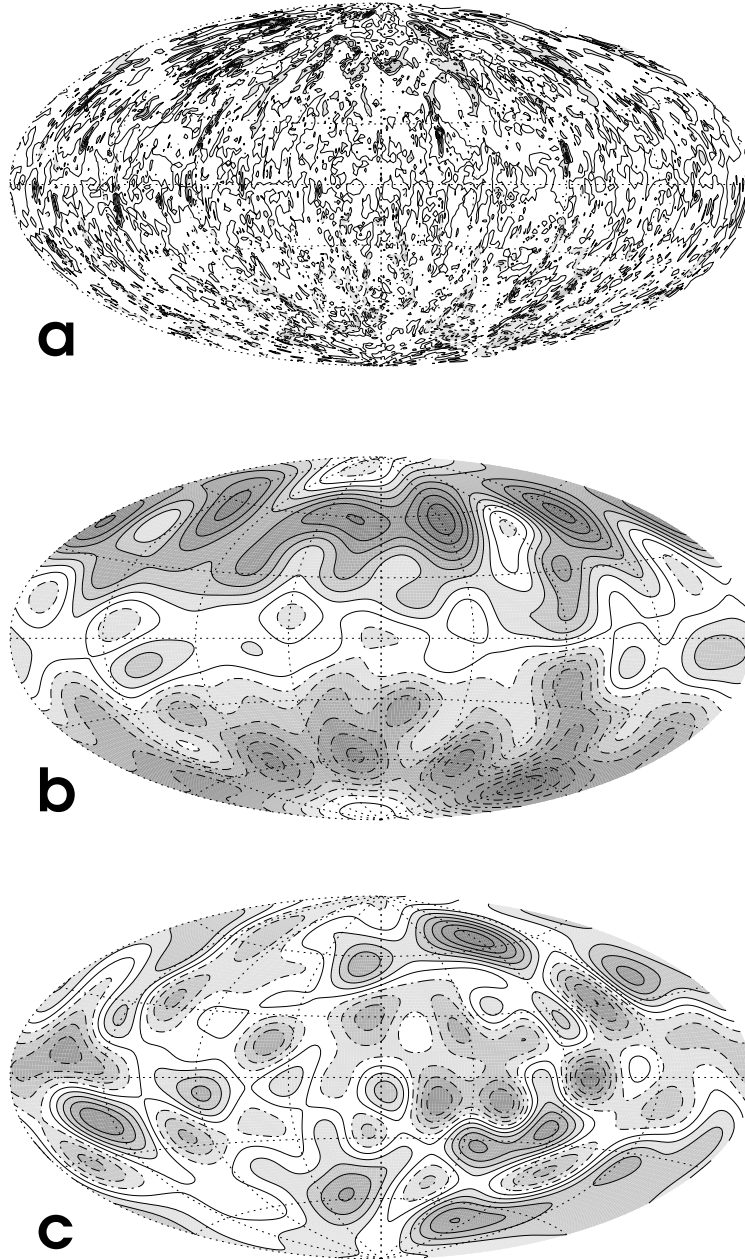


Fig. 7.7. Snapshots of the radial magnetic field component on the outer boundary from numerical dynamo models. Solid lines (red in the color version) are used for outward flux and dashed lines (blue in the color version) for inward flux (arbitrary contour steps in each panel). Grey-scale indicates absolute amplitude. (a) Model parameters $E=10^{-5}$, $R_a^* = 0.12$, $P_m = 0.8$, $P_r = 1$. (b) Same field low-pass filtered to harmonic degrees $n < 14$. (c) Model parameters $E=10^{-5}$, $R_a^* = 0.17$, $P_m = 0.5$, $P_r = 1$, low-pass filtered. R_m is approximately 900 in both cases; $R_{o\ell}$ is 0.125 in (a,b) and 0.19 in (c). See also the color plate section.

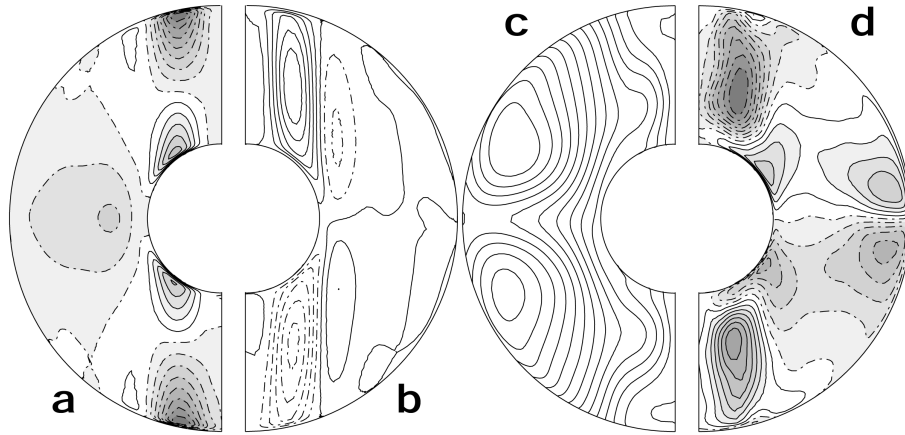


Fig. 7.8. Time-averaged axisymmetric components of velocity and magnetic-field components for a planetary dynamo model with $R_a^* = 0.225$, $E = 3 \times 10^{-4}$, $P_r = 1$, $P_m = 3$, $R_m \approx 250$ and $R_{o\ell} \approx 0.1$. The grey-scale indicates absolute intensity. (a) Azimuthal velocity, broken lines are for retrograde flow, (b) streamlines of meridional velocity, full lines for clockwise circulation, (c) poloidal magnetic field lines, (d) azimuthal (toroidal) magnetic field, broken lines westward directed field.

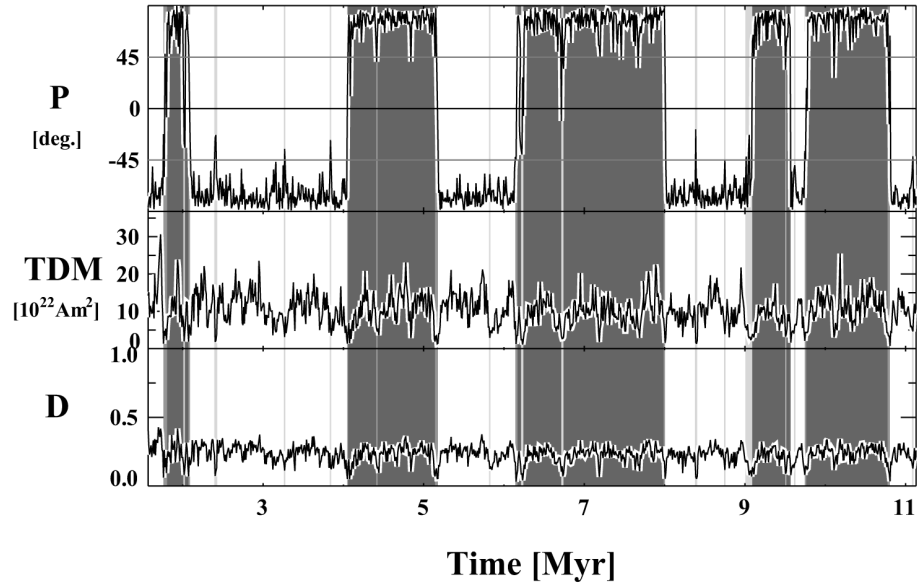


Fig. 7.9. Evolution of the dipole tilt for a modeled planetary magnetic field with respect to the equator (P), the true dipole moment (TDM), and the dipole strength relative to the total field strength at the core mantle boundary (D) for a dynamo model with $E = 10^{-3}$, $R_g^* = 0.5$, $P_m = 10$, $P_r = 1$. The present TDM of the geomagnetic field is $8 \times 10^{22} \text{ Am}^2$. Dark and light bands indicate polarity intervals. From Christensen (2009), courtesy of Johannes Wicht.

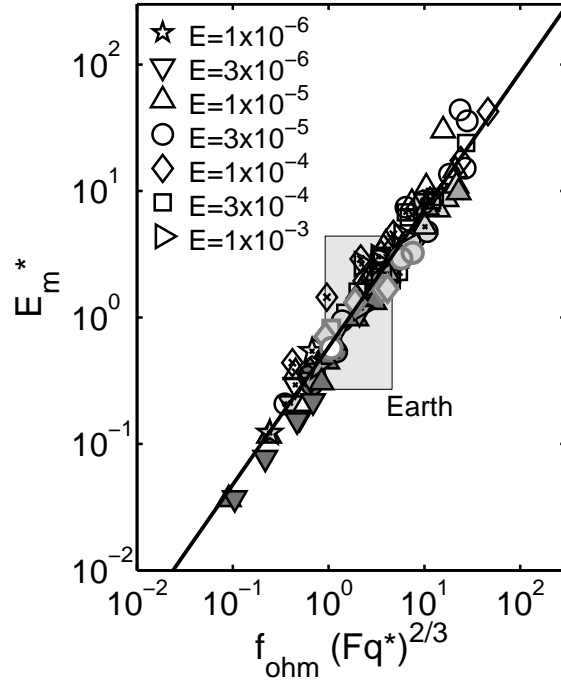


Fig. 7.10. Non-dimensional magnetic energy density in numerical dynamo models versus 2/3-power of the non-dimensional available energy flux. Symbol shape indicates Ekman number (Eq. 7.11), shading of the symbols magnetic Prandtl number (Eq. 7.13); darker means a lower value. Crosses inside the main symbol indicate $Pr > 1$ and circles indicate $Pr < 1$. Symbols with black edges are models driven by an imposed temperature contrast, those with grey edges are for compositional convection. The line represents the fit for a forced slope of one, equivalent to an exponent of 2/3 in Eq. (7.17). The location of the geodynamo in the diagram is shown by the grey rectangle.

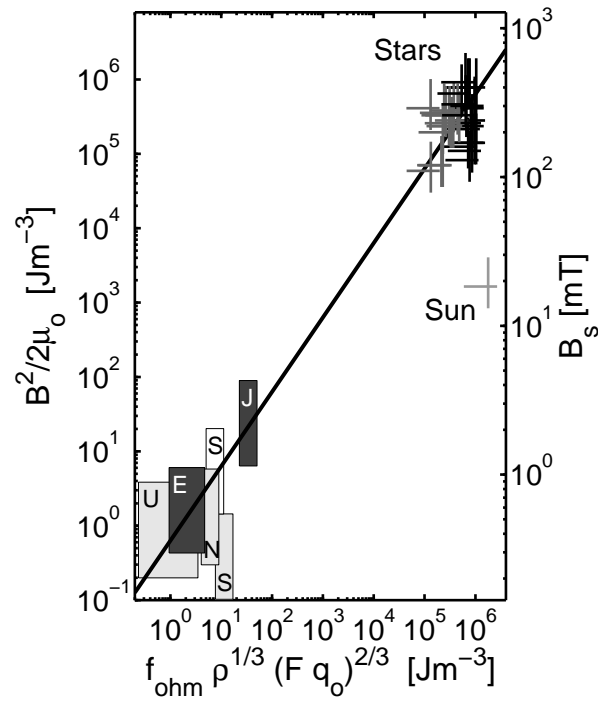


Fig. 7.11. Magnetic energy density in the dynamos of planets and certain stars versus the predicted dependence on a function of available energy flux and density. E: Earth; J: Jupiter; S: Saturn; U: Uranus; N: Neptune. The grey rectangle for Saturn is for a dynamo boundary at $0.62R_p$ and the white rectangle for $0.4R_p$. Black crosses for rapidly rotating main-sequence stars of low mass and grey crosses for classical T Tauri stars. The scale on the right is the average field strength (or flux density) at the surface of the dynamo. The black line is taken from Fig. 7.10 and converted here to physical units.

8

**The structure and evolution of the 3D
solar wind**

John T. Gosling

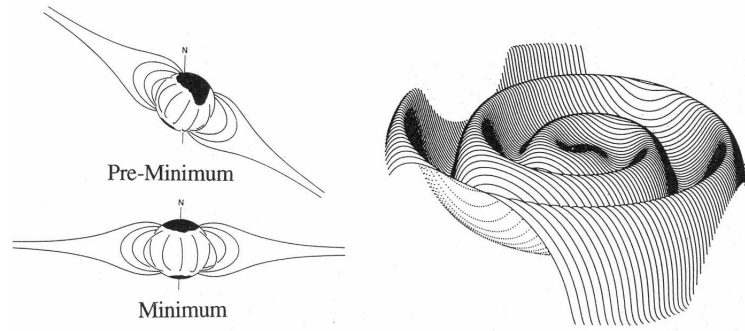


Fig. 8.1. *Left:* Schematic illustrating the changing tilt of the solar magnetic dipole and related coronal structure relative to the rotation axis of the Sun. (From Hundhausen, 1977.) *Right:* Idealized configuration of the heliospheric current sheet in the solar wind when the tilt of the solar magnetic dipole is substantial. (From Jokipii and Thomas, 1981).

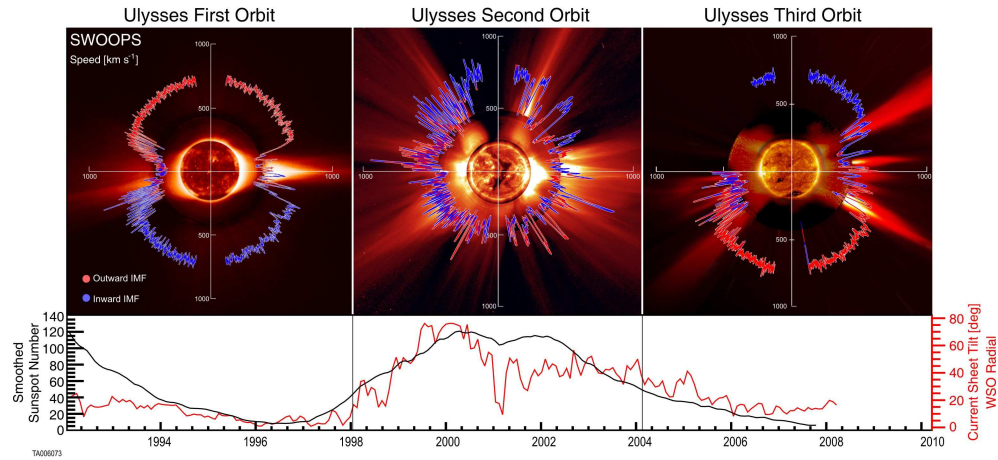


Fig. 8.2. *Top*: Polar plots of solar wind speed as a function of latitude for almost three complete Ulysses polar orbits about the Sun plotted over solar images characteristic of solar minimum (8/17/1996), solar maximum (12/07/2000), and again solar minimum (03/28/2006). Color-coding of the speed plots indicates the polarity of the IMF, blue inward directed and red outward directed. In each plot the earliest times are near aphelion on the left (nine o'clock position) and time progresses counterclockwise. The apparent differences in the scale of structures at low latitudes on opposite sides of each panel are artifacts associated with the fact that Ulysses changed latitude very rapidly near perihelion (1.34 AU) but very slowly near aphelion (5.41 AU). The brief low-speed interval near latitude 80°S in the third orbit plot was associated with Ulysses' encounter with the ion tail of comet McNaught (Neugebauer et al., 2007). The solar images from Sun center outward are from the Solar and Heliospheric Observatory (SOHO) Extreme Ultraviolet Imaging Telescope (Fe XII at 1950 nm), the Mauna Loa K-coronameter (700-950 nm), and the SOHO C2 white light coronagraph. *Bottom*: Contemporaneous values for the smoothed sunspot number (black) and the tilt of the heliospheric current sheet (red). (From McComas et al., 2008.)

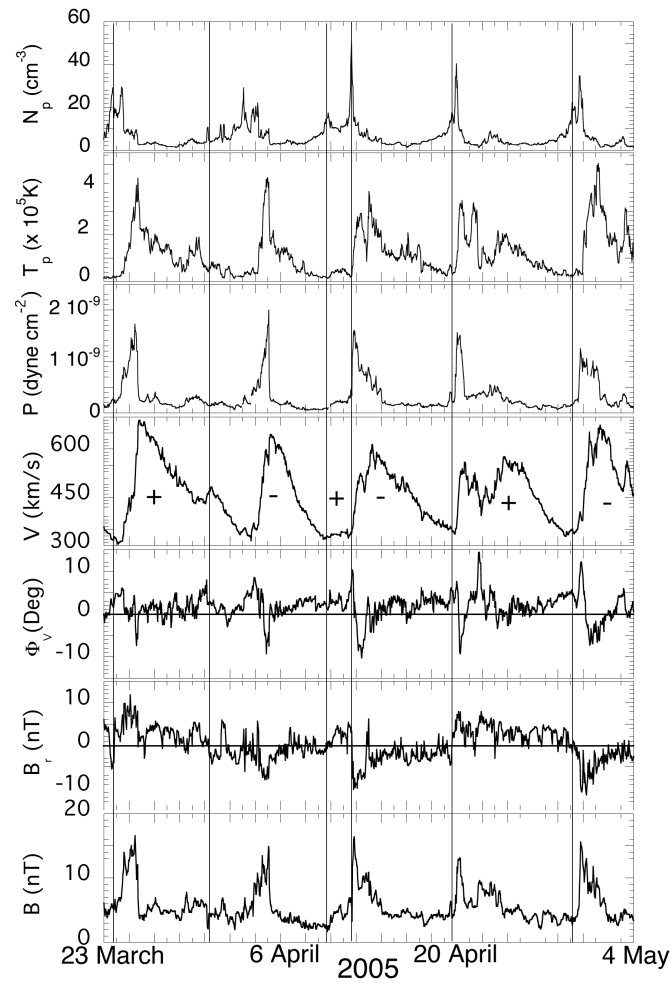


Fig. 8.3. Solar wind stream structure at 1 AU for a 42-d interval in 2005. From top to bottom the quantities plotted are 1-hr averages of the solar wind proton number density, proton temperature, total (field plus plasma) pressure, bulk flow speed, flow azimuth angle (positive in the sense of Earth's motion about the Sun), radial component of the HMF, and the HMF magnitude. Vertical lines mark crossings of the HCS, which were identified by changes in the suprathermal electron strahl flow polarity. Plus and minus signs in the fourth panel mark the magnetic polarities.

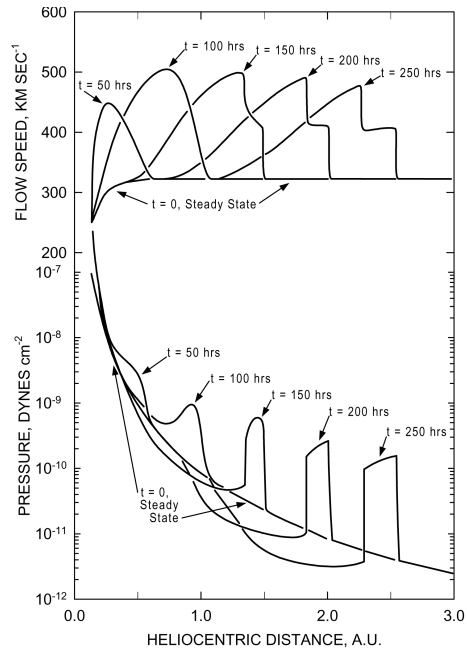


Fig. 8.4. Snapshots of solar wind flow speed and pressure as functions of heliocentric distance at different times during the outward evolution of a high-speed stream as calculated using a simple 1D gas-dynamic code. After obtaining a steady-state solar wind expansion that produced a flow speed of 325 km/s far from the Sun, a high-speed stream was introduced into the calculation by linearly increasing and then decreasing the temperature (and thus also the pressure) by a factor of four at the inner boundary at 0.14 AU over an interval of 100 h. (From Hundhausen, 1973.)

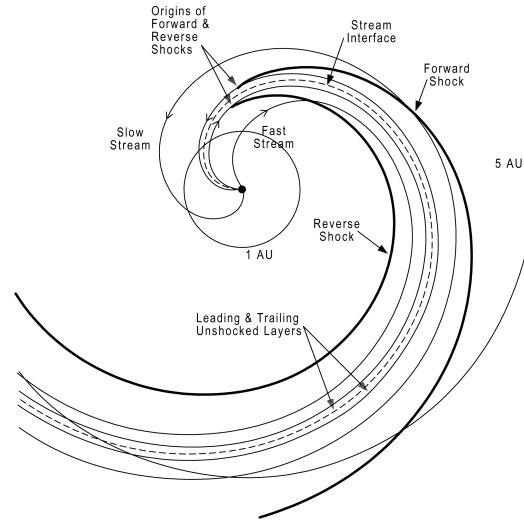


Fig. 8.5. Idealized schematic illustrating the basic structure of a corotating interaction region in the solar equatorial plane. The dashed line threading the middle of the corotating interacting region (CIR) denotes the stream interface and the solid heavy lines indicate the forward and reverse shocks. Plasma immediately surrounding the stream interface is compressed, but not shocked. (From Crooker et al., 1999.)

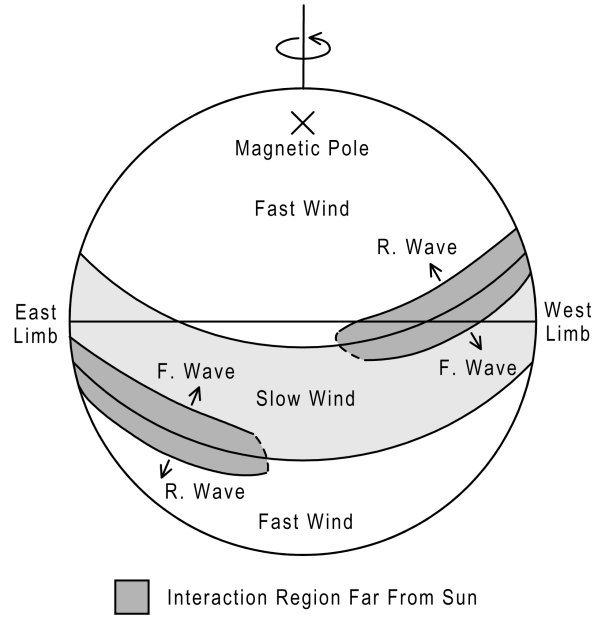


Fig. 8.6. Idealized sketch illustrating the origin of tilted CIRs in the solar wind in terms of a magnetic dipole tilted forward from the plane of the page in this sketch. The band of slow wind (light shaded region) girding the Sun at low latitudes is tilted relative to the heliographic equator in the same sense as is the heliospheric current sheet. The pattern of flow is established close to the Sun and the interaction regions (heavy shade) form well away from the Sun. (From Gosling et al., 1993.)

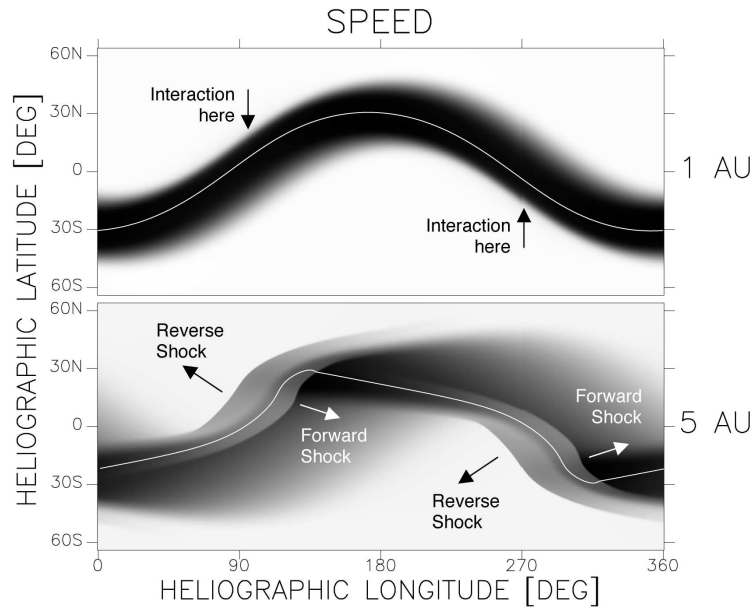


Fig. 8.7. Latitude-longitude gray-scale map of solar wind speed at 1 AU and 5 AU resulting from the 3D MHD simulation described in the text. Light (dark) shading indicates high (low) speed flow. The white line threading the speed plots is the heliospheric current sheet (HCS). In the 5 AU panel, the flow pattern has been shifted 90° in longitude to compensate for co-rotational drift between 1 and 5 AU. Corotating interacting regions (CIRs) at 5 AU appear as the two medium-tone diagonal features near 90° and 270° longitude. The abrupt speed changes bordering the CIRs are forward/reverse shock pairs. Note that the reverse shocks extend to higher latitudes than do the forward shocks. (Adapted from Pizzo and Gosling, 1994.)

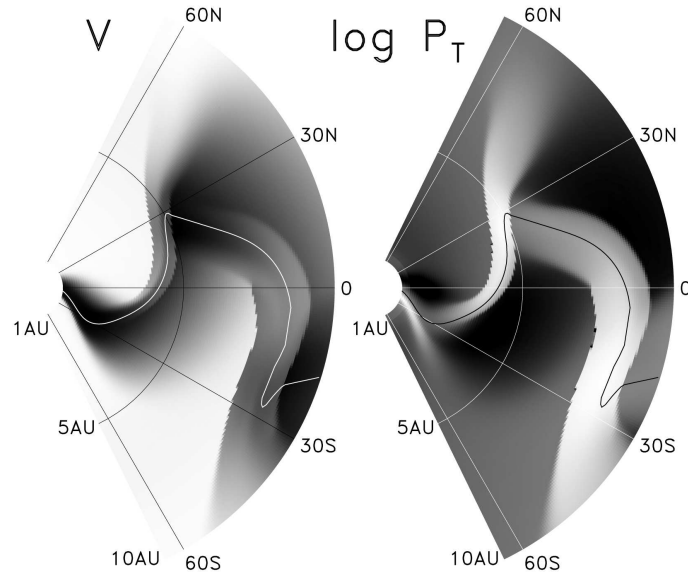


Fig. 8.8. Meridional gray-scale maps at a fixed longitude extending from 1 to 10 AU of the pattern of solar wind speed (left) and log of the total pressure (right) originating from a tilted dipole at the Sun. High (low) values of speed and pressure are indicated by light (dark) shading. The heliospheric current sheet HCS is the light (dark) line weaving back and forth across the equator in the speed (pressure) map. (From Pizzo and Gosling, 1994.)

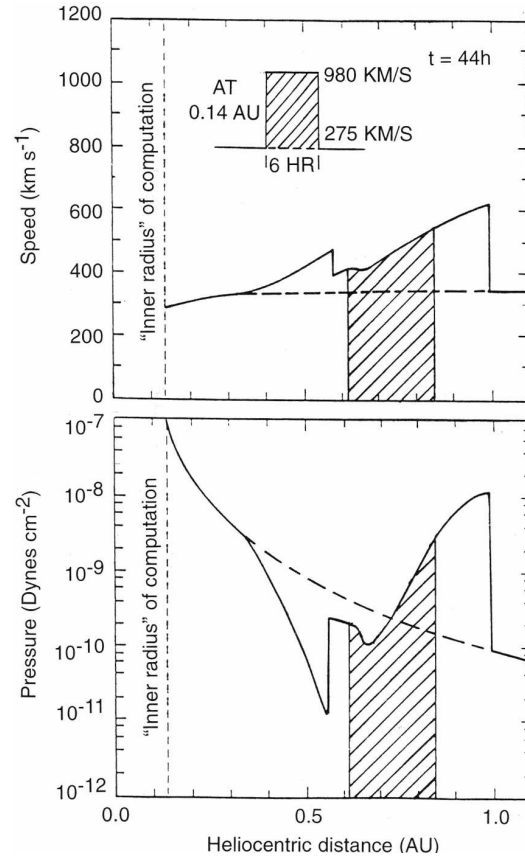


Fig. 8.9. A snapshot of solar wind speed and pressure as functions of heliocentric distance for a 1D gas-dynamic simulation of a solar wind disturbance driven by a fast CME/ICME at the time the leading edge of the disturbance reached 1 AU. The solid-dashed-solid curves indicate the steady state prior to introduction of the temporal variation in flow speed imposed at the inner boundary (0.14 AU) of the simulation shown at the top of the figure. Cross-hatching identifies material that was introduced with a speed of 980 km/s at the inner boundary, and therefore identifies the CME/ICME in the simulation. Temperature and pressure were held constant at the inner boundary during the introduction of the CME/ICME into the simulation. (Adapted from Hundhausen, 1985.)

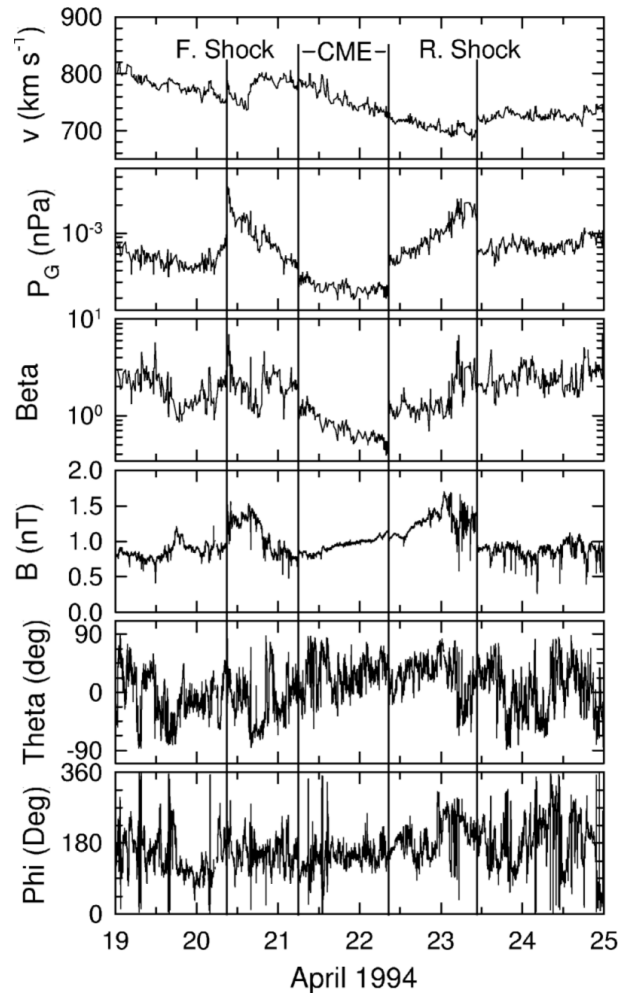


Fig. 8.10. Selected solar wind plasma and magnetic field parameters for a disturbance driven by an interplanetary coronal mass ejection (ICME) observed by Ulysses at 3.2 AU and 61°S . Parameters plotted from top to bottom are respectively the flow speed, gas pressure, plasma beta (ratio of gas to magnetic field pressure), magnetic field strength, and the polar and azimuthal angles of the field. Vertical lines bracket the CME/ICME and also indicate forward and reverse shocks bounding the disturbance. (From Gosling et al., 1994b.)

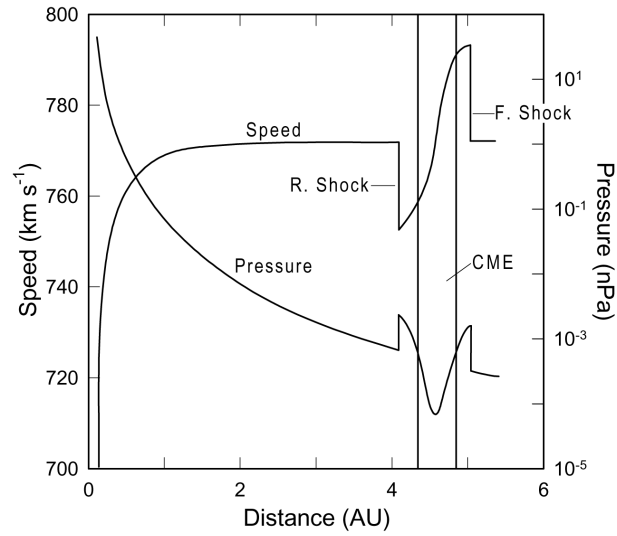


Fig. 8.11. A snapshot of solar wind speed and pressure as functions of heliocentric distance for a simulated (1D, gas-dynamic) ICME-driven disturbance that has just arrived at 5 AU. After establishing a steady state flow of 760 km/s at large heliocentric distances, the disturbance was initiated at 0.14 AU by increasing the density by a factor of 4 in a bell-shaped pulse of 10 hours duration while holding the speed and temperature constant there. Vertical lines bracket the plasma introduced into the simulation with higher density and thus identify the ICME in the simulation. (From Gosling et al., 1994b.)

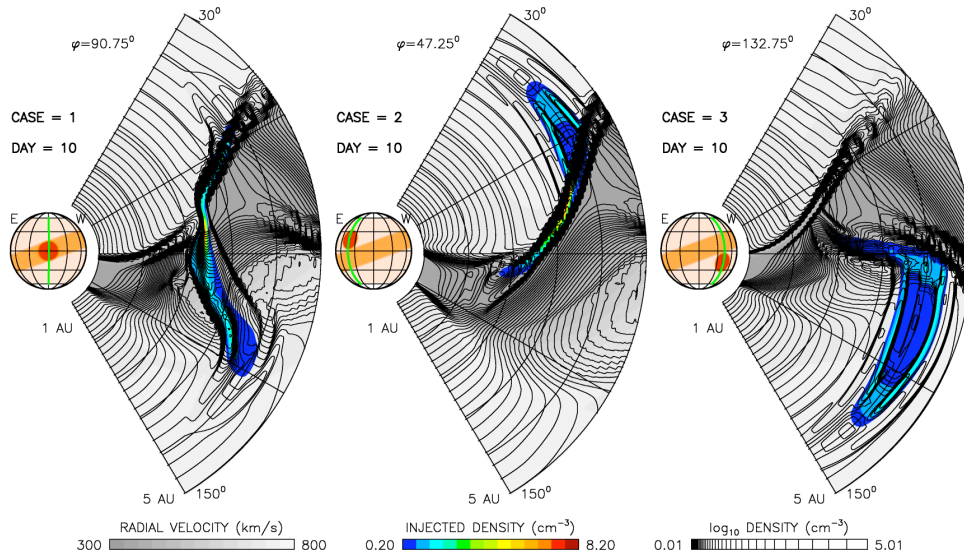


Fig. 8.12. Meridional plane cross-sections of three ICME-driven disturbances 10 days after launch at the inner boundary of a 3D gas-dynamic simulation. In the original color version of this figure radial velocity is indicated by a grey-scale, density within the ICME is indicated in color, and log of the density in the ambient wind is indicated by the contour lines. The three cases shown are (left) an ICME injected at the equator within the band of slow wind, (center) an ICME injected to the east of the slow wind band, and (right) an ICME injected to the west of the slow wind band. In each case the ICME was injected as an over-pressured (factor of 8) plasma cloud having a speed identical to that of the high-speed wind. In the first case the pressure enhancement was achieved with density and temperature enhancements 2 and 4 times, respectively, that of the slow wind; in the latter 2 cases the over-pressure was achieved with a density enhancement 8 times that of the background fast flow. The clouds had identical 30° circular shapes and 12-h durations at the inner boundary of the simulations. The ambient slow wind band was tilted 20° relative to the heliographic equator. (From Odstreil and Pizzo, 1999.)

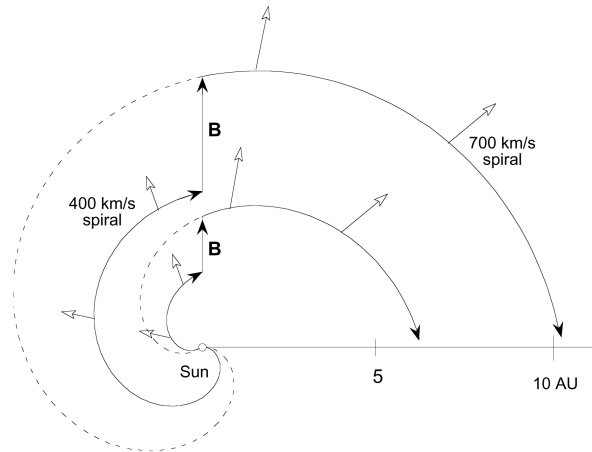


Fig. 8.13. Snapshots from above the north solar pole of a highly idealized magnetic field line in the solar equatorial plane shown at two different times on which a sudden and semi-permanent decrease in solar wind speed from 700 to 400 km/s occurred close to the Sun when the field line footpoint was at 0° clock angle on the trailing edge of a high-speed stream. The snapshots are obtained at successively later times when the field-line footpoint has rotated to clock angles of -130° and -270° , respectively. Dashed lines indicate the Parker spirals that would have resulted had the wind speed on the field line remained constant at 700 km/s. Open arrows indicate flow vectors. An ever-growing radially oriented kink in the field line develops at 0° clock angle connecting the pre-decrease and post-decrease 400 and 700 km/s spirals in this kinematic sketch. The sketch ignores dynamic effects associated with the rarefaction produced by a sudden drop in speed that serve to bend the radial field segment eastward, yet still produce a field line segment that is less tightly wound than is a Parker spiral field line. (From Gosling and Skoug, 2002.)

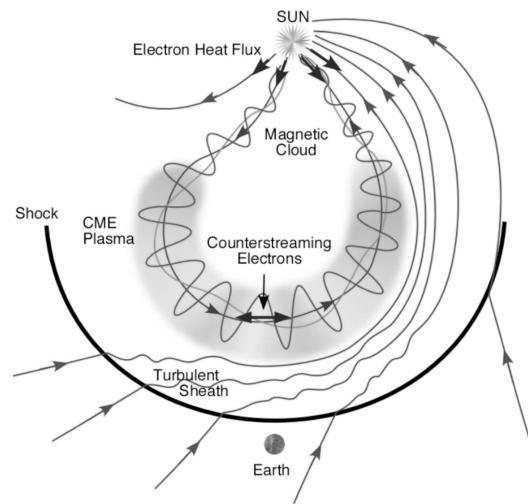


Fig. 8.14. An idealized 2D sketch of a solar wind shock disturbance produced by a fast ICME, depicted as a magnetic flux rope or magnetic cloud, running into slower wind ahead and directed toward Earth. The heavy curved line running in front of the ICME indicates the forward shock, the thin lines with small arrows indicate magnetic field lines, and the heavy arrows indicate the direction of the suprathermal electron strahl directed outward from the Sun. The ambient magnetic field is compressed by its interaction with the ICME and is forced to drape about it. (From Zurbuchen and Richardson, 2006.)

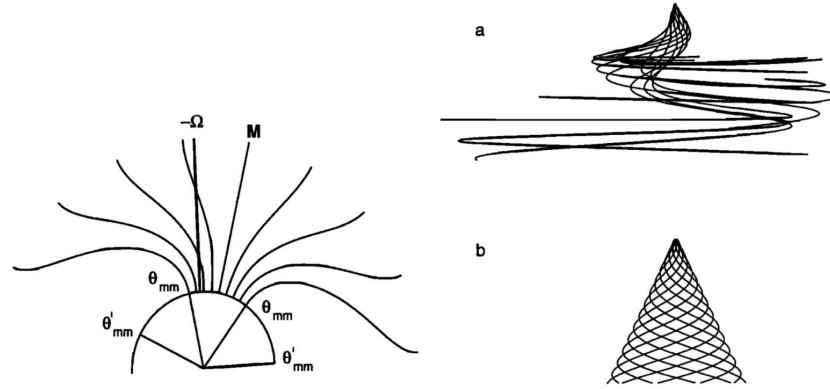


Fig. 8.15. *Left:* A schematic illustration of the expansion of magnetic field lines from a south-polar coronal hole centered on a dipole axis (\mathbf{M}) tilted relative to the solar rotation axis (parallel to $-\Omega$). θ_{mm} is the magnetic co-latitude of the last field lines that extend from the coronal hole out into the heliosphere and θ'_{mm} is the magnetic co-latitude of those same field lines where they extend nearly radially outward into the heliosphere. All field lines drawn thread the high-speed wind. *Right:* HMF field lines that originate from 70°S latitude, projected onto a meridional plane. (a) The field lines resulting from a combination of differential rotation and a rigidly rotating dipole in Fisk's model. (b) The field lines in Parker's model. (Adapted from Fisk, 1996.)

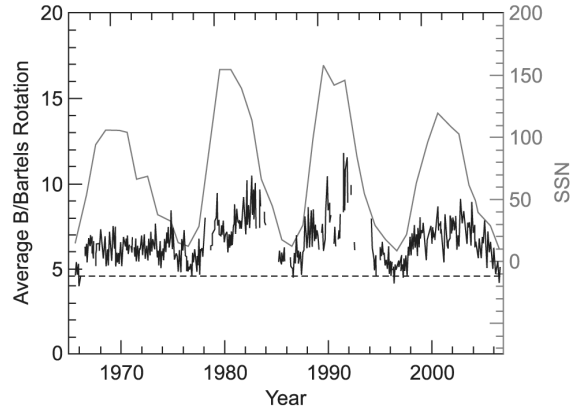


Fig. 8.16. Bartels (27-d) rotation averages of the magnitude of the HMF in the ecliptic plane (black line) from 1965 to 2006 covering most of sunspot cycles 20 – 23 along with the smoothed sunspot number (grey line). (From Svalgaard and Cliver, 2007).

9

The heliosphere and cosmic rays

J. R. Jokipii

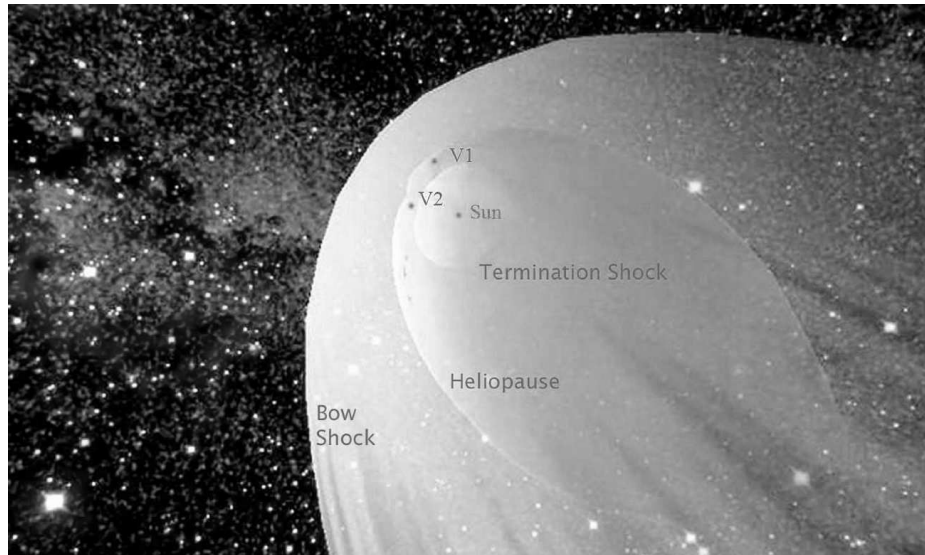


Fig. 9.1. Artist's rendition of the heliosphere, including the positions of the Voyager 1 and 2 spacecraft in 2009. Copyright P.C. Frisch (University of Chicago).

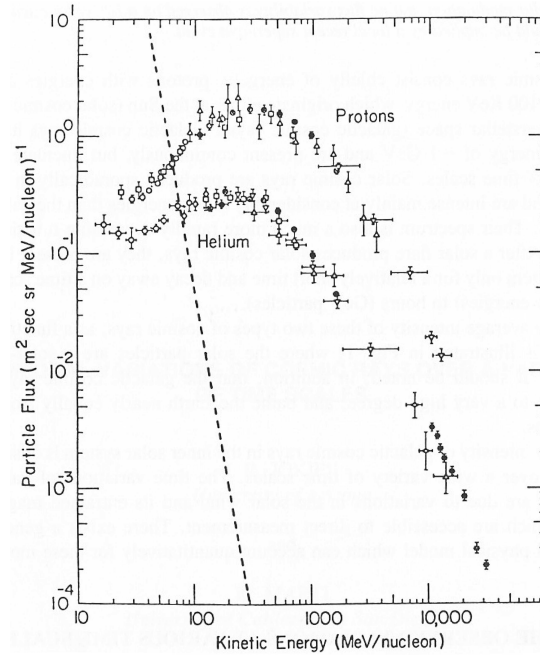


Fig. 9.2. Observed spectra of cosmic rays at Earth. The data points show the quiet-time spectrum of galactic cosmic-ray protons and helium nuclei, and the steeper, dotted line is a characteristic spectrum of solar energetic particles for an average event in the solar cycle. Different symbols reflect results from different instruments; see Jokipii (1991) for details. See Fig3. 3.1 and 9.1 in Volume I for the continuation of the particle spectra from different sources at lower energies.

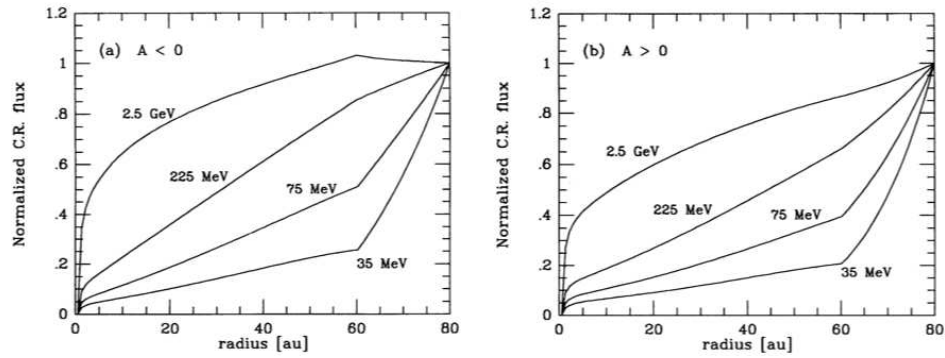


Fig. 9.3. Model calculation for the radial variation of cosmic rays for field configurations in which the magnetic field is either inward (a: $A < 0$) or outward (b: $A > 0$) in the northern hemisphere of the heliosphere for an early model with the radius of the termination shock of 60 AU. Observations from spacecraft generally confirm this picture. The intensity decreases inward away from the particle source (see Sect. 9.5.2 in Vol. II) and goes to zero near the Sun because of absorption by the solar atmosphere. From Jokipii et al. (1993).

The heliosphere and cosmic rays

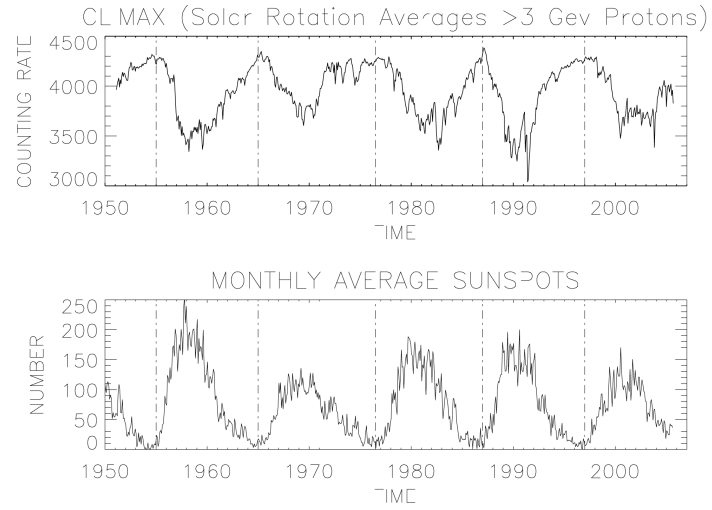


Fig. 9.4. The modulation of galactic cosmic rays during five sunspot cycles. Note the alternation in the cosmic-ray maxima between sharply peaked and more-rounded shapes. Data courtesy of the University of Chicago.

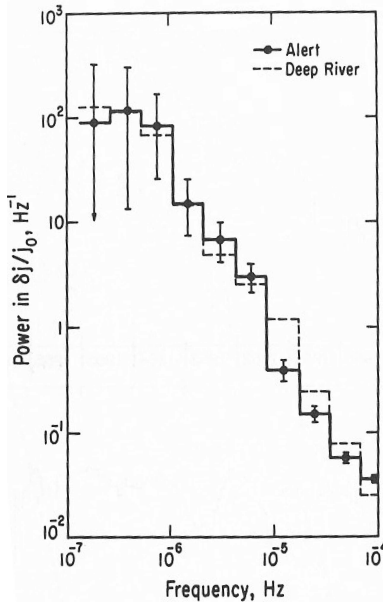


Fig. 9.5. The temporal power spectrum of the observed variations of ≈ 1 GeV galactic cosmic rays at Earth from Jokipii and Owens (1973). Note that 1 Hz or one cycle per second is $\approx 3 \times 10^7$ cycles per year.

The heliosphere and cosmic rays

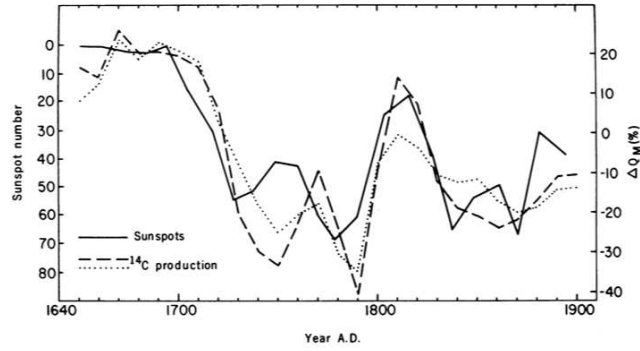


Fig. 9.6. Carbon-14 concentrations around the time of the Maunder minimum. Shown are the sunspot number (inverse scale) and the production rate of ^{14}C inferred from tree-ring studies. During the Maunder minimum period in the 1600s, when the sunspot number was lowest, the ^{14}C production rate was highest. The 11-y running mean sunspot number is given by the solid line (left axis) and the ^{14}C measurements are given with the dotted line (assumed residence time 60 y) and the dashed line (assumed residence time 20 y), both with the right axis. From Stuiver and Quay (1980).

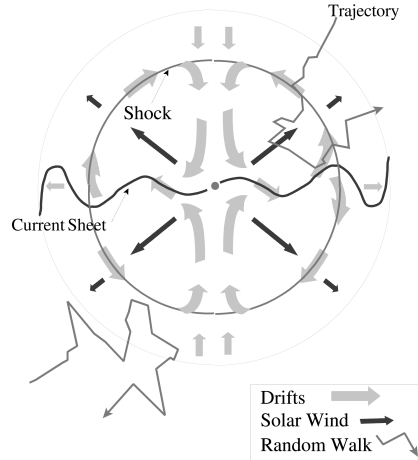


Fig. 9.7. Schematic illustration of the motions of galactic and anomalous cosmic rays in the heliosphere. The directions of the arrows are for a sunspot cycle when $A > 0$ (northern hemisphere magnetic field out). The direction of the drift arrow would be reversed for the opposite sign of the magnetic field. The galactic cosmic rays enter from the outer boundary and the anomalous cosmic rays are accelerated at the termination shock. Both are affected by the shock and the current sheet.

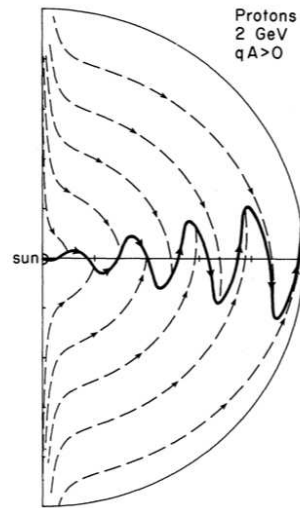


Fig. 9.8. Cosmic-ray drift motions in a Parker spiral magnetic field with a current sheet. The arrows shown correspond to the time when the northern-hemisphere heliospheric magnetic field is outward from the Sun (1975, 1996) for positively charged particles. The arrows reverse for the alternate sign of the magnetic field (1986, 2007) and for the opposite sign of the particle's electric charge. From Jokipii and Thomas (1981).

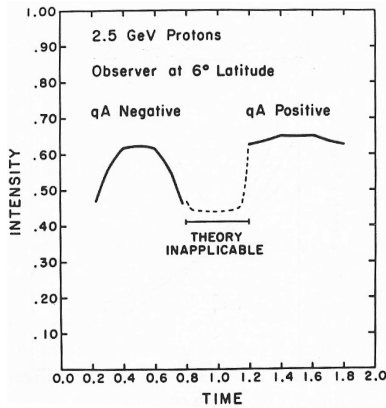


Fig. 9.9. Illustration of the results of a simple model calculation for the galactic cosmic ray flux where only the current sheet tilt and the sign of the magnetic field varied. The model is inapplicable near sunspot maximum. The plots are for cosmic-ray ions (with charge $q > 0$) which comprise the majority of observed cosmic rays. From Jokipii and Thomas (1981).

The heliosphere and cosmic rays

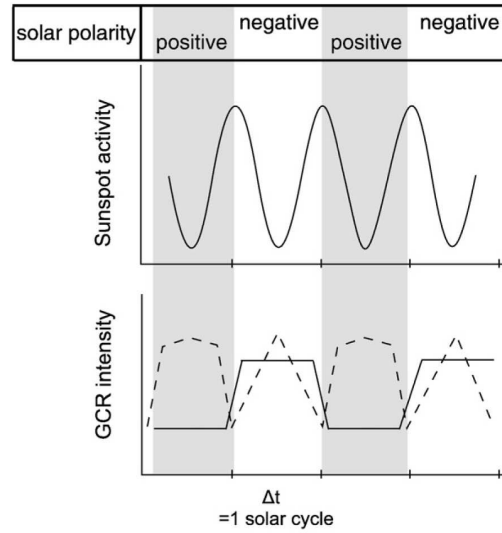


Fig. 9.10. Model results presented by Miyahara et al. (2008), showing the two effects of the heliosphere on galactic cosmic rays. Sunspot activity is represented by the upper curve. The solid line in the lower curve represents the effect of the changing sign of the heliospheric magnetic field (positive and negative for $A > 0$ and $A < 0$, respectively, as defined in the caption to Fig. 9.3; plots are shown for positively charged ions). The dashed line in the lower panel is the normal situation which combines both the sunspot activity and the change in sign of the heliospheric magnetic field.

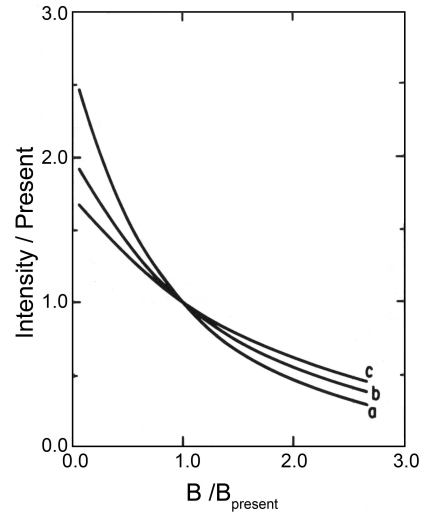


Fig. 9.11. Illustration of the computed value of the cosmic-ray intensity for various particle energies (a: 0.5 GeV, b: 1 GeV, and c: 1.5 GeV) as a function of the magnetic field strength. From Jokipii and Marti (1986).

The heliosphere and cosmic rays

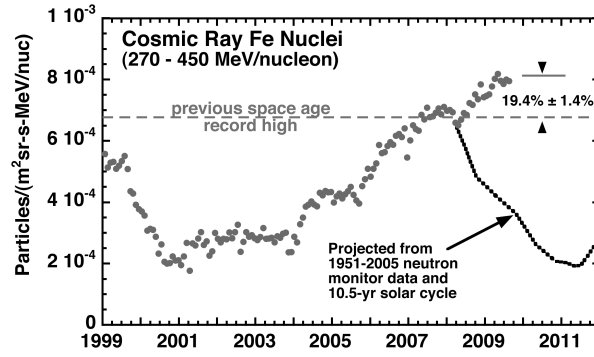


Fig. 9.12. Intensity of cosmic-ray iron from the NASA ACE spacecraft. Note that the rate increases beyond the previous space high, with no sign as yet of leveling out. Courtesy R.A. Mewaldt.

10

**Solar spectral irradiance: measurements
and models**

Judith L. Lean and Thomas N. Woods

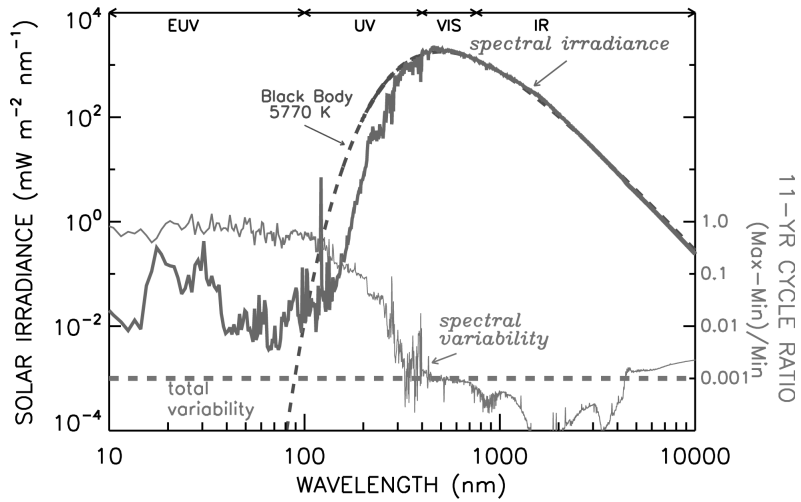


Fig. 10.1. Comparison of the solar spectrum and the black body spectrum for radiation at 5770 K (the approximate temperature of the Sun's visible surface). Also shown is an estimate of the variability of the solar spectrum during the 11-y solar cycle, inferred from measurements (at wavelength below 400 nm) and models (at longer wavelengths) and, for reference (dashed line), the solar cycle 0.1% change in the total solar irradiance.

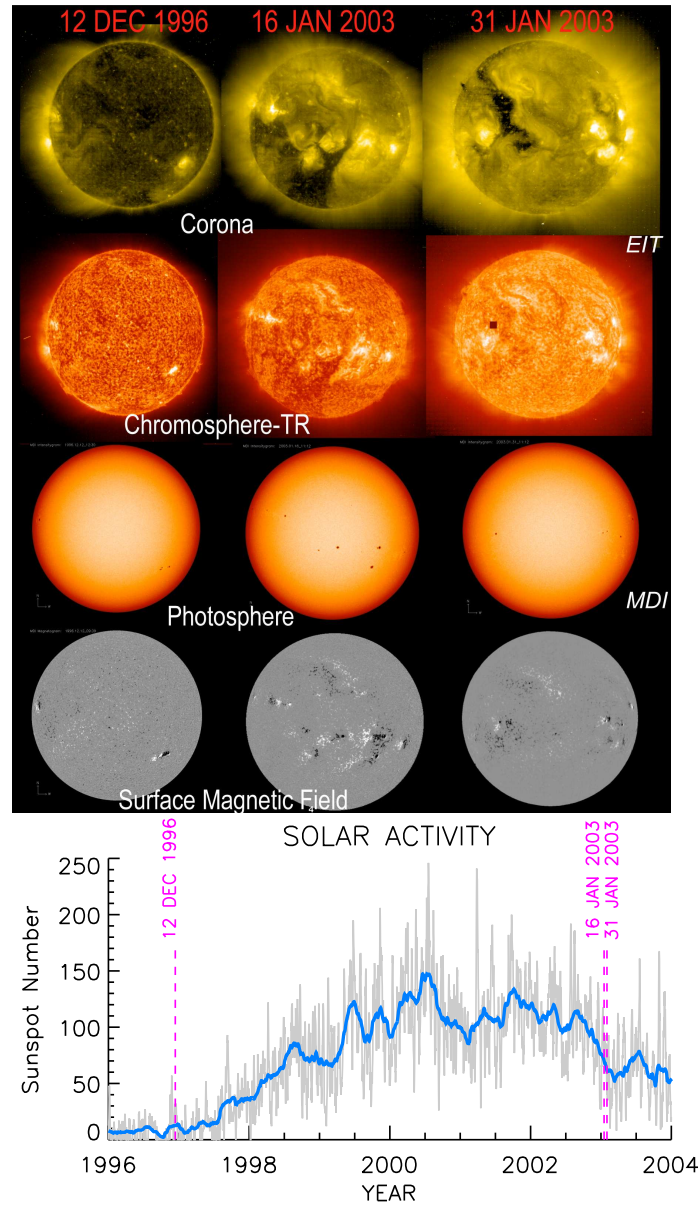


Fig. 10.2. Images of the Sun's surface seen in magnetic flux (bottom row) and visible light (second row) are compared with images of the solar chromosphere/transition region (third row) and corona (top row). The images, made using different wavelengths of the solar spectrum, are compared at different levels of solar activity. The images in the left column (December 1996) are typical of quiet conditions during solar activity minima, and those on the right illustrate conditions near high solar activity (January 2003) at two different phases of the Sun's 27-day synodic rotational cycle. The bottom plot shows the sunspot number time series.

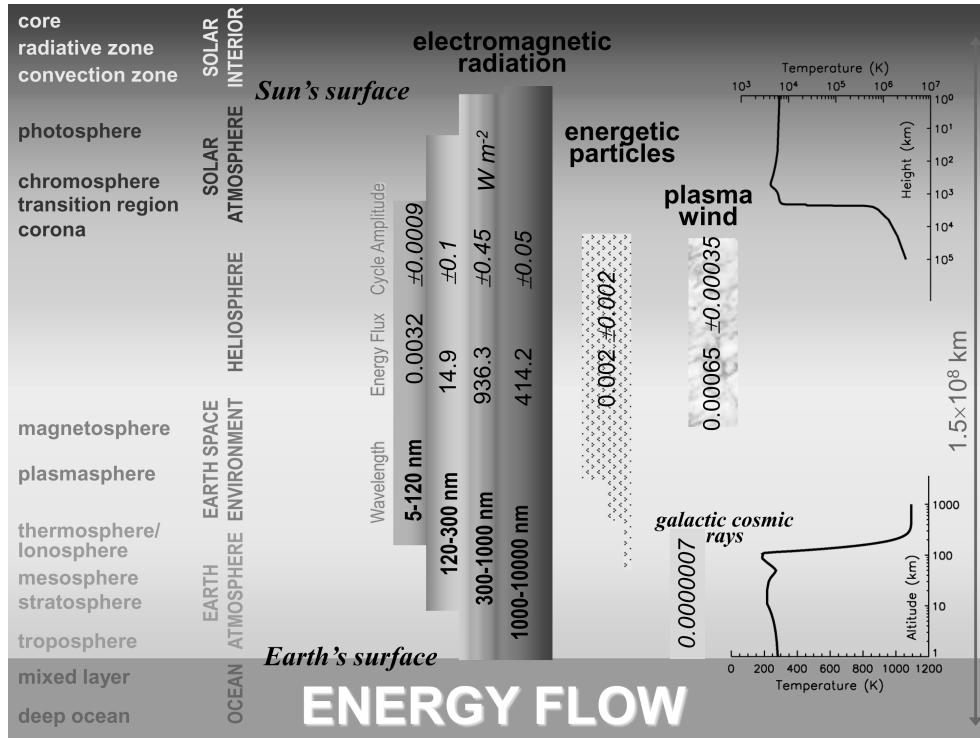


Fig. 10.3. The flow of energy from the Sun to the Earth is compared for photons in four different wavelength bands, energetic particles, and the plasma wind. The numbers are approximate energies with their variations (following the ± symbol) during an 11-y solar activity cycle, in Wm^{-2} . Visible radiation connects the surfaces of the Sun and Earth while ultraviolet radiation connects their atmospheres. Particles and plasma connect the outer solar atmosphere primarily with Earth's magnetosphere and high-latitude upper atmosphere. Shown on the right are approximate temperatures of the various Sun and Earth regimes. (Adapted from Lean, 2005)

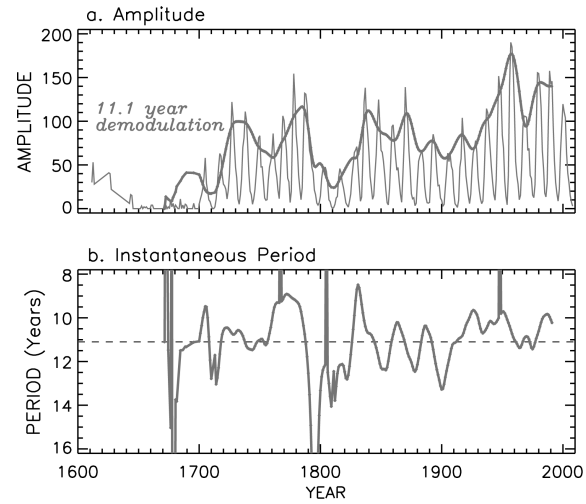


Fig. 10.4. Annual values of the historical sunspot record during the past four centuries (top panel), indicating the evolution of the 11-y activity cycle. The amplitude of the cycle obtained by demodulation of the annual time series is also shown. In the bottom panel, the instantaneous period of the cycle, similarly obtained from demodulation, indicates the inconstancy of the nominal "11-y" sunspot cycle period.

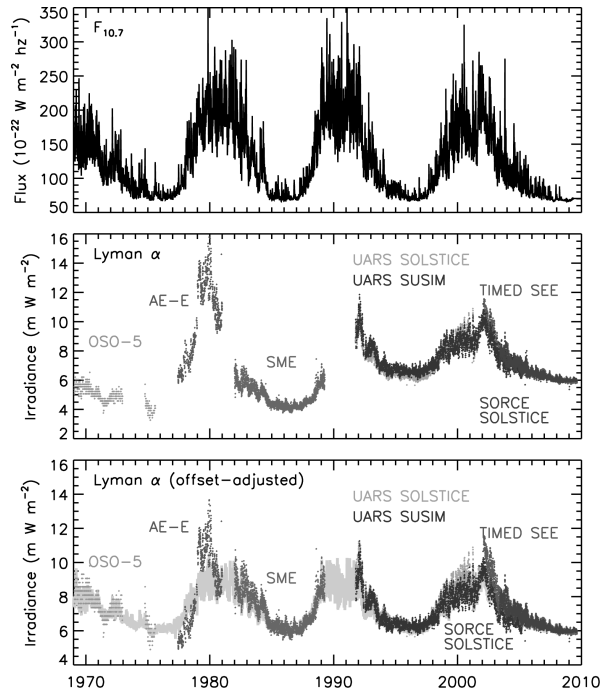


Fig. 10.5. The longest and most widely used index of solar extreme ultraviolet (EUV) irradiance variability is the 10.7 cm radio flux, $F_{10.7}$, whose daily values are shown in the top panel for more than three solar cycles. Observations of the Lyman α irradiance, the strongest emission line in the solar UV spectrum, are shown in the middle panel on their "native" calibration scales. Adjusting individual Lyman α observations by constant offsets to account for differences in absolute calibrations, in the bottom panel, reveals more clearly the actual Lyman α solar cycle variability. Short-term rotational modulation variations are superimposed on both the 10.7 cm and Lyman α time series.

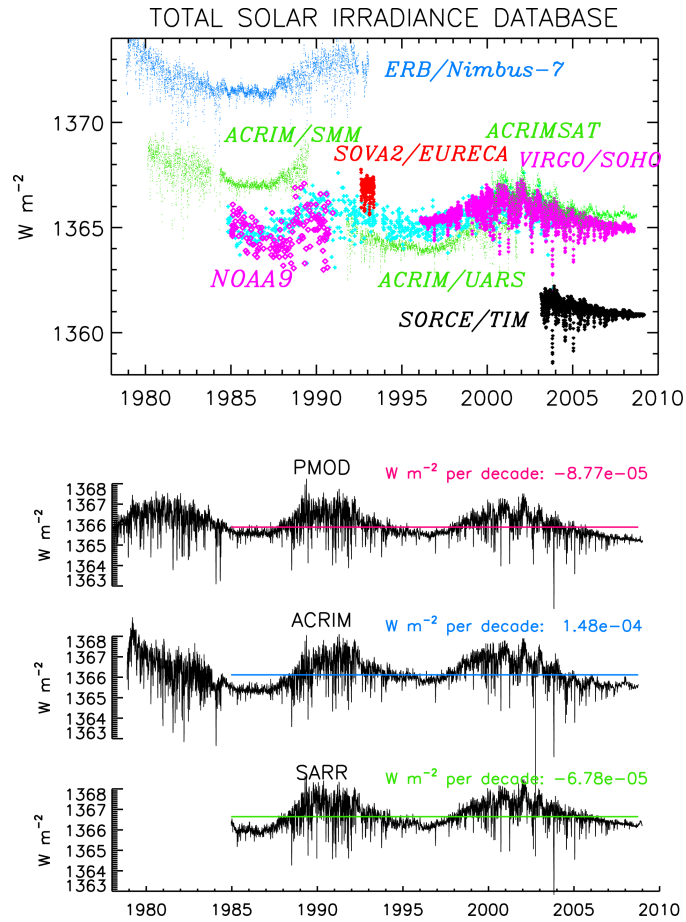


Fig. 10.6. Individual measurements of the total solar irradiance, made since 1978 from a variety of space platforms, are compared on their "native" calibration scales in the top panel. Shown in the lower three panels are different composite records of total solar irradiance constructed from the observational database, using varying assumptions about calibration offsets and in-flight sensitivity changes (PMOD: C. Fröhlich; ACRIM: R. C. Willson; SARR: S. Dewitte). For quantitative comparison, the slopes of the time series are also indicated.

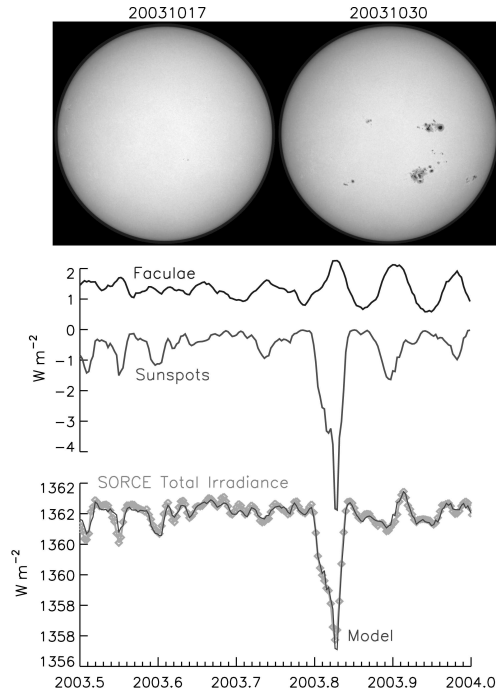


Fig. 10.7. Continuum light solar images made by the Michelson Doppler Imager (MDI) instrument on SOHO are compared for 17 and 30 October 2003, when total solar irradiance underwent one of the largest decreases observed in the space era. Shown in the lower panel are the SORCE/TIM daily mean observations (symbols), compared with an empirical variability model developed from sunspot and facular influences. The middle panel compares the respective bolometric facular brightening (upper curve) and sunspot darkening (lower curve) that together produce the changes in total solar irradiance observed by TIM, using linear scaling to determine their relative contributions.

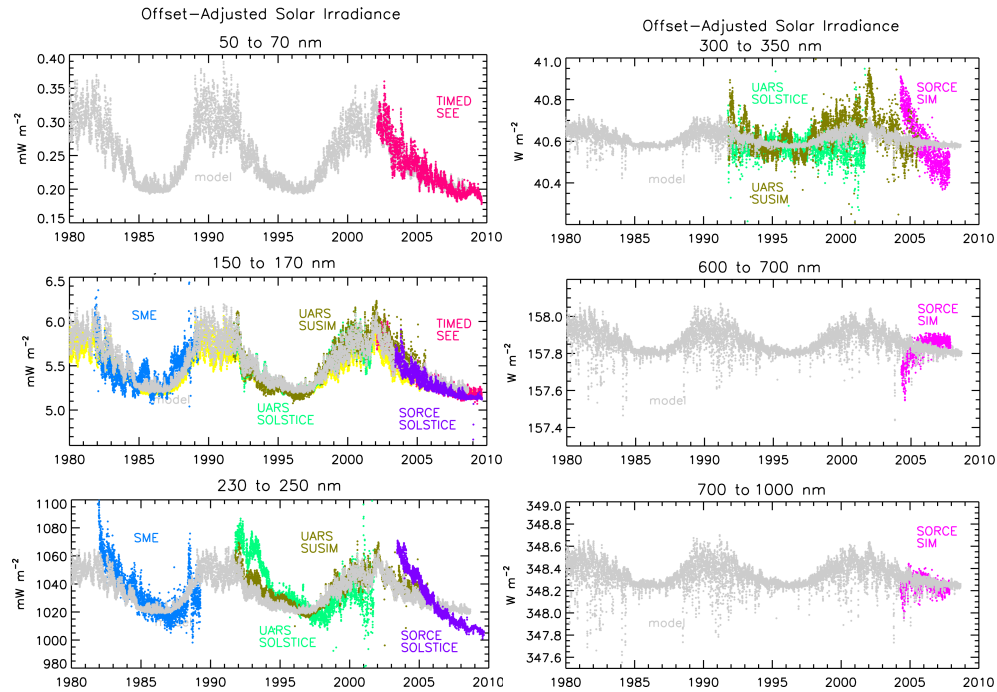


Fig. 10.8. Assorted space-based observations made of the solar spectral irradiance during the past three solar cycles are compared in selected wavelength bands. From top left to bottom right: EUV (50-70 nm), FUV (150-170 nm), MUV (230-250 nm), NUV (300-350 nm), visible (600-700 nm), and IR (700-1000 nm); the curves shown have offset-adjustments to account for their different absolute calibration scales. Also shown, as the grey time series, are models of the irradiance variations in the same wavelength bands, derived by scaling the observed rotational modulation variations to the Mg (and $F_{10.7}$ for the EUV band) proxy indicators. Note the lack of daily measurements shortward of 110 nm until TIMED SEE observations commenced in 2002, and longward of 400 nm until SORCE SIM observations commenced in 2003.

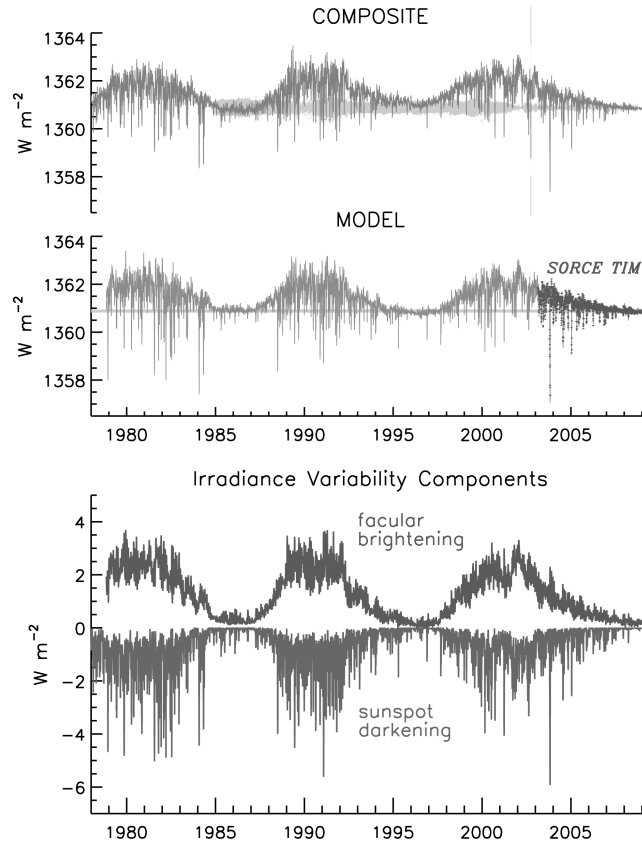


Fig. 10.9. Shown in the upper panel is a record of total solar irradiance obtained as an average of three different observational composites (shown separately in Figure 10.6). In the second panel are irradiance variations estimated from an empirical model that combines the two primary influences of facular brightening and sunspot darkening. The symbols indicate direct observations made by the TIM instrument of the SORCE mission, used to determine the relative sunspot and facular components in the model, shown separately in the lower panel.

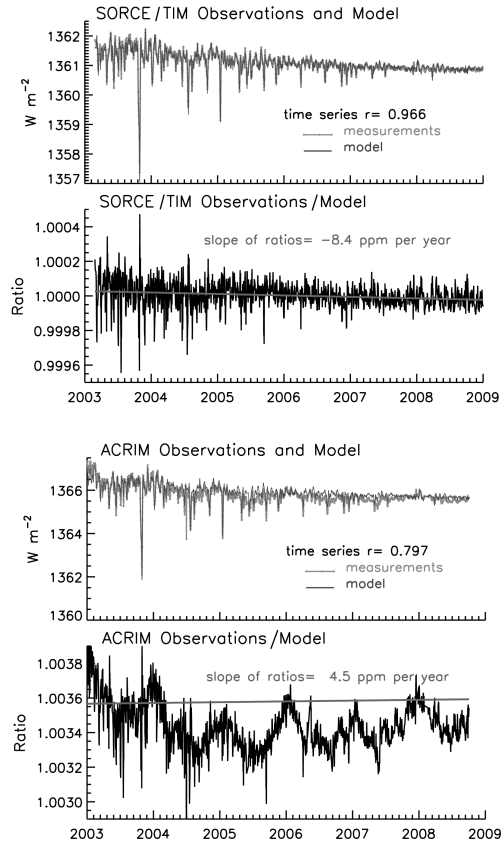


Fig. 10.10. A model of total solar irradiance variations, obtained from multiple regression of sunspot and facular indices with the SORCE/TIM observations, compared in the top panel with the direct TIM measurements, explains a large fraction (93%) of the observed variance. The second panel shows the ratios of the observations and model, indicating that the slope of the ratios is within the TIM long-term precision. In the two lower panels, the same total irradiance variability model is compared with the ACRIM observations, the ratios indicating significant, fluctuating deviations not present in either the model or the TIM measurements, and therefore likely of instrumental origin.

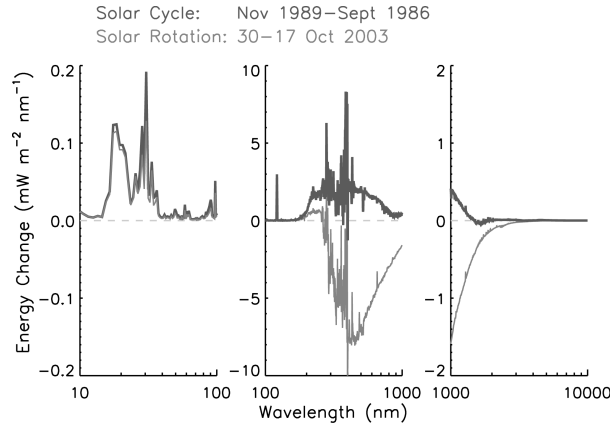


Fig. 10.11. Estimated changes in solar spectral irradiance are shown across the electromagnetic spectrum, from the EUV to the IR, for both the 11-y solar activity cycle (maximum in November 1989 and minimum in September 1986) and the 27-day solar rotational cycle (peak on October 30 and valley on October 17). These results indicate how the solar cycle and rotation cycle variations are in-phase at short wavelengths (below about 300 nm) and out of phase at longer wavelengths.

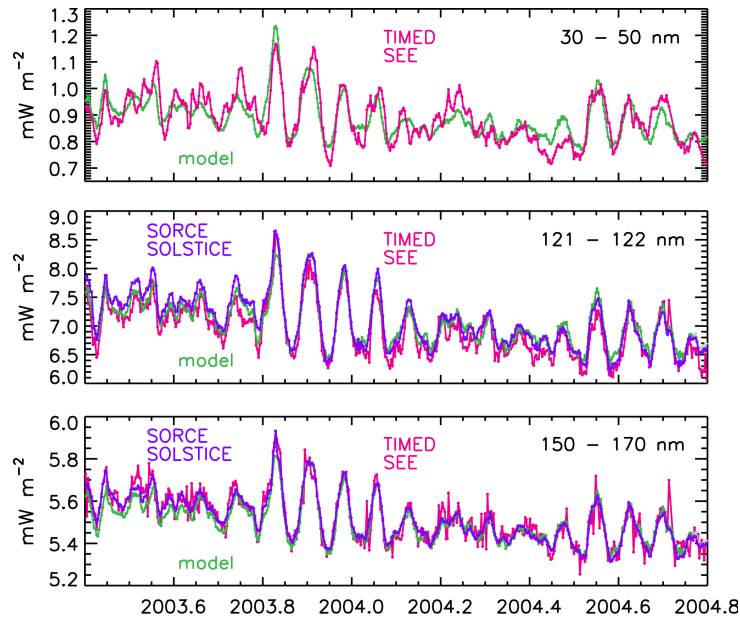


Fig. 10.12. Comparison of *SORCE/SOLSTICE* and *TIMED/SEE* observations and empirical variability model estimates of irradiance in selected wavelength bands including the extreme ultraviolet (30 to 50 nm), the Lyman α line (121-122 nm), and the far ultraviolet (150-179 nm) wavelength bands. The comparisons indicate the good agreement among the irradiance measurements and models on the short time scales of the 27-day rotational modulation.

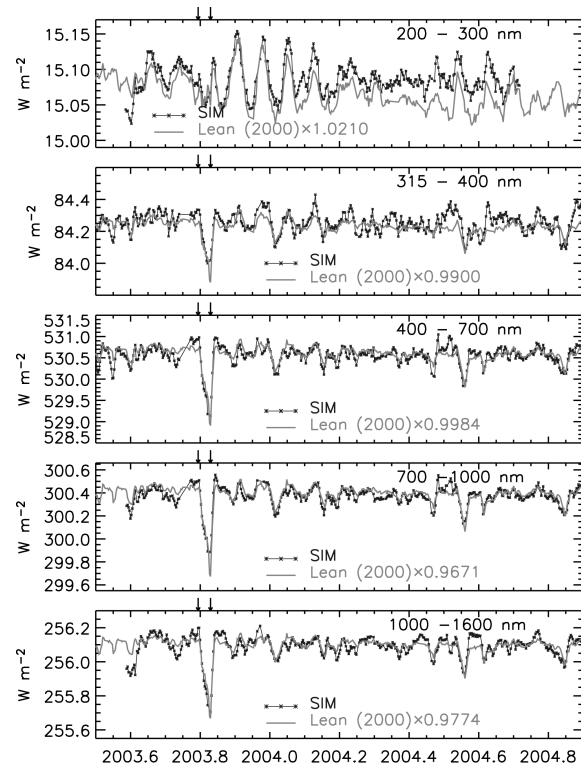


Fig. 10.13. Comparison of SORCE observations (symbols) and empirical variability model values (solid line) of irradiance in selected wavelength bands including the middle ultraviolet (200 to 300 nm), near ultraviolet (315 to 400 nm), visible (400 to 700 nm and 700 to 1000 nm), and near-IR (1000 to 1600 nm) wavelength bands. SORCE observations are made by SIM, except at wavelengths between 200 and 300 nm, which are made by SOLSTICE. The SORCE time series have been detrended by subtracting a 30-day running mean, to remove known instrumental drifts not yet incorporated in the data reduction algorithms. The model time series are scaled by the values shown in each panel to agree with the SIM absolute scale. The arrows indicate the times of the two images in Fig. 10.7.

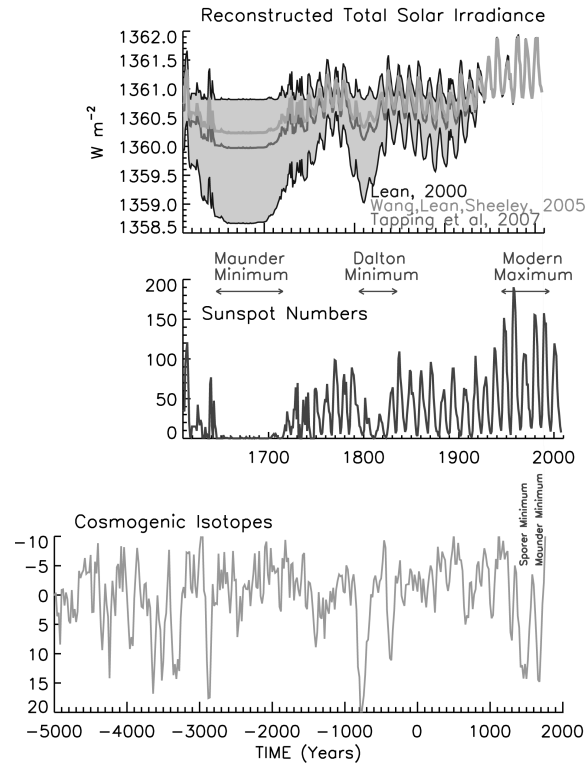


Fig. 10.14. *Top*: Comparison of estimates of total solar irradiance since the Maunder minimum, reconstructed with different assumptions about the strength of the background component that underlies the activity cycle. The upper boundary of the grey shaded region indicates the solar irradiance reconstructed subject to the assumption that the 11-year activity cycle is the only source of variability. The lower boundary of the grey shaded region indicates the solar irradiance reconstructed (by Lean, 2000) subject to the assumption that there is an additional long-term component whose magnitude is derived from the chromospheric Ca II K variations that Baliunas and Jastrow (1990) reported for Sun-like stars. *Middle*: The annual sunspot numbers (Figure 10.4) are shown for comparison, indicating epochs of anomalously low activity during the Maunder and Dalton minima. *Bottom*: Episodes of low activity are seen to punctuate the 7,000 year record of the ^{14}C cosmogenic isotopes (a proxy for long-term solar activity archived in tree rings), shown (on an inverted scale) in the bottom panel.

11

**Astrophysical influences on planetary
climate systems**

Jürg Beer

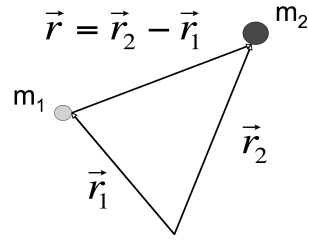


Fig. 11.1. Movement of two bodies m_1 and m_2 under their mutual gravitational interaction.

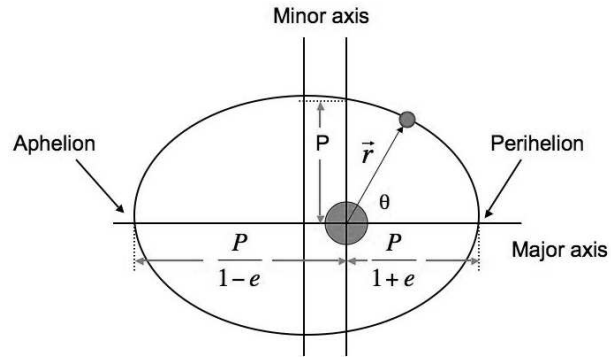


Fig. 11.2. Elliptical orbit of a planet around the Sun which is located in one of the two focal points. The form of the ellipse is determined by the eccentricity e .

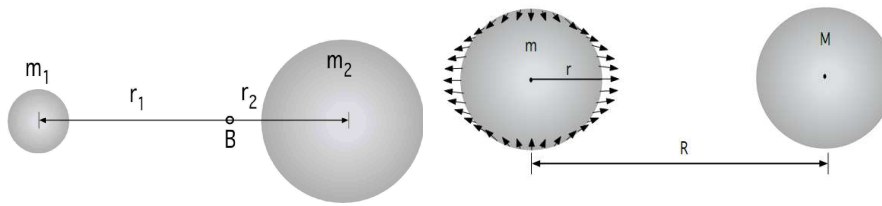


Fig. 11.3. *Left:* Two bodies orbiting around the barycenter B . *Right:* Tidal acceleration induced by the body with mass M on the body with mass m with the distance R between their centers.

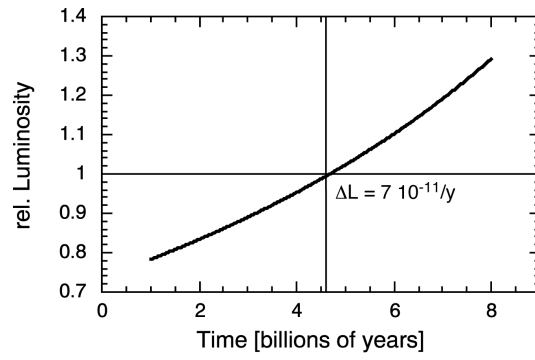


Fig. 11.4. Luminosity of the Sun according to the standard solar model in units relative to the present (Newkirk, 1983).

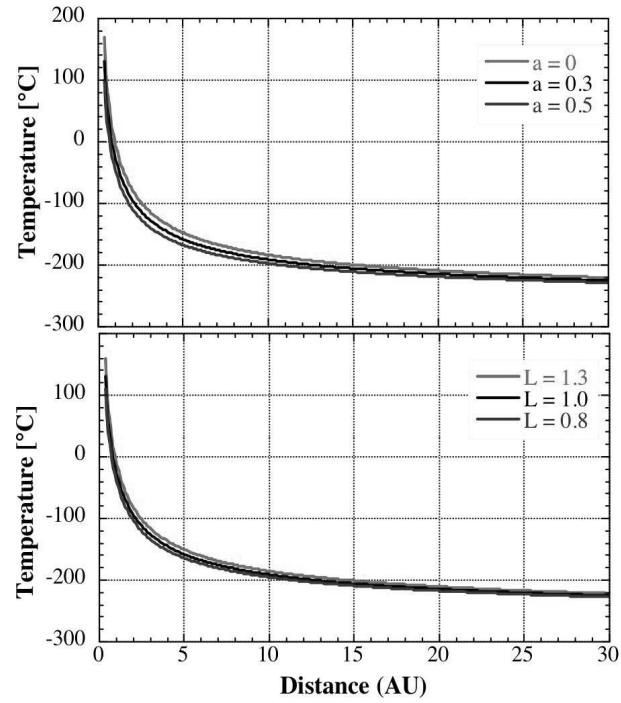


Fig. 11.5. Dependence of planetary temperatures in the absence of an atmosphere on the distance from the Sun (in astronomical units) for different values of the albedo a (upper panel) and the stellar luminosity L_* , which is assumed to be radiated isotropically (lower panel).

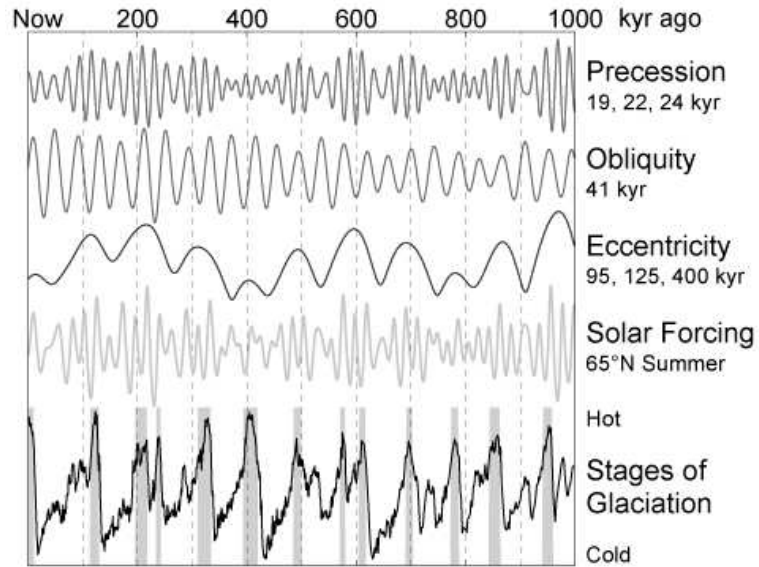


Fig. 11.6. Earth's orbital parameters for the past million years. The first three panels show the three orbital parameters influenced by the other planets (mainly Jupiter and Saturn) and the moon (precession). The fourth panel exhibits the calculated solar forcing at 65°N. The lowermost panel shows sea level changes derived from stable isotope measurements on benthic foraminifera indicating glacial (cold) and interglacial (warm, grey bands) periods

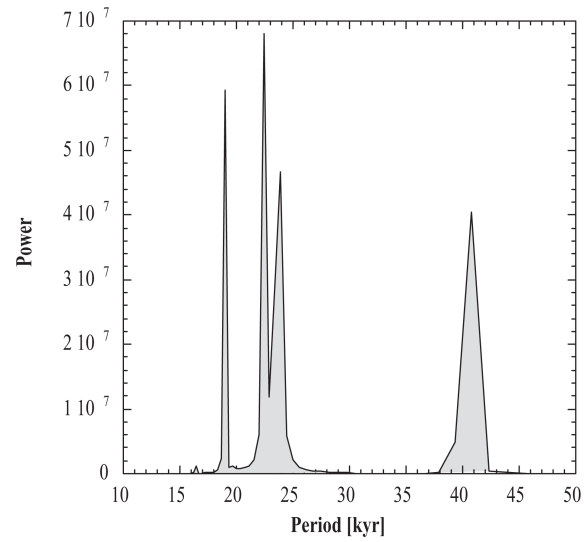


Fig. 11.7. Fourier power spectrum of the calculated summer insolation at 65° N in Fig. 11.6. The precessional periodicities between 19 and 25 kyr and the periodicity of 41 kyr due to the obliquity are clearly visible. The 100-kyr periodicity (eccentricity) is too weak to be seen.

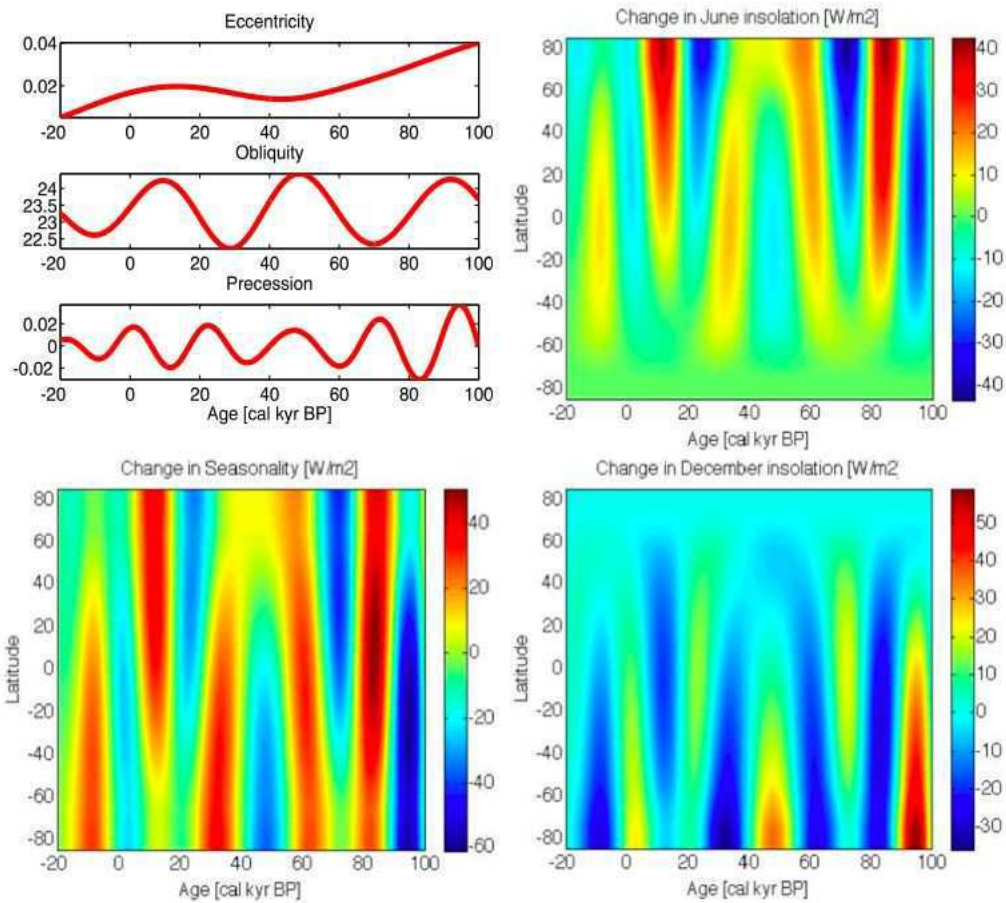


Fig. 11.8. Changes in the orbital parameters of Earth (a) and their effect on the summer (June), the winter (December) and the seasonal (June-December) insolation for the past 100 kyr and the future 20 kyr (-20 kyr BP). Shown are the deviations in W m^{-2} from the mean values. Note the large changes at high latitudes.

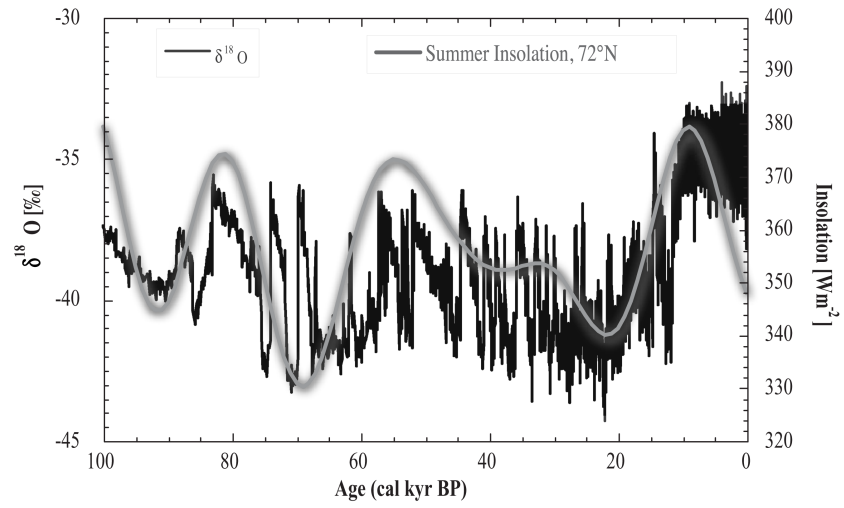


Fig. 11.9. Comparison of the $\delta^{18}\text{O}$ record from the GRIP ice core in central Greenland (72° N) (Dansgaard et al., 1993) with the corresponding summer insolation for the past 100 kyr.

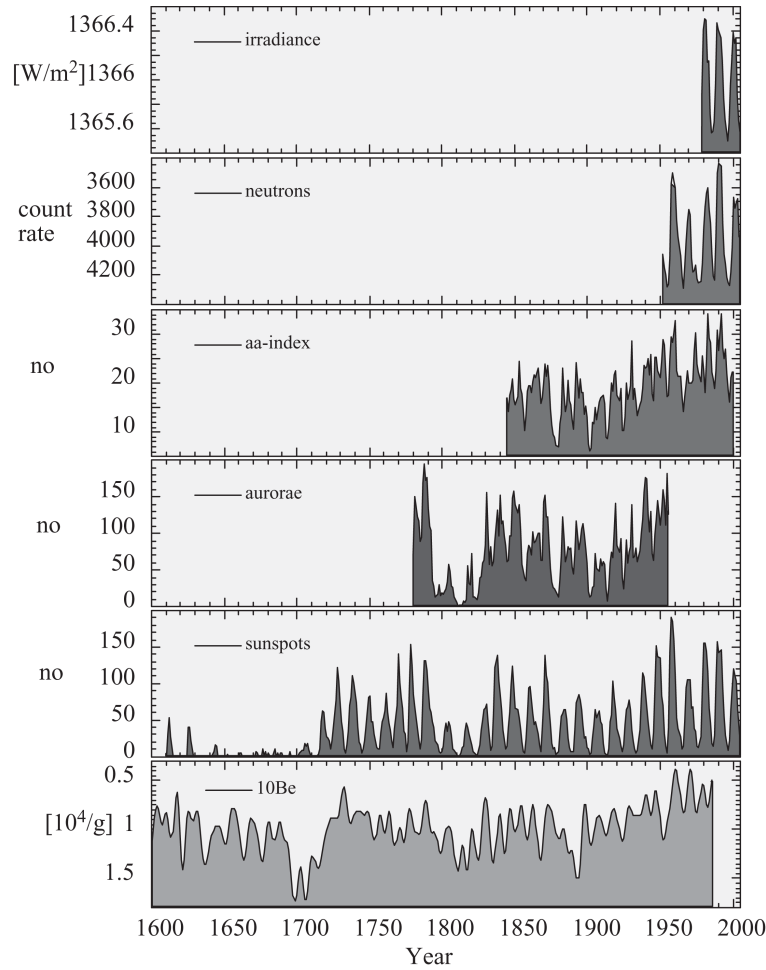


Fig. 11.10. Comparison of proxies of solar activity. Each proxy reflects a specific aspect of solar activity. As a result, all proxies show some common features (11-yr cycle, trends, solar minima), but also differences. The length is limited to the periods of instrumental observations and ranges from 30 (TSI) to about 400 years (sunspots). ^{10}Be is the only record which is not based on direct observations and, therefore has the potential to be extended over at least 10,000 years.

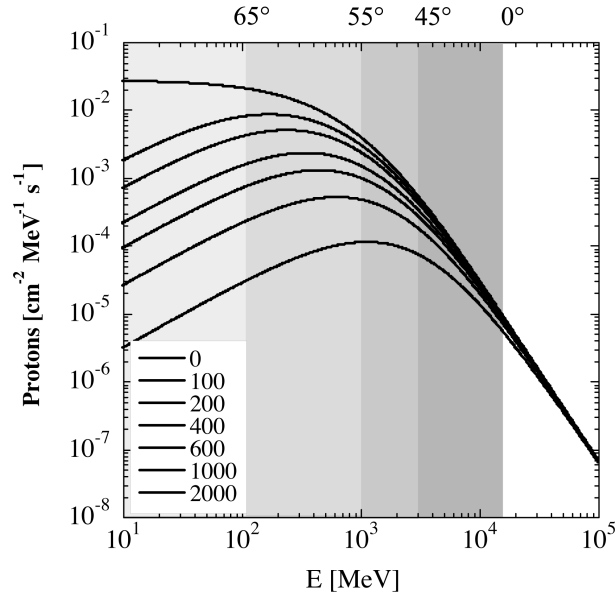


Fig. 11.11. Differential galactic cosmic ray proton fluxes for different levels of solar activity ranging from a value of the solar modulation function $\Phi = 0$ MeV (Eq. 9.8), corresponding to the local interstellar spectrum arriving at Earth without any solar influence, to $\Phi = 2000$ MeV which corresponds to a very active Sun. There are similar curves for cosmic ray alpha particles and heavier nuclides. The vertical bands illustrate the effect of the geomagnetic field which cuts off all protons approaching vertically with an energy below about 100 MeV for a geomagnetic latitude of 65°; below 1 GeV for 55°, and below 3 GeV for 45°. At 0° the cut-off energy is 13.9 GeV for the present geomagnetic field.

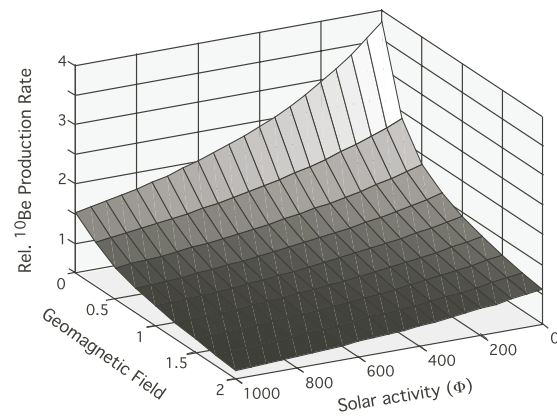


Fig. 11.12. Dependence of the ^{10}Be production rate on the geomagnetic field intensity (in units relative to the today's field) and the solar activity (expressed by the solar modulation function Φ , Eq. 9.8). The production rate is normalised to the present strength of the geomagnetic field and solar activity corresponding to a solar modulation function of 550 MeV (matching the long-term average).

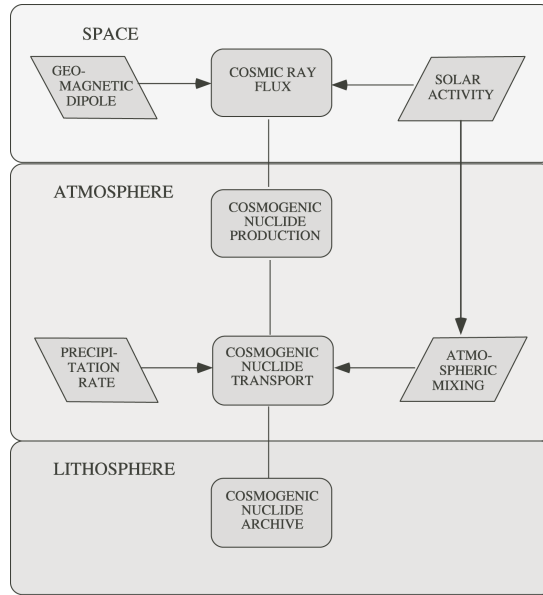


Fig. 11.13. Schematic overview of the production of cosmogenic nuclides and the processes influencing their concentration found in an archive such as a polar ice sheet.

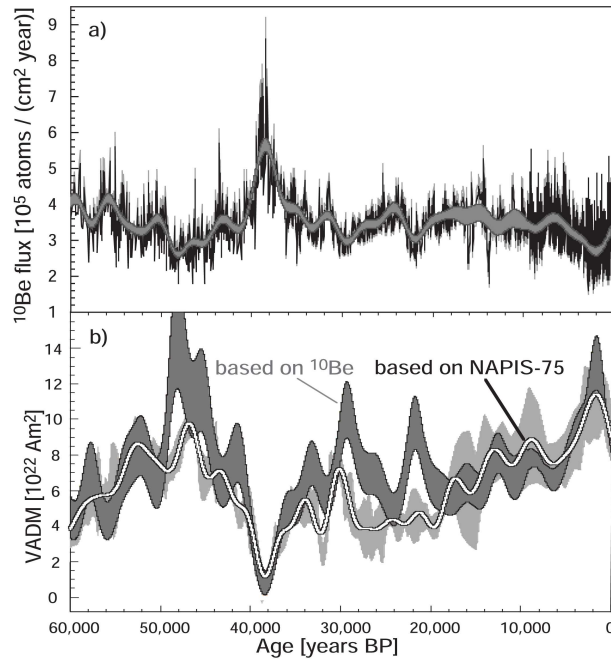


Fig. 11.14. Comparison of (a) ^{10}Be data with (b) the geomagnetic dipole field for the past 60,000 years (modified after Muscheler et al., 2005). Panel (a) shows a compilation of ^{10}Be data from the GRIP and GISP ice cores in Greenland. Panel (b) compares the dipole field derived from ^{10}Be (panel a) to that from remanence data (NAPIS-75) measured in ocean sediment cores (Laj et al., 2000).

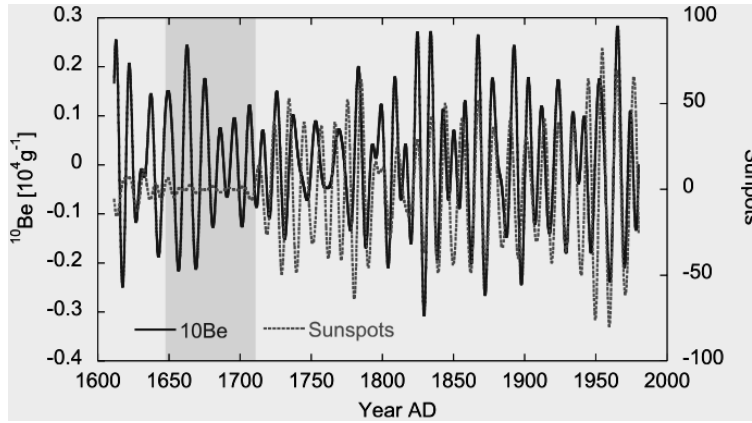


Fig. 11.15. Comparison of the ^{10}Be concentration measured in the Dye 3 ice core from Greenland (Beer et al., 1994) with the sunspot number after applying a band-pass filter (8-16 years). Note that during the Maunder Minimum 1645-1715 (shaded area) when almost no sunspots were observed ^{10}Be shows a clear 11-y Schwabe cycle.

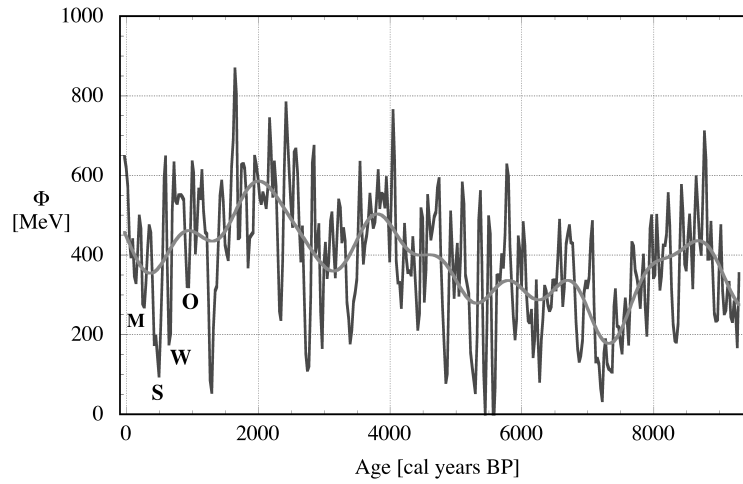


Fig. 11.16. Solar modulation function Φ from the present (0 BP corresponds to 1950) back to 9350 BP (Steinhilber et al., 2008). The black curve shows data that have been low-pass filtered with a cut-off of 150 years; the smooth grey curve with 1000 years. The most recent solar minima are indicated: M: Maunder; S: Spörer; W: Wolf, and O: Oort.

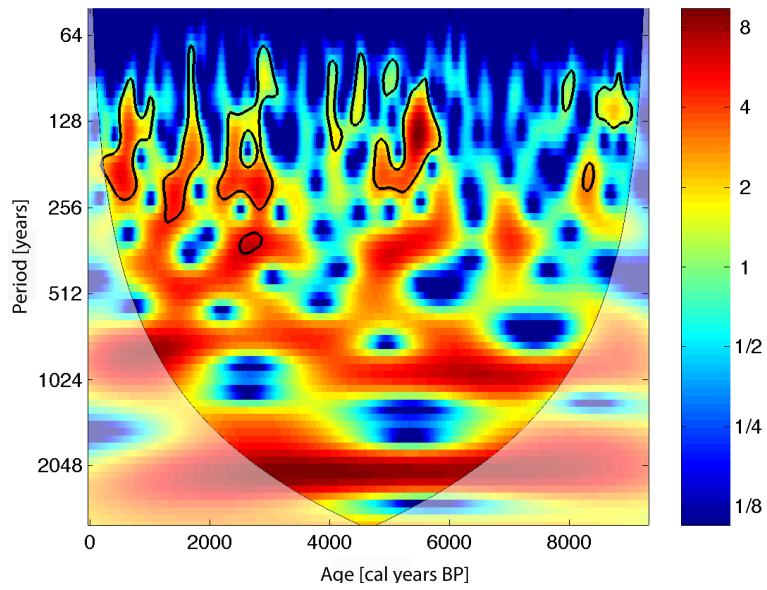


Fig. 11.17. Wavelet analysis (Grinsted, 2002-2004) of the solar modulation function Φ from Fig. 11.16. The color scale is a measure of the spectral power relative to the spectral power of white noise, thus measuring signal significance.

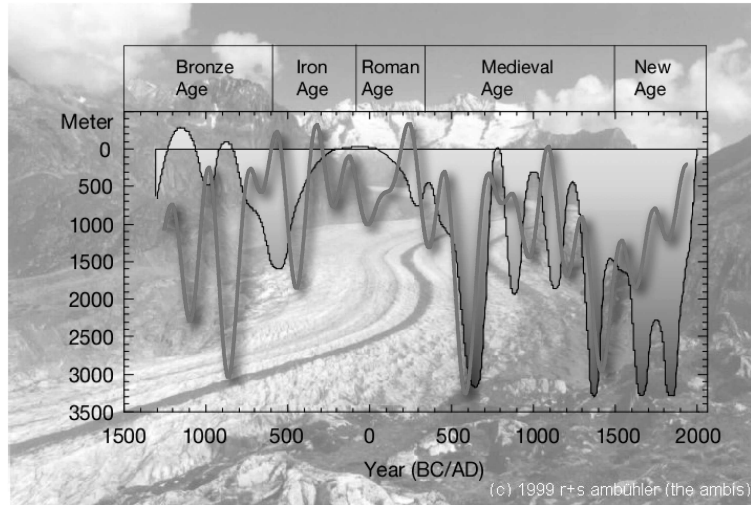


Fig. 11.18. Comparison of the reconstructed length fluctuations of the Great Aletsch glacier (shown in the background) relative to its present length (filled black contour) in the Swiss Alps (from Holzhauser et al., 2005) with the reconstructed total solar irradiance (grey curve with shadow; from Steinhilber et al., 2009a). Lower TSI coincides generally with larger extensions of the glacier. Note that the dating of the record of glacier length fluctuations has some uncertainties. The TSI record is shifted by about 80 years to account for the time lag of the Aletsch glacier.

12

**Assessing the Sun-climate relationship in
paleoclimate records**

Thomas J. Crowley

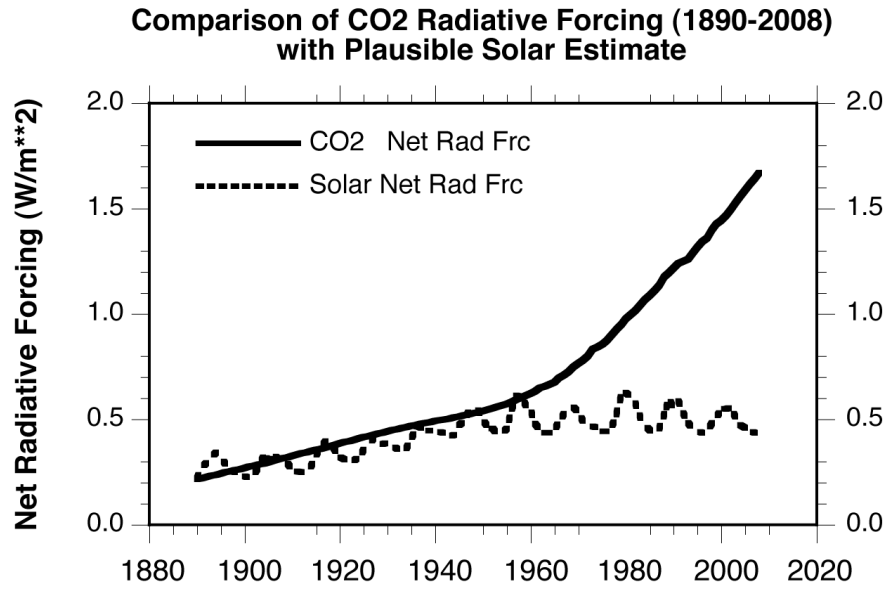


Fig. 12.1. Comparison of well-known radiative forcing (Wm^{-2}) of the anthropogenic carbon dioxide increase (solid) to possible lower-frequency changes in solar irradiance (dotted).

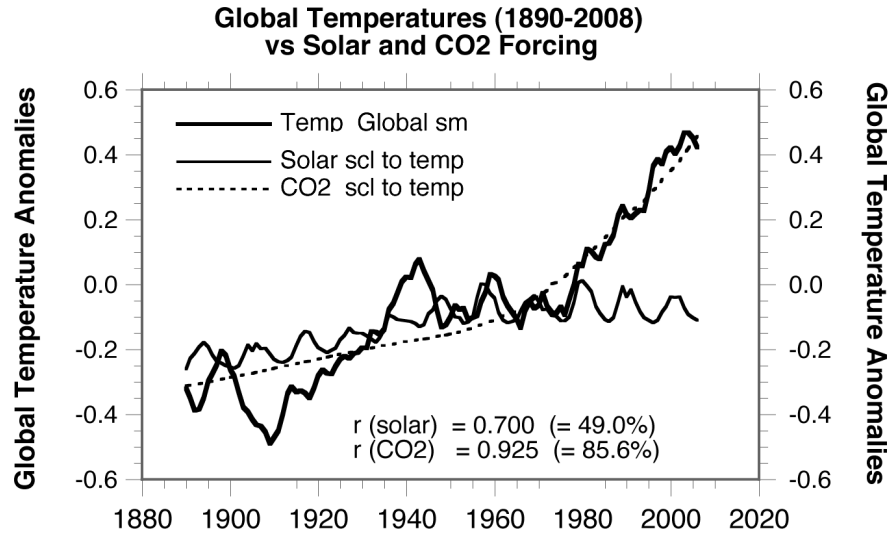


Fig. 12.2. Comparison of plausible temperature changes from radiative forcing of solar variability (thin solid) and carbon dioxide (dashed) against the 5-y smoothed global temperature record (thick solid). The panel shows the correlation coefficients (and, between parentheses, the percentage of the covariance) of temperature records and solar variability ($r(\text{solar})$) and for CO₂ concentration ($r(\text{CO}_2)$).

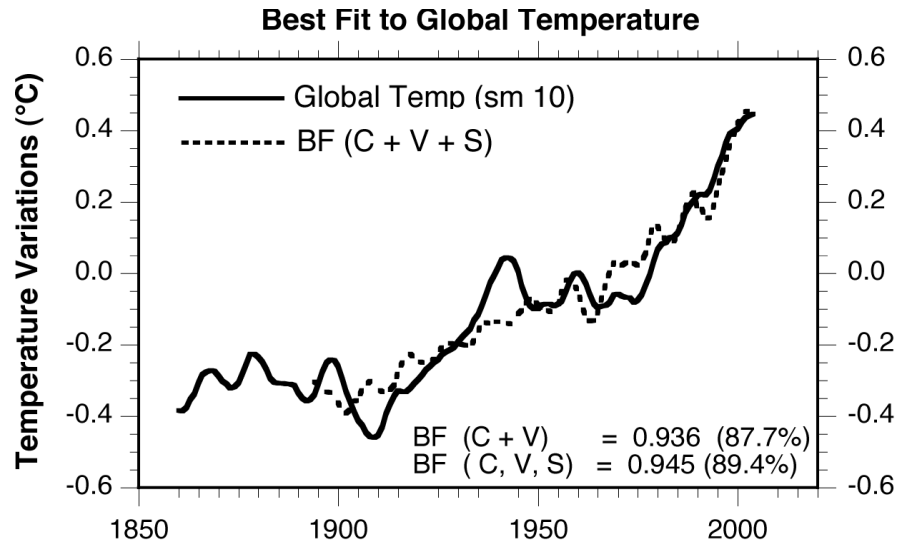


Fig. 12.3. Best-fit (BF) model (dotted) compared with the observed global temperature (solid) for three contributions: C for CO₂, V for volcanism, and S for solar. The correlation coefficients and relative covariances are given for a best fit with CO₂ and volcanism only and for a best fit including all three effects (the difference between the two compilations are so small that only the total forcing is included in the figure).

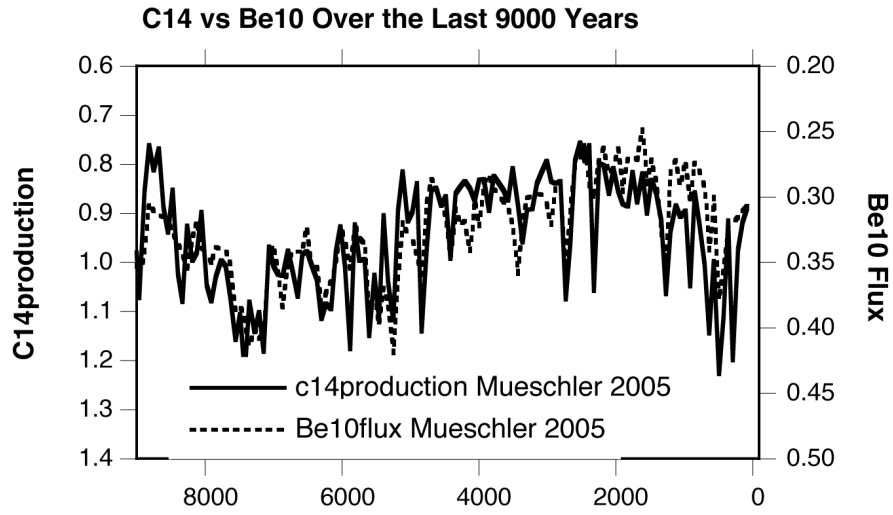


Fig. 12.4. Comparison of two independent estimates of solar variability deduced from relative changes in ^{14}C to ^{12}C ratios and from ^{10}Be concentrations (in units of 10^6 atoms/cm 2 /yr).

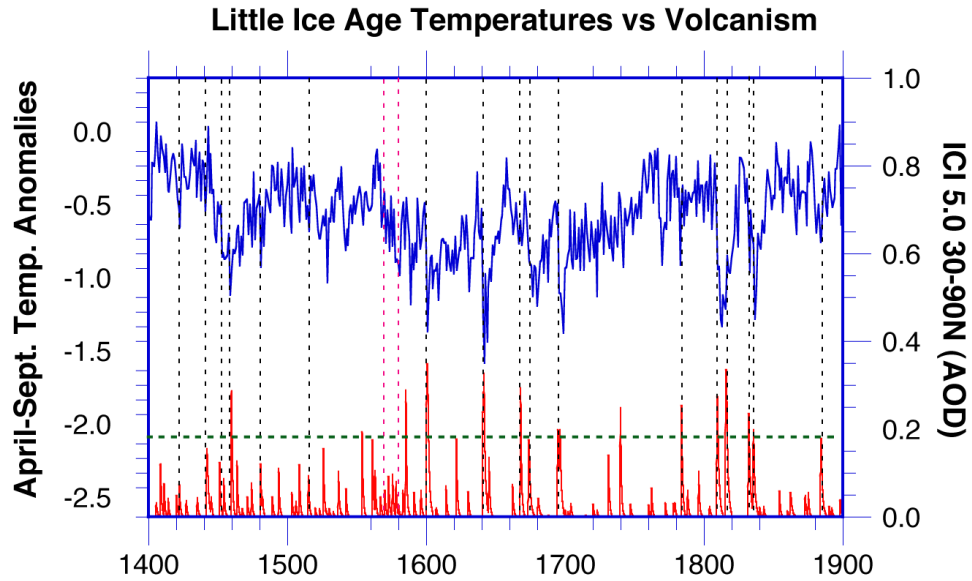


Fig. 12.5. Comparison of treering-based reconstruction of northern hemisphere (land) summer half-year temperatures (upper curve, lefthand axis) with an index of volcanism (lower curve, righthand axis) for $30^{\circ} - 90^{\circ}$ N (AOD denotes aerosol optical depth). Seventeen volcanic eruptions coincident with cooling events registered by tree rings are marked by dashed black lines. A cluster of small eruptions in the late 1500's is contained between the two magenta dashed lines. The AOD of the great 1883 CE Krakatau eruption is highlighted by a horizontal green dashed line.

Three Records of 30-90N (land) Climate Change

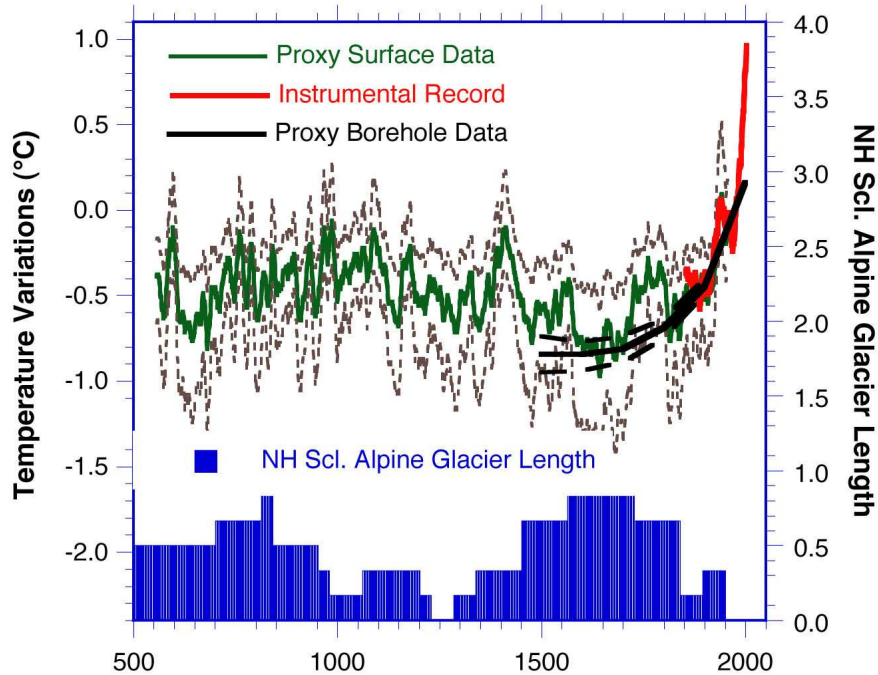


Fig. 12.6. Example of temperature variations over the last 1500 years. The figure illustrates a comparison with scaled northern-hemisphere alpine-glacier extent (see Sec. 12.4) of two estimates of completely different data types for mean annual temperature changes over land for $30^{\circ} - 90^{\circ}\text{N}$. The estimate of surface proxy data (tree rings, ice cores, etc.) is from Hegerl et al. (2007). The "borehole estimate" is based on geothermal measurements of heat flux in boreholes, in which a deconvolution method has been used to remove the heat flux gradient in the Earth's interior in order to determine an estimate of the downward diffusion of century-scale land surface temperature changes over time (cf., Pollack and Smerdon, 2004). To my knowledge, the approach in the Hegerl et al. (2007) paper is the only time these two techniques have been quantitatively compared over the same time and space domains (where most of the data are located). Figure adapted from results in Hegerl et al. (2007), with the unsmoothed instrumental record updated through 2008, and shown up to 2003 after a 10-y smoothing filter was applied.

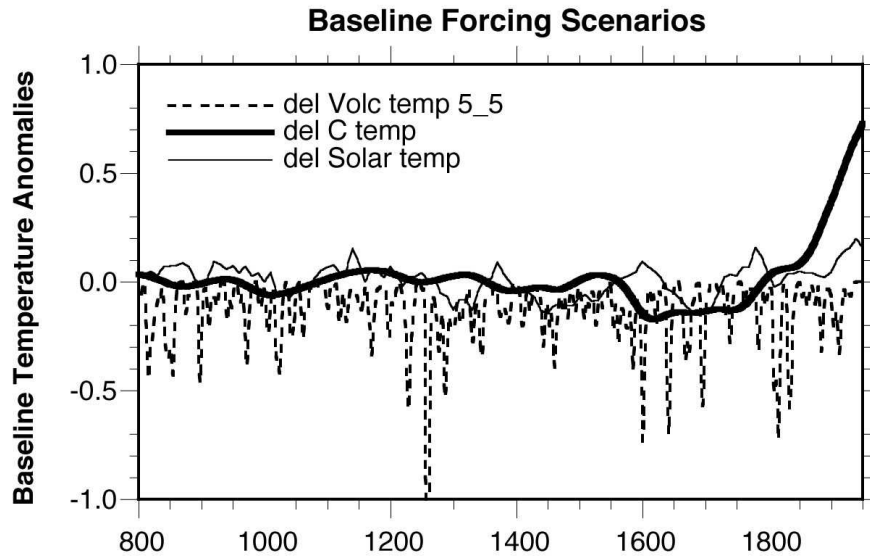


Fig. 12.7. Plausible temperature variations for three different kinds of forcing (C: CO₂; V: volcanism; S: solar) that were used as a baseline for best fit comparisons to tree-ring reconstruction.

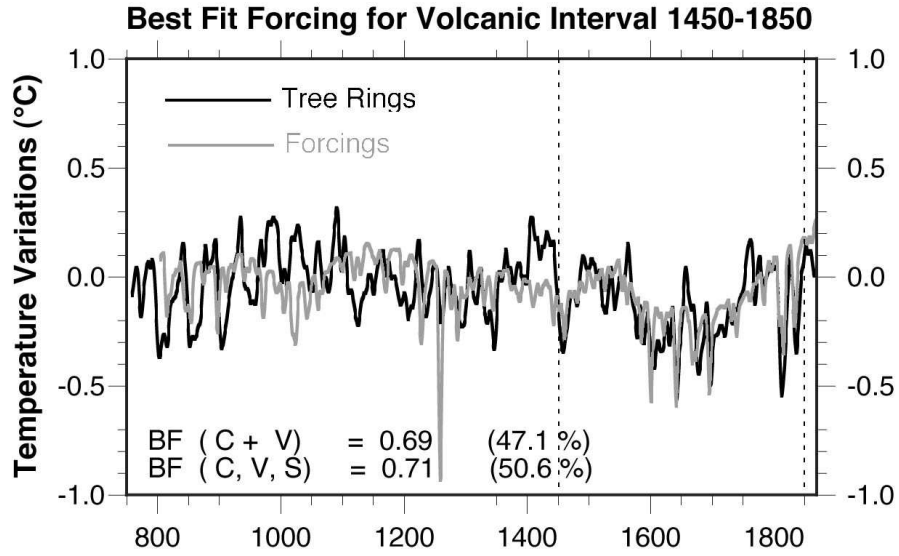


Fig. 12.8. Comparison of best-fit forcing run (grey) over the interval 1450 – 1850 CE (boundaries of vertical dashed lines) with paleoclimate observations (black) for both the calibration interval and the remaining part of the reconstructed records (back to 800 CE). The correlation coefficients and percentage of total variance are shown for two- and three-component fits (the two curves are almost distinguishable, thus only one is plotted).

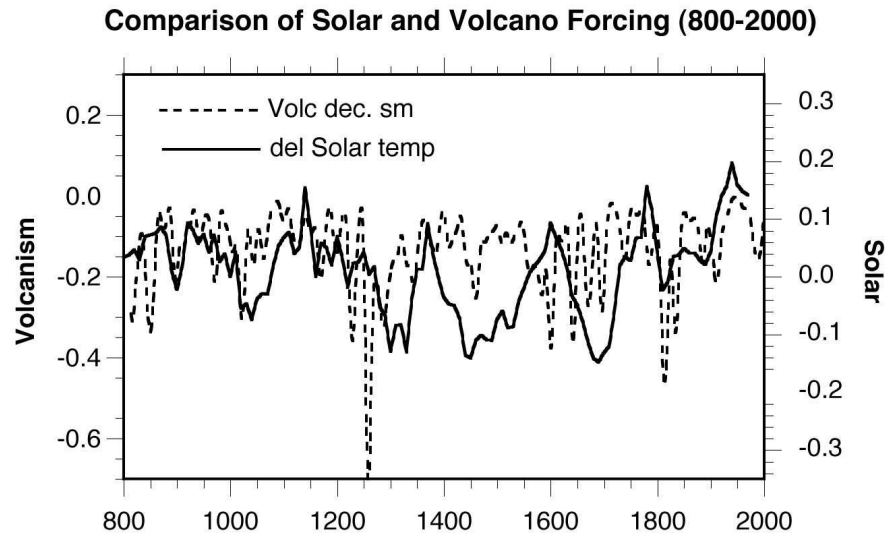


Fig. 12.9. Comparison of solar forcing and smoothed volcanic forcing indicating that there is covariation over a number of time intervals, which can lead to erroneous interpretations of causality.

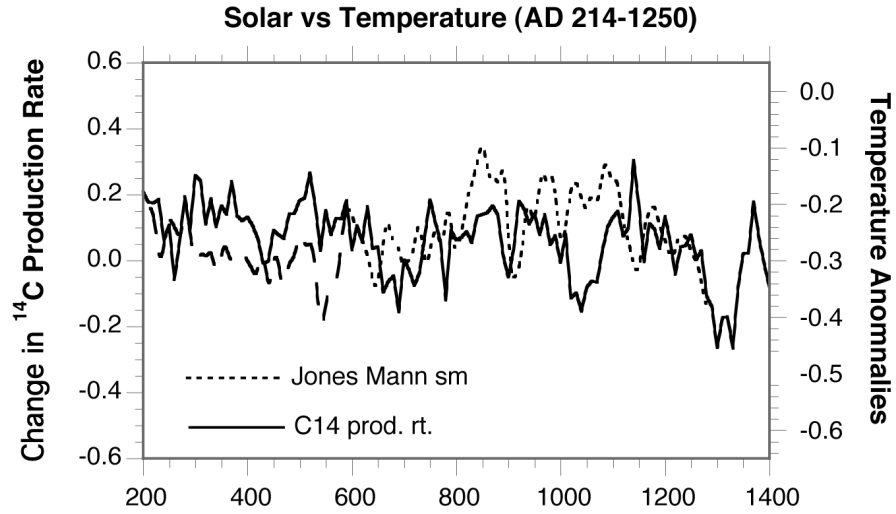


Fig. 12.10. Comparison of solar forcing (solid line; left axis) with a climate reconstruction (dotted and dashed line; right axis) for the interval prior to the time of intense "Little Ice Age" volcanism (214 – 1250 CE). The dashed-dotted line highlights the first section of the Jones-Mann reconstruction to determine whether there were any differences-of-fit for different intervals (there were not - see Table 12.1).

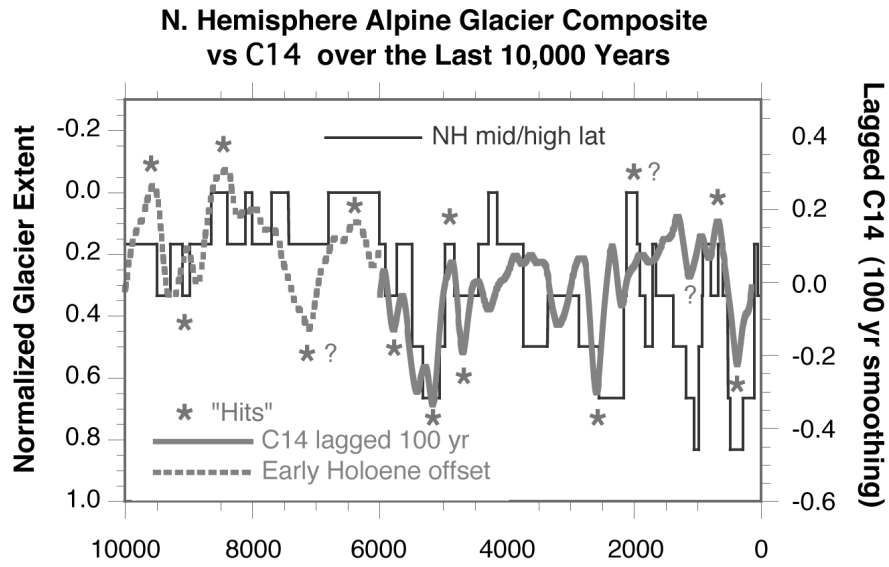


Fig. 12.11. Comparison of ^{14}C estimate of solar variability (solid and dashed curve) with composite record of alpine glaciation (histogram).

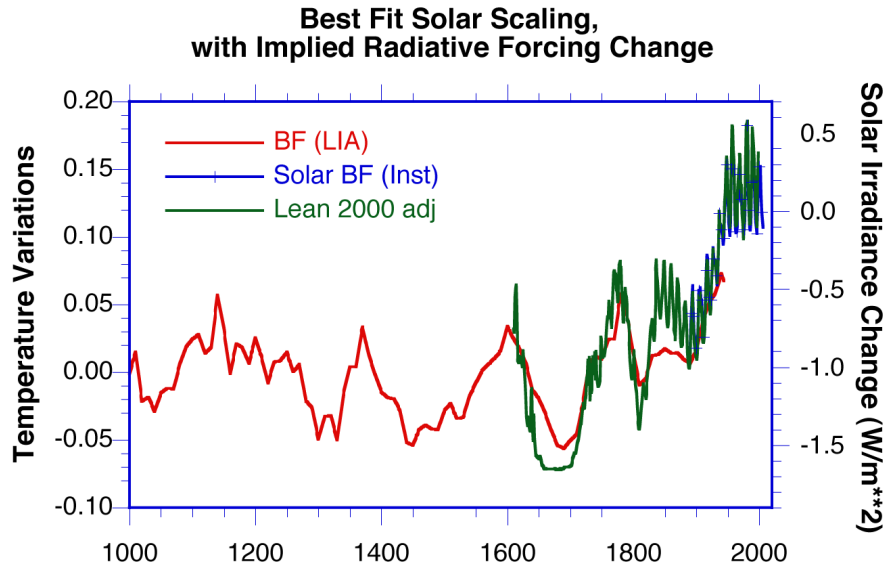


Fig. 12.12. Comparison of independent estimates of solar component for the instrumental interval and Little Ice Age. The righthand scale indicates the estimated change in total solar irradiance for the background component of the re-scaled Lean (2000) record. See Sect. 12.5 for a discussion of the method.

13

Ionospheres of the terrestrial planets

Stanley C. Solomon

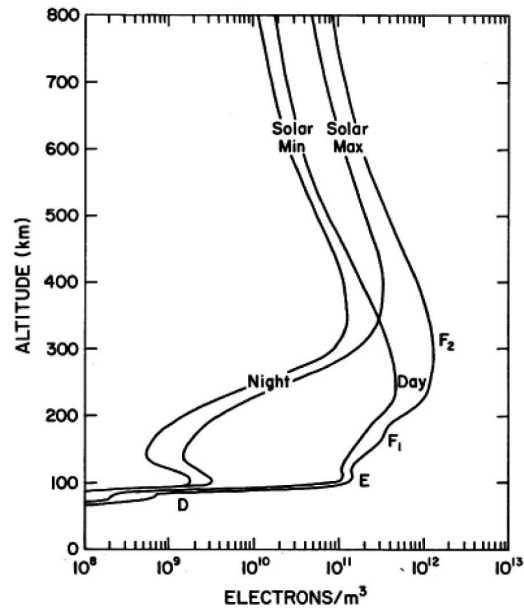


Fig. 13.1. Overview of the altitude distribution of Earth's ionosphere for daytime and nighttime conditions, at high and low solar activity.

Ionospheres of the terrestrial planets

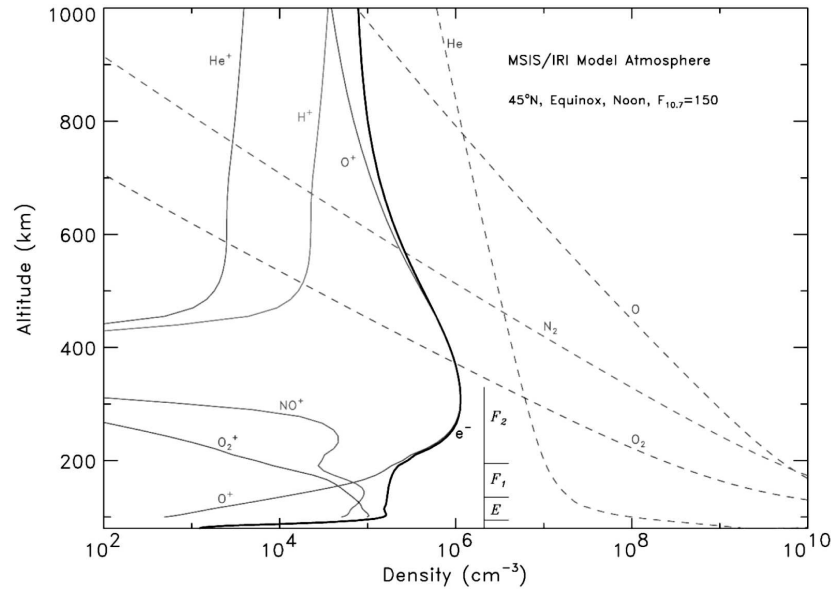


Fig. 13.2. Semi-empirical models of the Earth's thermosphere/ionosphere: the Mass Spectrometer Incoherent Scatter (MSIS) model (Hedin, 1987) and International Reference Ionosphere (IRI; Belitza, 1990).

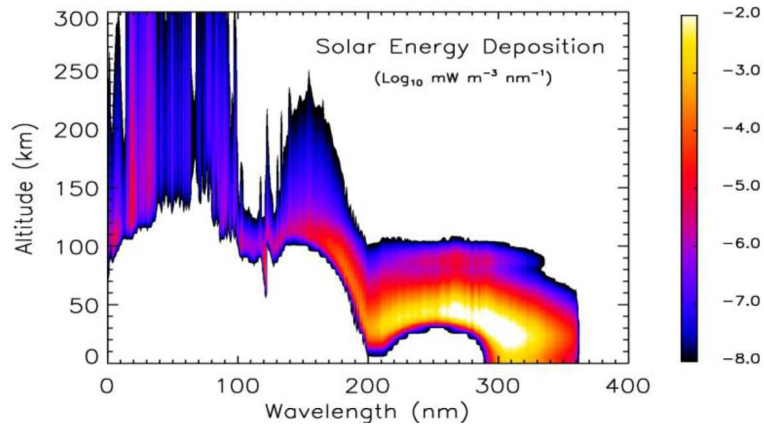


Fig. 13.3. Altitude of penetration of the solar radiation as a function of wavelength. The color range shows the amount of energy deposited in the different layers of the atmosphere for the different parts of the solar spectrum (on a logarithmic scale, in units of $\text{mW}/\text{m}^3/\text{nm}$).

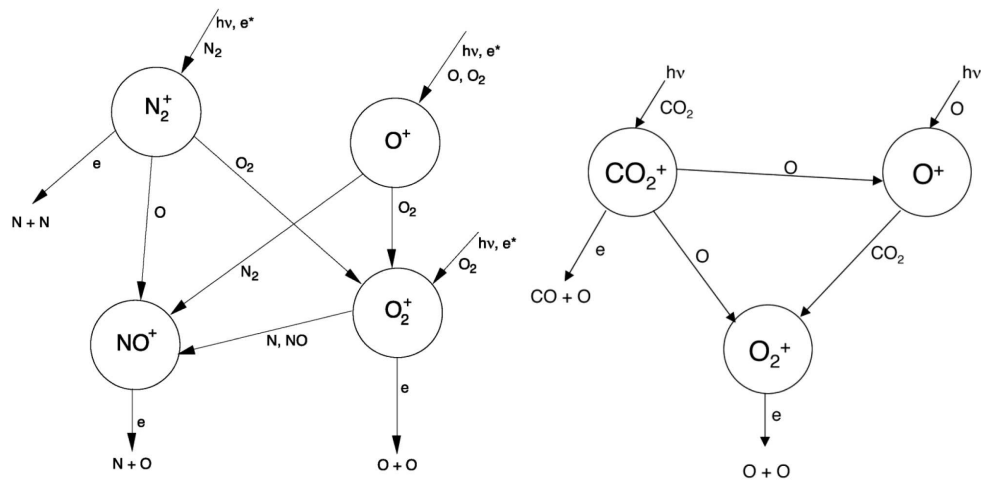


Fig. 13.4. Simplified diagram of ionospheric chemistry in the upper atmosphere of Earth (*left*) and of Venus and Mars (*right*). The vertical direction in these diagrams implies approximate ionization potential.

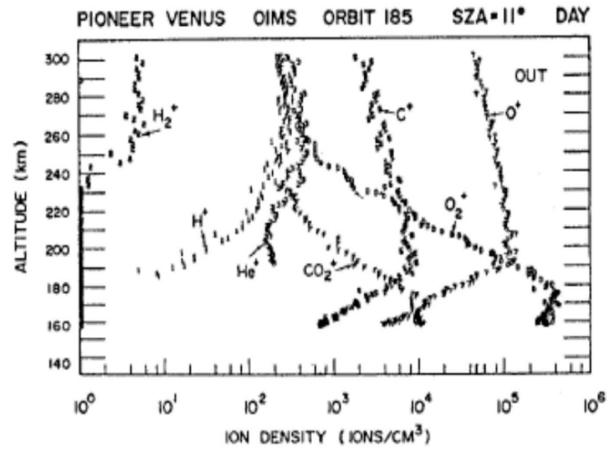


Fig. 13.5. Measurements of the ionosphere of Venus from the ion mass spectrometer on the Pioneer Venus spacecraft.

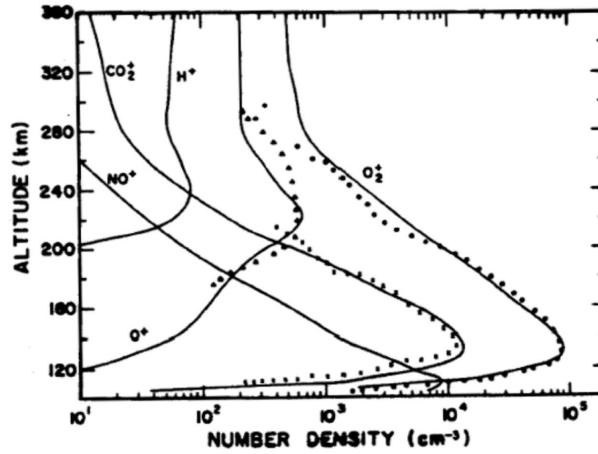


Fig. 13.6. Measurements of the ionosphere of Mars from the ion mass spectrometer on the Viking-1 spacecraft (symbols), and a model ionosphere calculation (lines) for comparison.

Ionospheres of the terrestrial planets

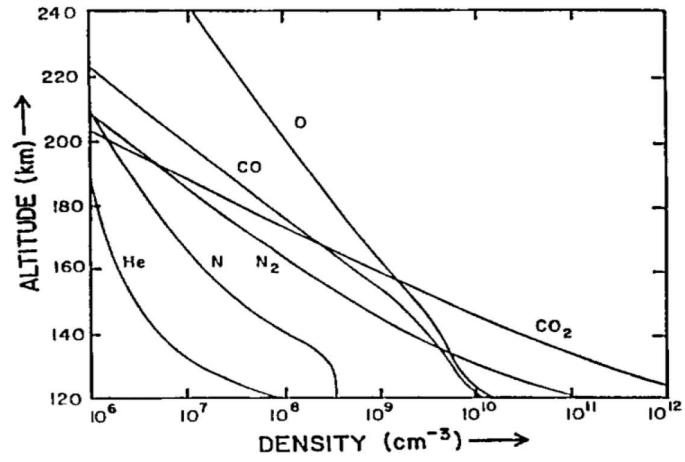


Fig. 13.7. Typical composition of the Venus thermosphere.

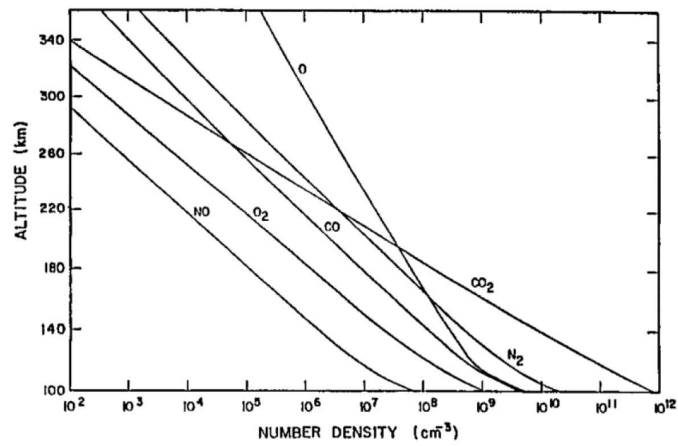


Fig. 13.8. Typical composition of the Mars thermosphere.

14

**Long-term evolution of the geospace
climate**

Jan J. Sojka

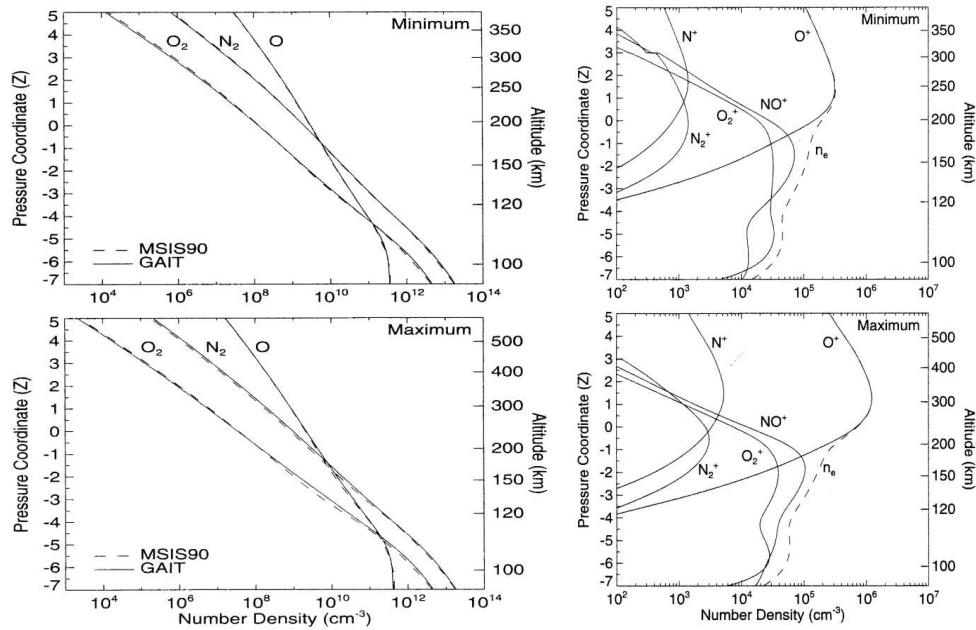


Fig. 14.1. *Left*: Global mean number density profiles under the same conditions for the three major neutral species (N_2 , O_2 , and O) calculated using the GAIT model (solid lines) and MSIS-90 empirical model (dashed lines). *Right*: Global mean number density profiles for five ion species (O^+ , NO^+ , O_2^+ , N^+ , and N_2^+) and the total electron density (n_e) calculated using the GAIT model. Solar minimum (top) and solar maximum (bottom; assuming quiet geomagnetic conditions with $A_p = 4$). The discontinuity observed in the NO^+ and N_2^+ profiles at $Z = 3$ corresponds to where the photo electron calculation stops. (From Smithtro and Sojka, 2005a)

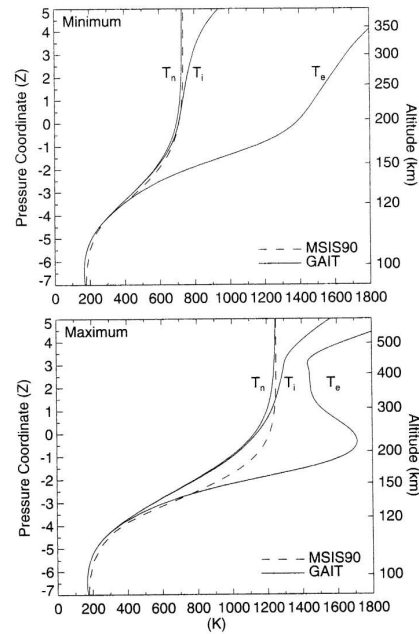


Fig. 14.2. Global mean temperature profiles calculated using the GAIT model (solid lines) and MSIS-90 empirical model (dashed lines). The three profiles correspond to neutral (T_n), ion (T_i), and electron (T_e) gases. Solar minimum (top) and solar maximum (bottom) assuming quiet geomagnetic conditions ($A_p = 4$). (From Smithtro and Sojka 2005a)

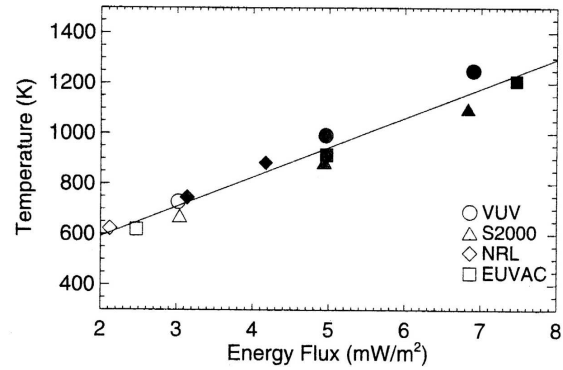


Fig. 14.3. Modeled global mean exospheric temperatures as a function of the EUV energy flux (3-105 nm), calculated using four different irradiance models. The circles, triangles, diamonds, and squares correspond to the UVU [Woods and Rottman, 2002], Solar 2000 version 2.21 [Tobiska et al., 2000], NRLEUV [Warren et al., 2001] and EUVAC [Richards et al., 2994] models respectively. Open symbols represent solar minimum conditions, solid symbols solar maximum conditions, and shaded symbols moderate solar conditions. The solid line indicates a least squares fit to the results. (From Smithtro and Sojka, 2005a)

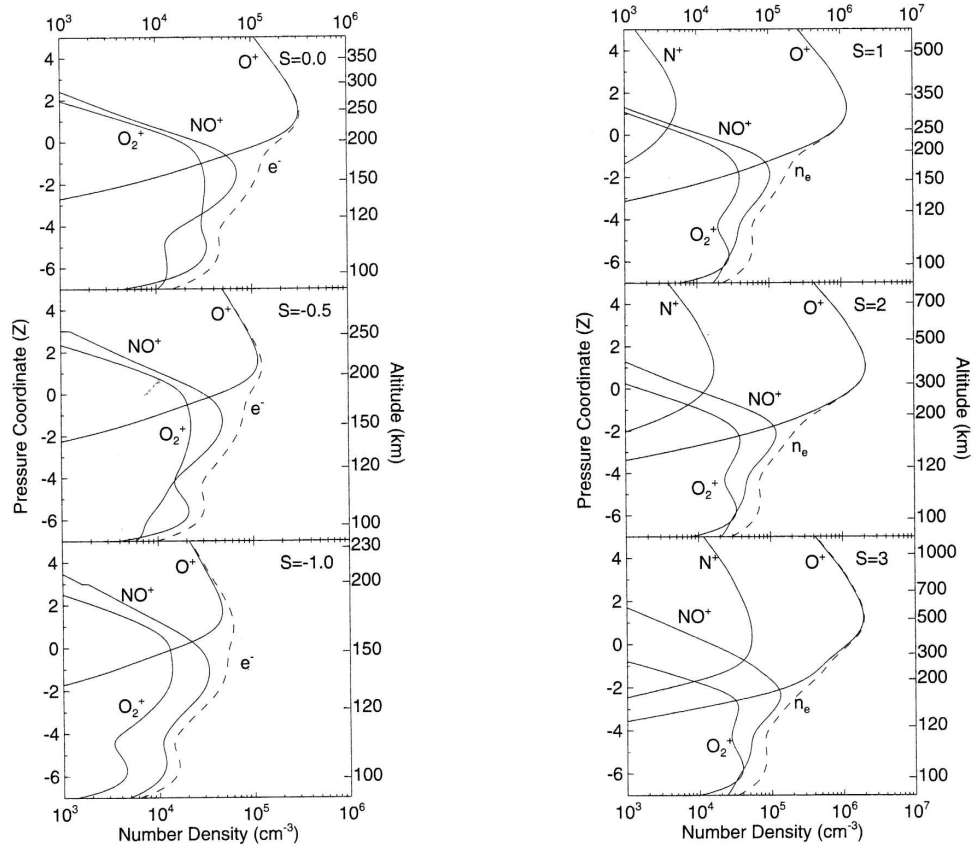


Fig. 14.4. Global mean concentration of the ion and electron (dashed line) gases, calculated using the GAIT model for six different levels of the solar activity increasing from $S_{\text{EUV}} = -1.0$ to $S_{\text{EUV}} = 3$, clockwise from the bottom left. The profiles are plotted as a function of the pressure coordinate, Z , with the corresponding altitudes provided on the right-hand axis. (From Smithtro and Sojka, 2005b)

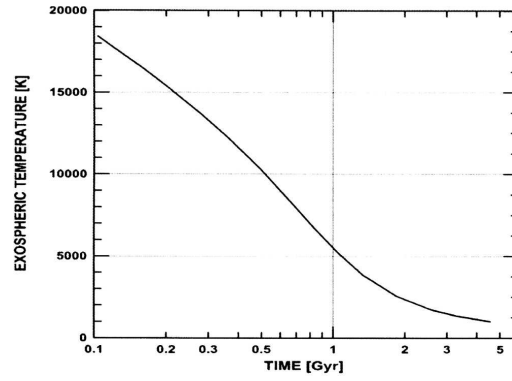


Fig. 14.5. Evolution of the exospheric temperature based on Earth's present atmospheric composition over the planet's history as a function of the solar XUV flux for a strongly limited hydrogen blow-off rate. (From Kulikov et al., 2007.)

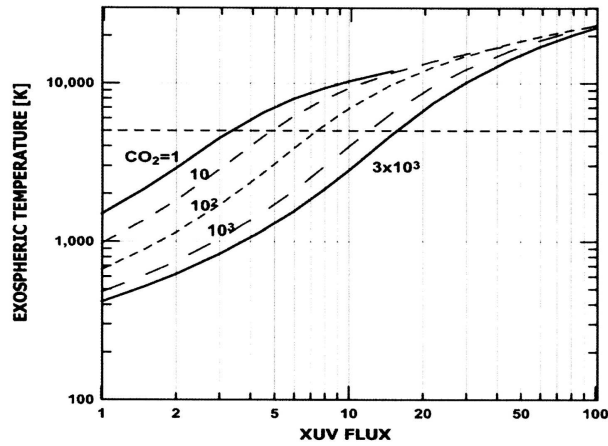


Fig. 14.6. Earth's exospheric temperatures for different levels of CO₂ abundance in units of PAL (Present Atmospheric Level: 1 PAL for CO₂ = 3.3×10^{-4}) in the thermosphere as a function of solar XUV flux. The numbers by the curves correspond to CO₂ volume mixing ratios expressed in PAL. The horizontal dashed line shows the blow-off temperature of atomic hydrogen. (From Kulikov et al., 2007)

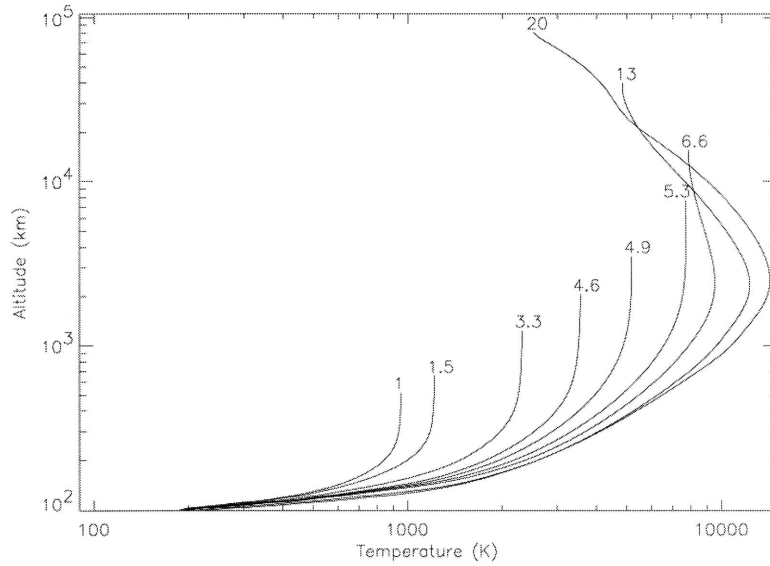


Fig. 14.7. Thermospheric temperature profiles for different solar EUV flux cases (normalized to present-day solar mean energy flux ~ 1 times present EUV which represents solar EUV energy flux $\sim 5.2 \text{ mW/m}^2$). It is shown that when solar EUV energy flux exceeds certain critical value, the upper part of the thermosphere begins to cool as a result of the increasingly significant adiabatic cooling effect. Beyond the critical flux (~ 5 times present EUV in this plot), the higher the energy input into the thermosphere, the lower the exobase temperature. (From Tian et al., 2008a)

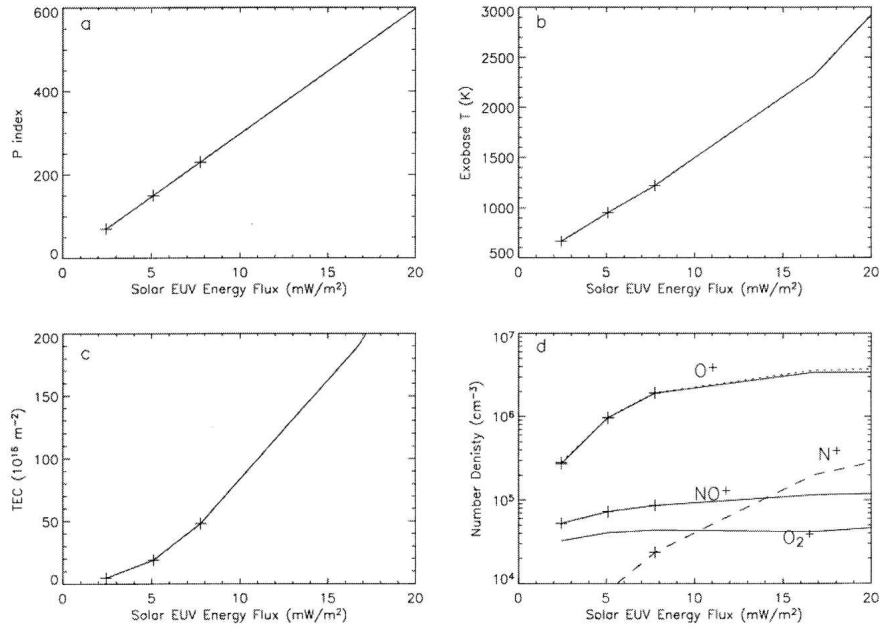


Fig. 14.8. (a) Variations of solar EUV energy flux with P index (an equal weighting of the instantaneous F10.7 and 81-d average F10.7 solar radio flux at 10.7 cm). (b) Variation of exobase temperature with solar EUV flux. (c) Variation of total electron content (TEC) with solar EUV flux. (d) Variation of peak densities of major ion species with solar EUV flux. The dotted curve in panel (d) marks the variation of peak electron densities. In each variation of peak electron densities, the crosses correspond to the solar minimum mean and maximum values. (From Tian et al., 2008a)

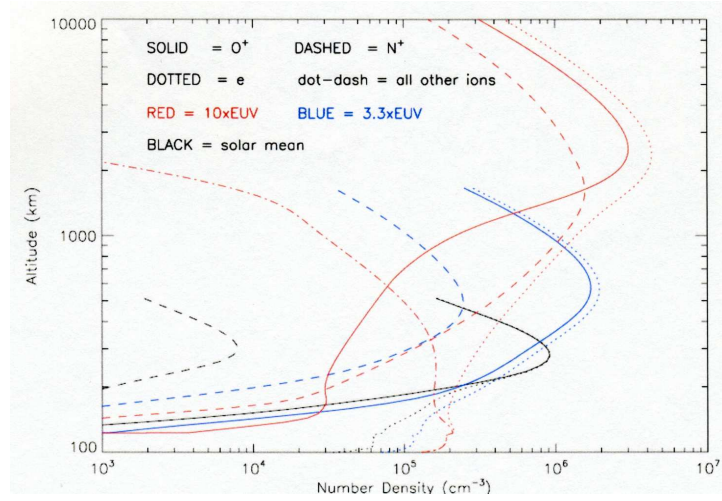


Fig. 14.9. Density profiles of O^+ (solid curves), N^+ (dashed curves), and electrons (dotted curves) under different solar EUV conditions. The total density curves of all ions other than O^+ and N^+ in the $10\times$ present EUV case is presented with the dot-dashed curve. (From Tian et al., 2008b)

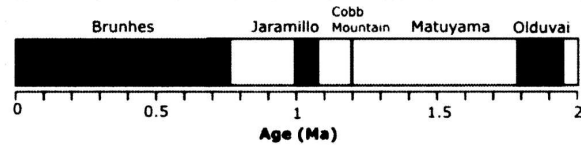


Fig. 14.10. The Earth's virtual axial dipole moment (VADM) orientation over the past 2 million years. The current orientation are the black shaded regions. See Fig. 7.4 for a much longer record. (From Valet et al., 2005)

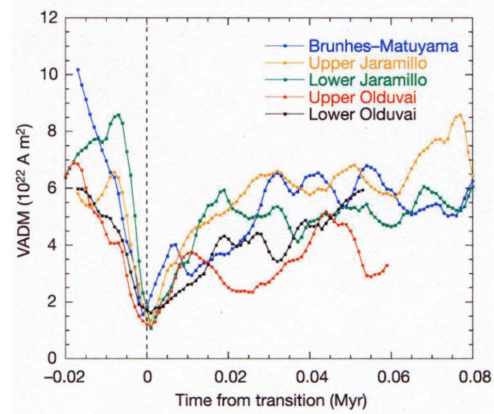


Fig. 14.11. Variations in the virtual axial dipole moment across the five reversals occurring during the past 2 My. These are superimposed about their respective reversal epoch (with time running from right to left). A 60 – 80 ky long decrease precedes each reversal. (From Valet et al., 2005)

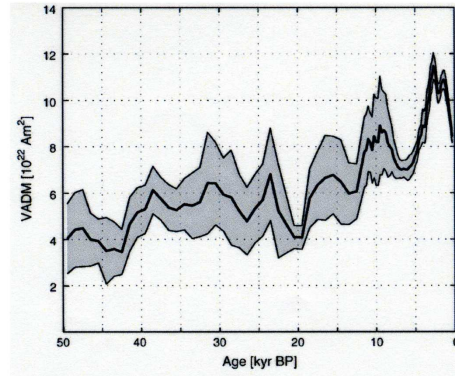


Fig. 14.12. The Earth's virtual axial dipole moment (VADM) for the past 50 ky (black line) and the associated error estimates (2σ) obtained using a bootstrap approach (gray zone). (From Knudsen et al., 2008)

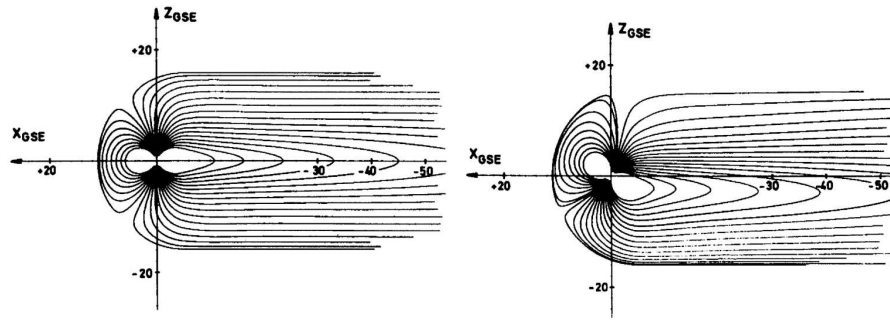


Fig. 14.13. Field lines plotted in the noon-midnight meridian plane for an untitled planetary dipole embedded in the solar wind (left) and the dipole tilted in the noon-midnight meridian at 35° (right). (From Voigt, 1981)

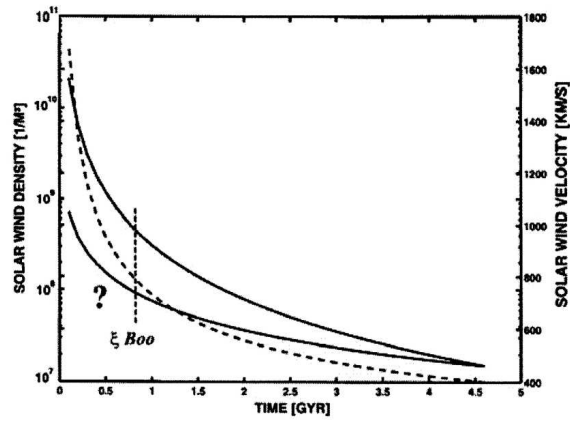


Fig. 14.14. Evolution of the observation-based minimum and maximum stellar wind densities scaled to 1 AU (left scale; solid lines) obtained from several nearby solar-like stars. On the right scale is the solar wind speed for the stellar wind evolution (dashed line). (From Lundin et al., 2007)

Long-term evolution of the geospace climate

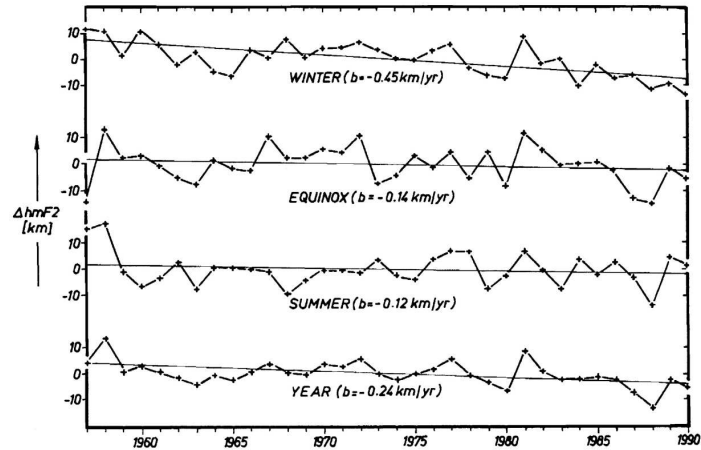


Fig. 14.15. Seasonal and yearly trends of the F_2 layer height ($hmF2$) at Julrusruh after elimination of solar and geomagnetic influences. (From Bremer, 1992)

15

**Waves and transport processes in
atmospheres and oceans**

Richard L. Walterscheid

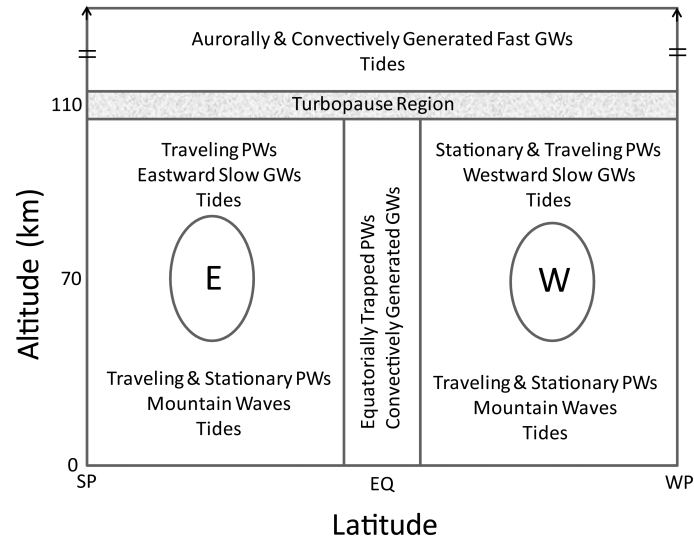


Fig. 15.1. Summary diagram for the dominant wave modes in the Earth's atmosphere as function of altitude and latitude from pole to pole, including gravity waves (GW), stationary and traveling planetary waves (PW) atmospheric tides, and mountain (gravity) waves. The approximate height of the turbopause, below which turbulent mixing dominates, is indicated. Here SP denotes the summer pole and WP the winter pole, E denotes the location of the stratospheric-mesospheric easterly (westward) jet and W denotes the location of the westerly (eastward) jet. The jet maxima are generally found within a few kilometers of 70 km altitude. The mix of waves in various regions indicates the dominant waves. Other waves may be present (for example non-equatorial convectively generated waves below the jets). The directionality associated with slow gravity waves above the jets is caused by the filtering action of the zonal wind system. North-south (meridionally) propagating gravity waves are also present, but the primary source of slow waves is zonal flow over mountains and this generates mostly zonal propagation.

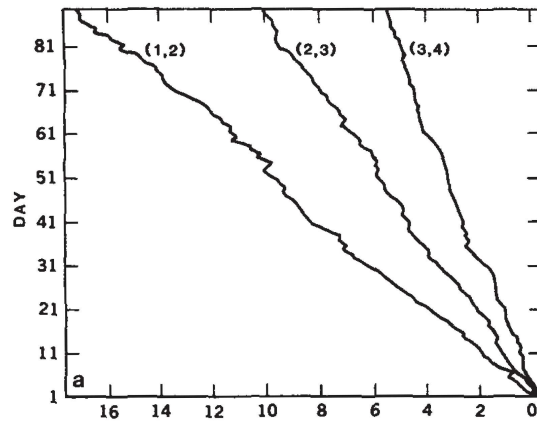


Fig. 15.2. The results of a spherical harmonic analysis of the 24-hour tendency field (i.e., the change over a 24-h period) in the height of the 500 hPa surface (at ~ 5.5 km) in the Earth's atmosphere. The abscissa is the number of passages of a fixed phase of a wave. The ordinate is the number of days since the first passage. The three waves shown have zonal wavenumbers $s = 1, 2$ and 3 (the first index of each index pair). (From Lindzen et al., 1984, redrawn from Eliassen and Machenhauer, 1965)

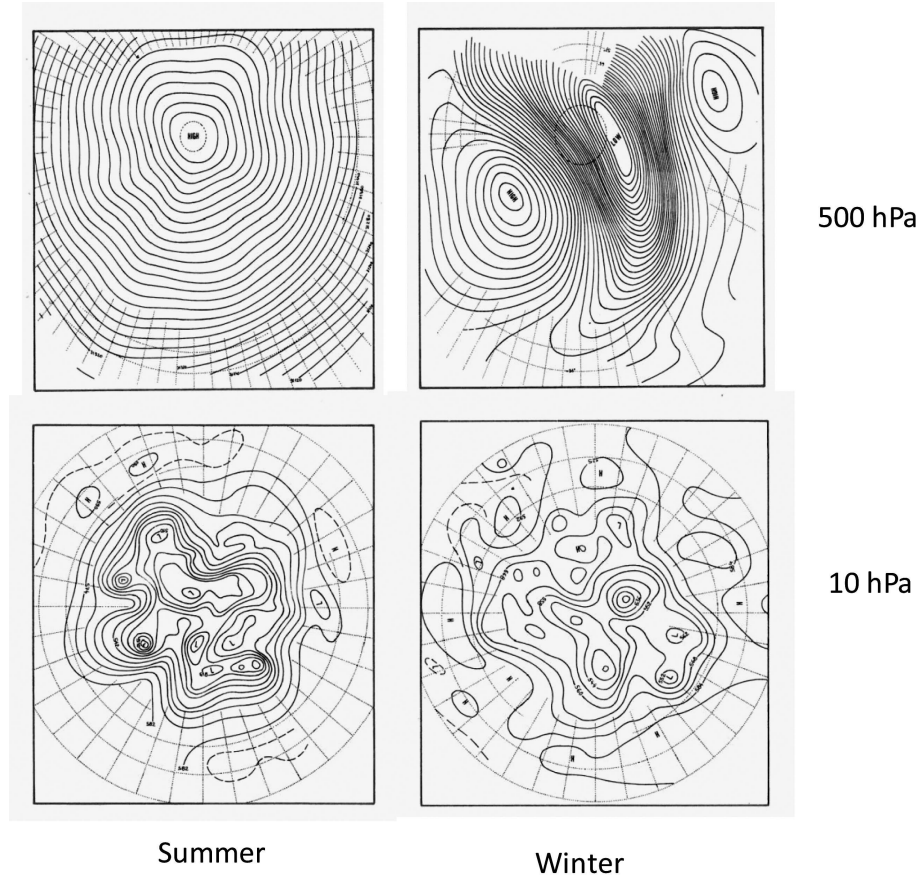


Fig. 15.3. Traveling planetary waves: contour maps of the height of two different pressure levels in the northern hemisphere: in the troposphere at 500 hPa (~5.5 km altitude) and in the stratosphere at 10 hPa (~16 km) for 15 July 1958 (left) and 15 January 1959 (right). From Charney (1973).



Fig. 15.4. A long wave train of gravity waves visualized in clouds over the Indian Ocean. The waves are traveling on an interface between two layers of differing thermal properties. (Image courtesy NASA/GSFC/LaRC/JPL,MISR team)

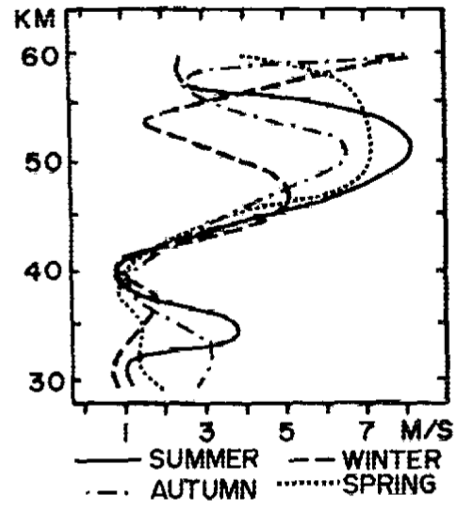


Fig. 15.5. The vertical variation of the amplitude of the diurnal component of the meridional wind at a low latitude location for all four seasons. (From Nastrom and Belmont, 1976)

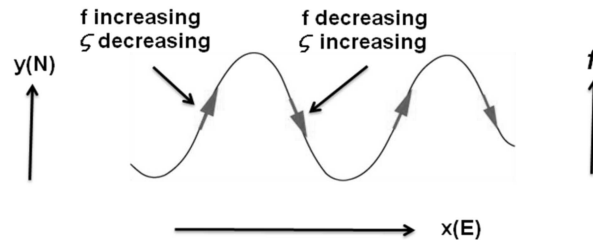


Fig. 15.6. The mechanism of planetary wave motion shown in schematic form based on conservation of absolute vorticity along a parcel's trajectory.

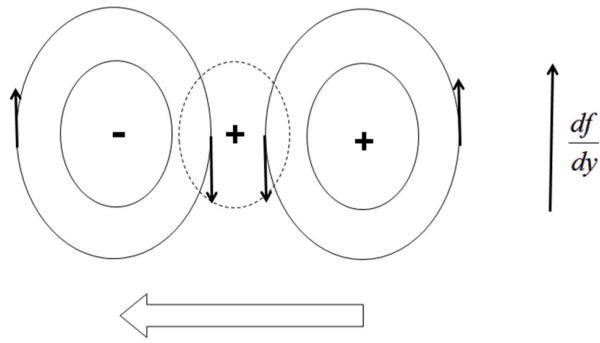


Fig. 15.7. An illustration of Rossby wave propagation. The schematic shows two relative vorticity cells of opposite sign. The contours are stream functions with anticlockwise flow around the positive center and clockwise flow around the negative center (see text for details).

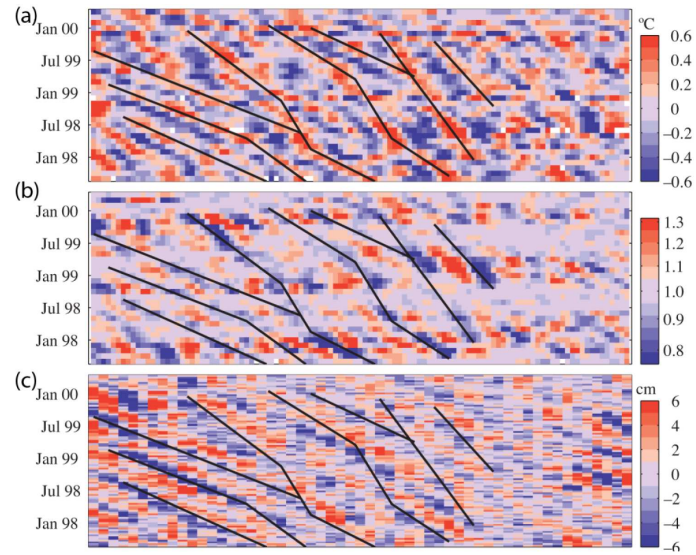


Fig. 15.8. A time-longitude representation of group (energy) propagation for Rossby waves in the ocean (Hovmöller diagram), showing the variation of (a) sea surface temperature anomalies, (b) chlorophyll concentration anomalies, and (c) sea surface height anomalies. The tilt of features in this diagram reflects the westward propagation of wave groups. (From Quartly et al., 2002)

Gravity Waves

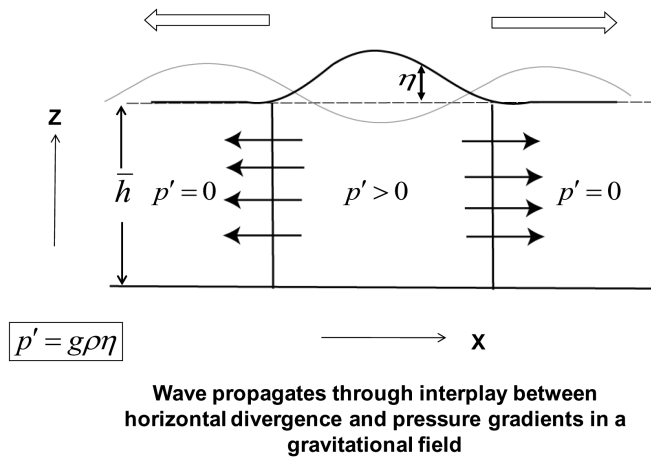


Fig. 15.9. Gravity waves in an incompressible fluid of uniform depth. The fluid has a free surface and an undisturbed average depth of \bar{h} . The fluid is initially deformed with a displacement height of η .

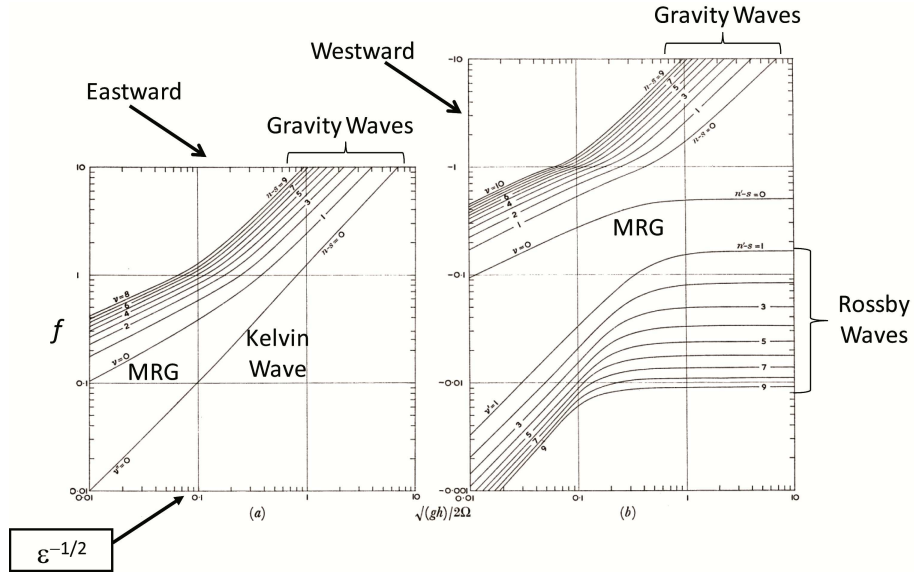


Fig. 15.10. The eigenfrequencies for eigensolutions of Laplace's tidal equation for zonal wave number 1 ($s = 1$). Results are shown for eastward and westward traveling waves. The ordinate is the normalized frequency $f_* = \omega/2\Omega$. The abscissa is the inverse square root of Lamb's parameter ϵ . Mixed Rossby-gravity modes are labeled MRG. Adapted from Figure 2 in Longuet-Higgins (1968).

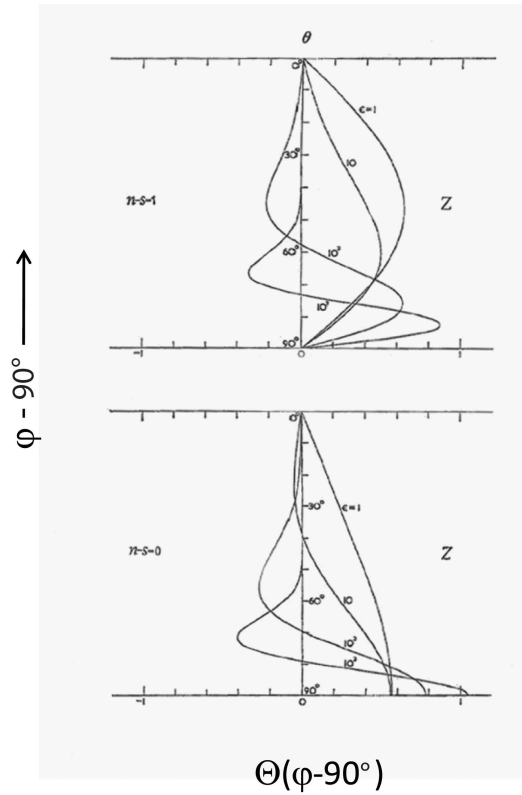


Fig. 15.11. The eigenfunctions (Hough functions) for $s = 1$ for the two lowest westward modes ($n - s = 0, 1$) of Class-1 waves. The curves are for fixed values of Lamb's parameter ϵ . The ordinate is co-latitude ($90^\circ - \text{latitude}$). The abscissa (Z) is a normalized value of the Hough functions. Adapted from Figure 8 of Longuet-Higgins (1968).

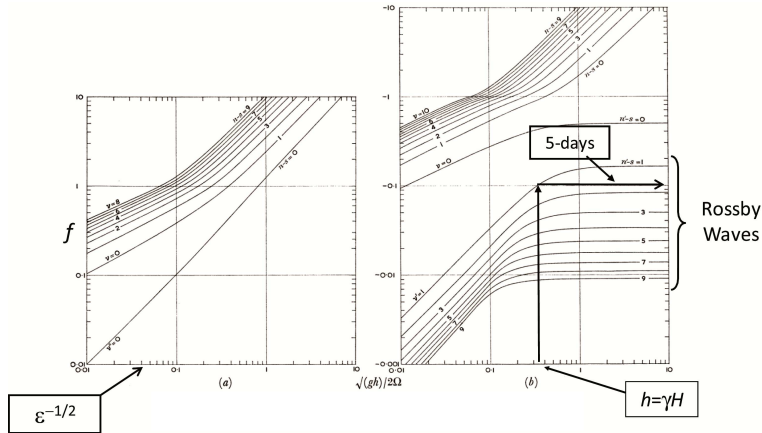


Fig. 15.12. An illustration of the process for determining eigenfrequencies for an $s=1$ westward propagating wave. Adapted from Figure 2 of Longuet-Higgins (1968).

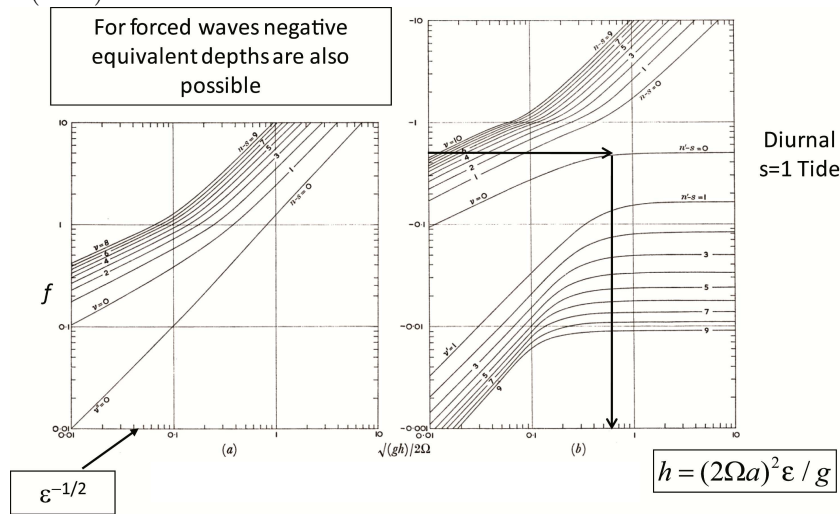


Fig. 15.13. Same as Figure 15.12 but for a forced wave. Rather than one equivalent depth and an infinite set of associated frequencies there is an infinite set of equivalent depths associated with a given frequency. Adapted from Figure 2 of Longuet-Higgins (1968).

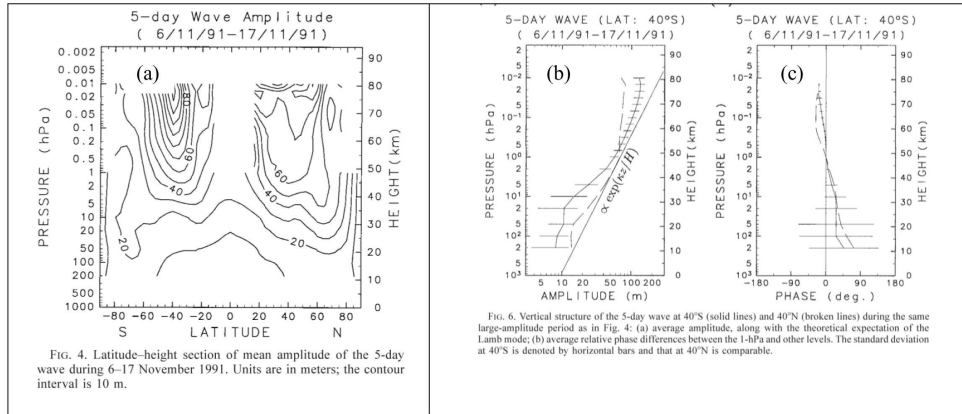


Fig. 15.14. The observed structure of the 5-day free wave in the terrestrial atmosphere 6-17 November 1991. Panel (a) shows the observed structure as a function of height (expressed as pressure) and latitude (from South to North poles). Panels (b) and (c) show the amplitude and phase, respectively, as function of height (pressure) at a latitude of 40°S. From Hirooka (2000).

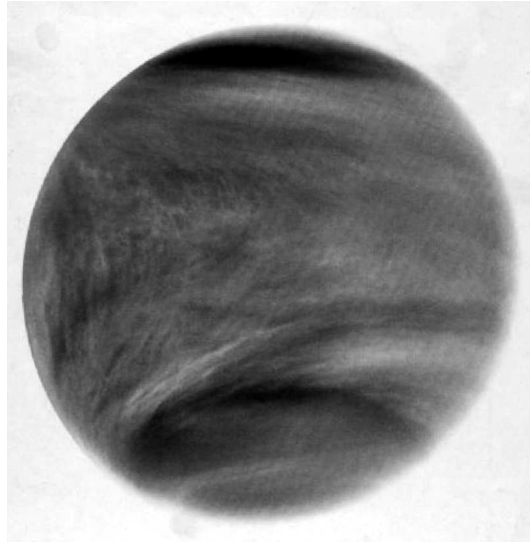


Fig. 15.15. The persistent “Y” pattern seen in UV images of the permanent cloud cover surrounding Venus. The pattern (on this negative image) appears as the ribbed structures that open to the left at low latitudes. The stem is oriented along the equator. These structures have been interpreted as Rossby waves. (Courtesy of G. Schubert, Department of Earth and Space Sciences, UCLA).

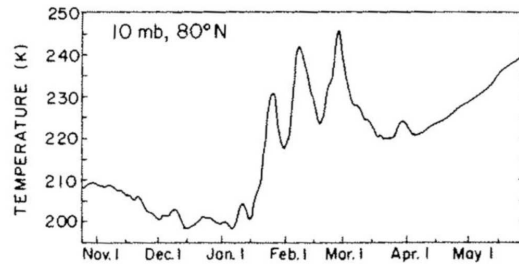


Fig. 15.16. Example of high-latitude warming (at 80°N) associated with stratospheric sudden warmings. The warming at 80°N rises from its midwinter value of ~ 200 K to ~ 245 K in a series of three events between mid January to early March before relaxing to a more typical temperature of ~ 225 K. From Andrews et al. (1987), after Gille and Lyjak (1984).

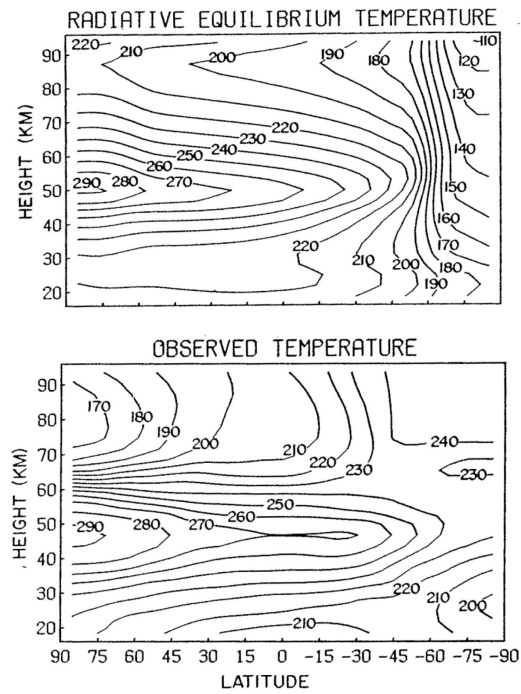


Fig. 15.17. Radiative-equilibrium (top) and observed (bottom) temperatures (K) in the stratosphere, mesosphere and lower thermosphere. The mesopause, the temperature minimum and transition between the mesosphere and thermosphere, is coldest during summer, opposite to what would obtain under radiative equilibrium. The upper panel shows the zonally-averaged temperature versus latitude and altitude calculated for radiative equilibrium and the lower panel shows the observed value during solstice. (From Wehrbein and Leovy, 1982)

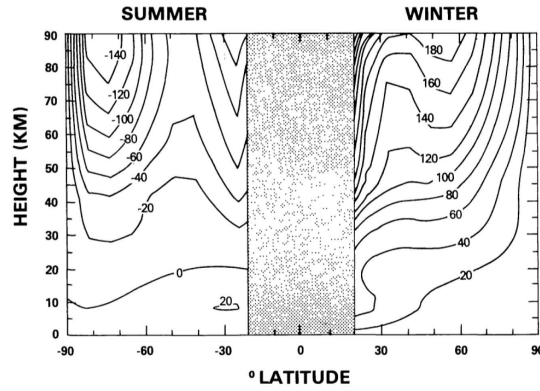


Fig. 15.18. Geostrophic mean zonal winds calculated from radiative equilibrium temperatures. Units are m s^{-1} . Eastward winds are positive. (From Geller, 1983)

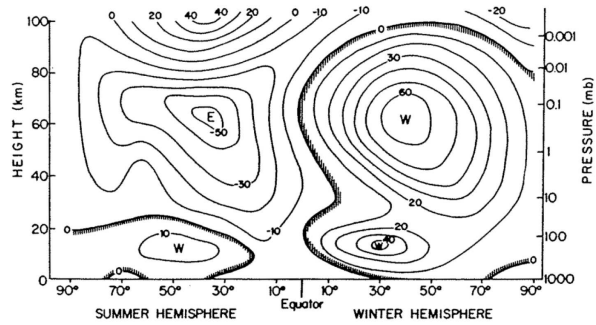


Fig. 15.19. Same as Figure 15.18 but for observed mean zonal winds. (From Andrews, 1987; courtesy R. J. Reed)

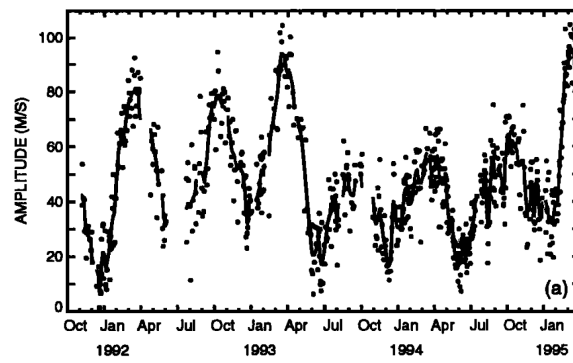


Fig. 15.20. Daily estimates of diurnal tidal wind amplitude from HRDI data for an altitude of 95 km. The data cover the period from October 1992 to March 1995. From Burrage et al. (1995)

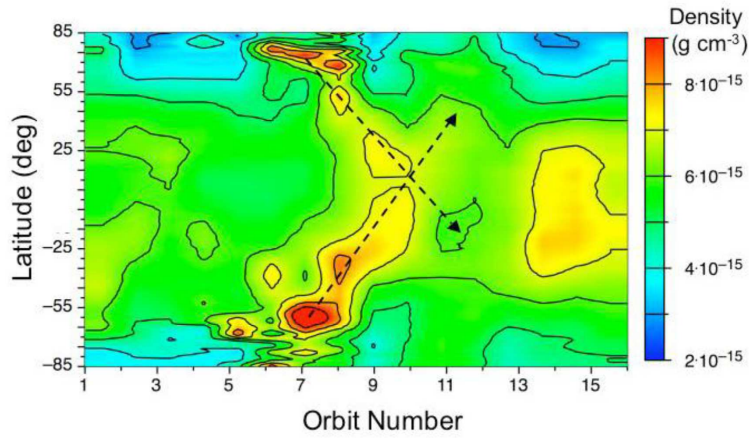


Fig. 15.21. An example of a traveling atmospheric disturbance seen in density near 400 km measured by the accelerometer on the CHAMP satellite in connection with a geomagnetic disturbance. The disturbances appear to penetrate into opposite hemispheres from their origins in the northern and southern hemisphere auroral zones. The simultaneous appearance in both hemispheres is due to conjugate activity. From Forbes (2007).

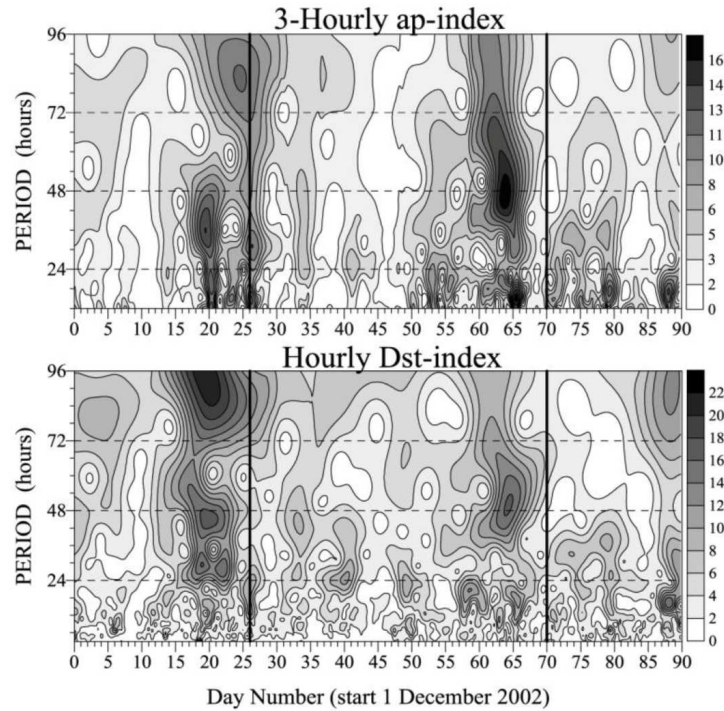


Fig. 15.22. A wavelet analysis of two indices of geomagnetic activity, ap and Dst. The figure shows wavelet amplitude as a function of frequency and day number. Around 20 days one sees the broad-band response to impulsive forcing due to geomagnetic disturbances with significant power near 2 days. The vertical solid dark lines at days 26 and 70 enclose the occurrence of a 2-d wave in the upper mesosphere and lower thermosphere (MLT); the ionospheric manifestation is seen as a series of wavelet power maxima near 48 h. (From Pancheva et al., 2006)

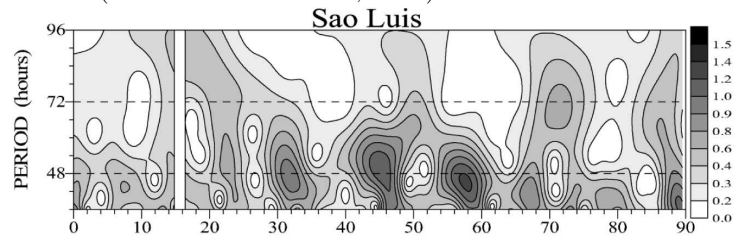


Fig. 15.23. A wavelet analysis similar to Figure 15.22 but for F_2 -region critical frequencies, f_0F_2 . (From Pancheva et al., 2006)

16

**Solar variability, climate, and atmospheric
photochemistry**

Guy P. Brasseur, Daniel Marsch, and Hauke Schmidt

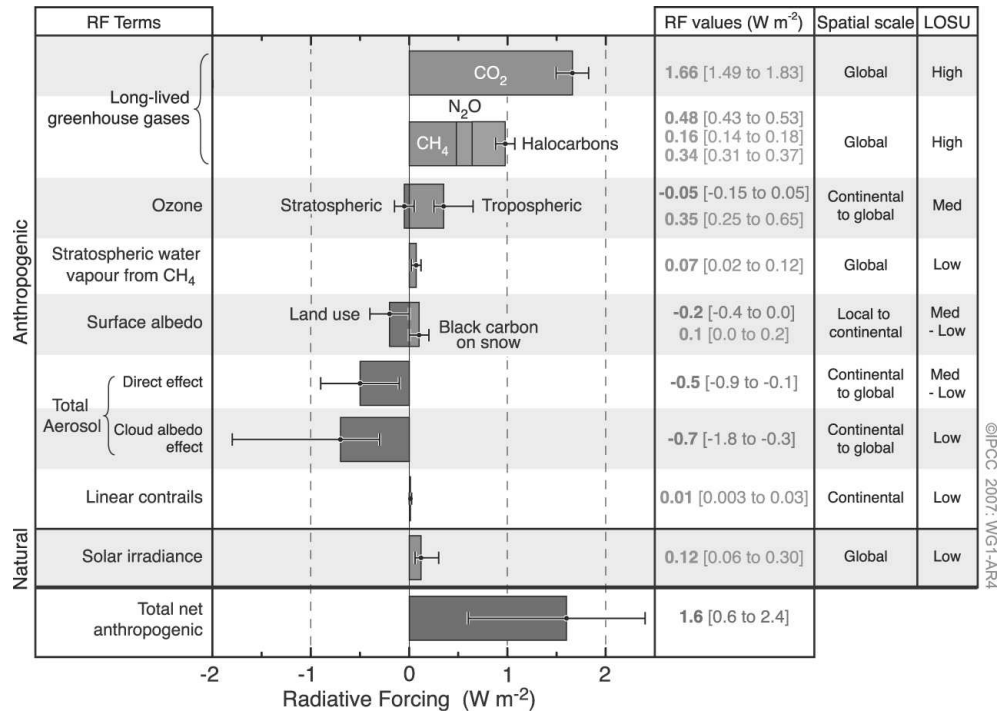


Fig. 16.1. Radiative forcing (RF, in $W m^{-2}$) relative to year 1750 associated with natural and anthropogenic changes in the atmosphere, as determined by IPCC (2008). The final column gives the IPCC's assessment of the level of scientific understanding (LOSU).

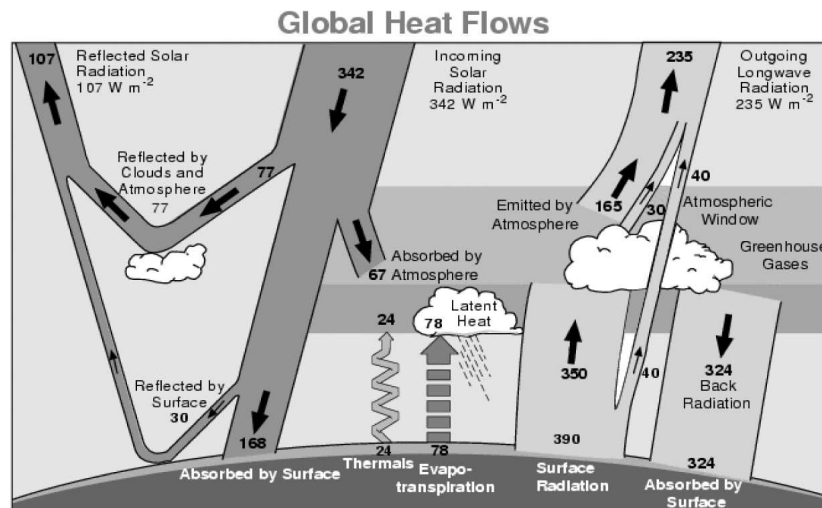


Fig. 16.2. Exchanges of solar (shortwave) and terrestrial (longwave) energy in the Earth's atmosphere. The flow of energy is expressed in Wm^{-2} , averaged over the entire Earth surface (i.e., averaged over the day-night cycle). From Kiehl and Trenberth (1987).

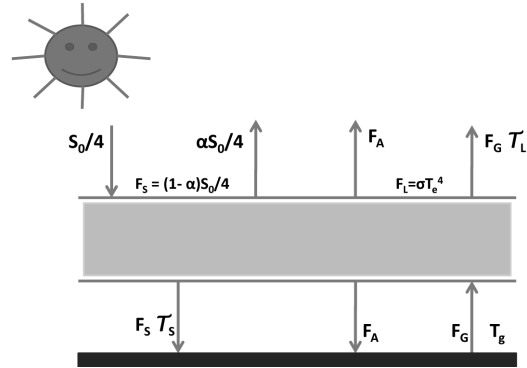


Fig. 16.3. Simplified model of radiative exchange in the Earth's atmosphere. The optical transmission in the atmosphere are represented by T_s in the shortwave (solar) spectral region and by T_L in the longwave (terrestrial) part of the spectrum.

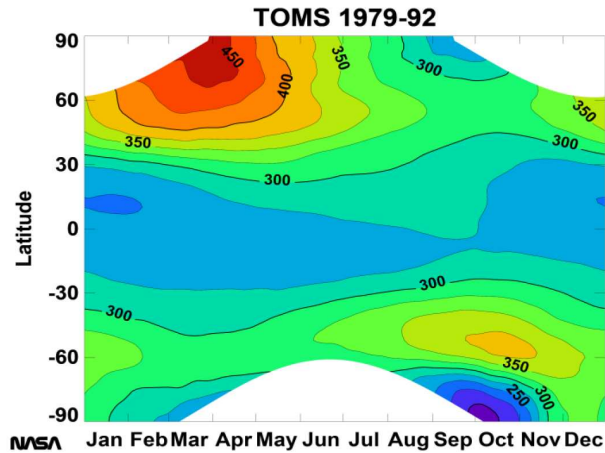


Fig. 16.4. Vertically integrated ozone concentration (expressed in Dobson units or DU; at 1 DU the column depth of ozone only would equal 10 microns at sea-level pressure and average temperature) represented as a function of latitude and month of the year. The distribution is established on the basis of observations made by the spaceborne TOMS instrument between 1972 and 1992. High values at the end of the winter are visible in the Arctic (March and April) and around 60°S in September and October. The presence of the Antarctic ozone hole is visible in the Antarctic in September-November. The value of 300 DU corresponds to an ozone layer of 3 mm under STP conditions. From NASA.

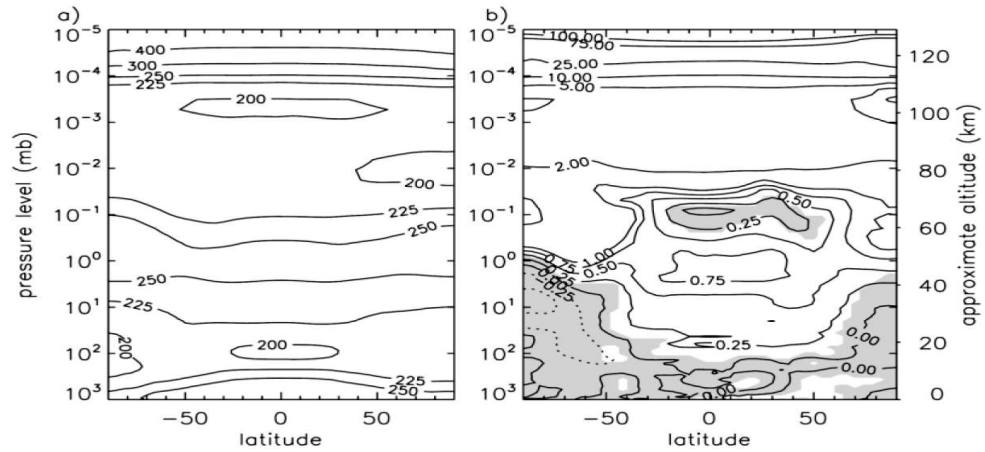


Fig. 16.5. Zonal mean distribution of the atmospheric temperature between the surface and approximately 130 km altitude (*left*) and response of temperature to the 11-y solar variability derived by the WACCM model (*right*). Units are in Kelvin. The shaded areas show areas where the calculated values are not significant. From Marsh et al. (2007).

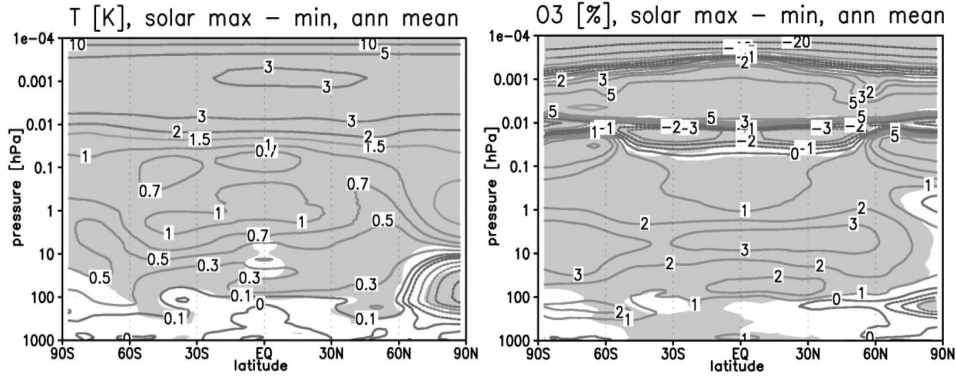


Fig. 16.6. Response of the atmospheric zonal mean, annual mean temperature (*left*; Kelvin) and the relative ozone variation (*right*; percent) to the 11-y solar cycle between the surface and approximately 110 km altitude as derived by the HAMMONIA model. Shaded areas correspond to regions where results are significant. After Schmidt et al. (2009).

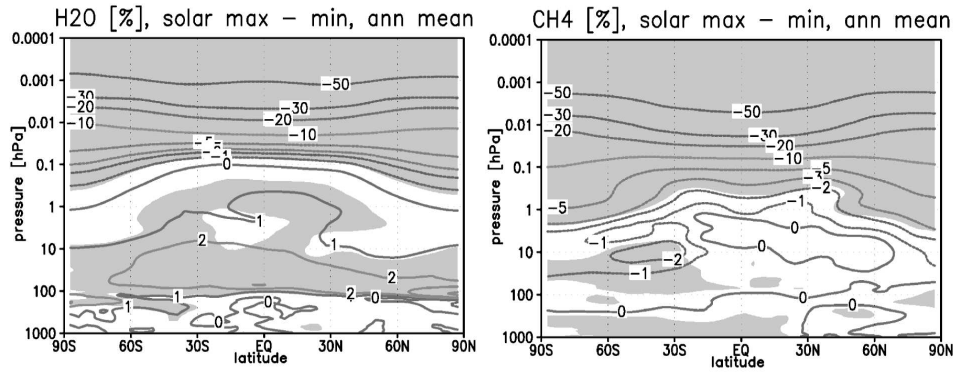


Fig. 16.7. Response of the atmospheric zonal mean, annual mean water vapor (*left*) and methane (*right*) concentration (percent) to the 11-y solar cycle between the surface and approximately 110 km altitude as derived by the HAMMONIA model. From the model of Schmidt et al. (2009).

SC Ozone Response, HALOE vs. Model

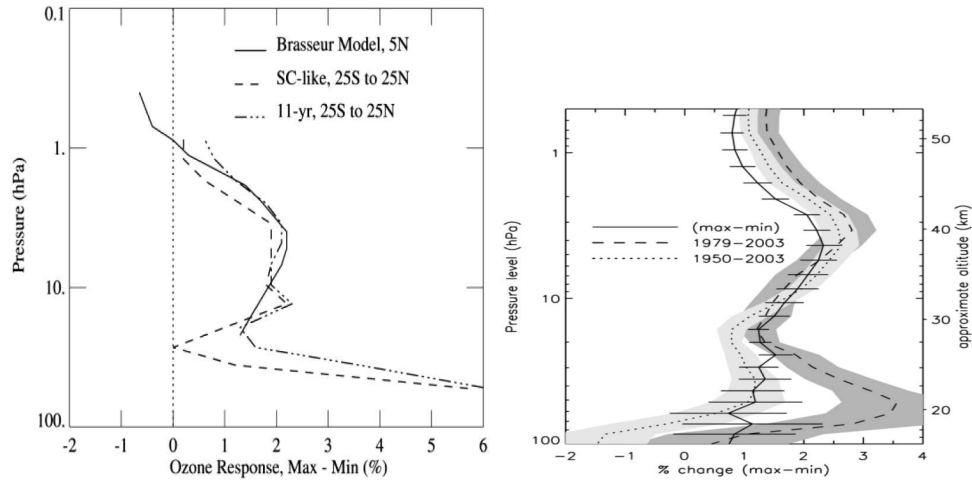


Fig. 16.8. *Left*: Comparison of calculated to observed ozone response (percent) in the stratosphere from minimum to maximum in the solar cycle. The data are retrieved from observations by the HALOE instrument on board UARS. From Remsberg (2008). *Right*: Percentage change in tropical ozone density between solar minimum and solar maximum conditions averaged between 24°S to 24°N. Solid line, with 2σ error bars, calculated from constant solar forcing “time slice” simulations. Lines with shaded regions are calculated using a multiple linear regression from the transient simulations of Garcia et al. (2007) for the time periods indicated. Shaded regions indicate 2σ errors in trend estimate. From Marsh et al. (2007).

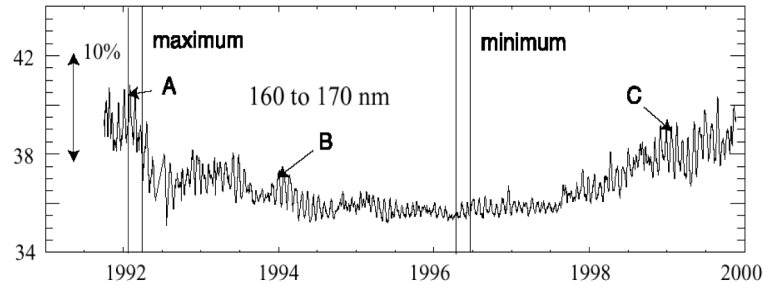


Fig. 16.9. Evolution of the solar irradiance (normalized intensity) at the top of the atmosphere in the spectral range 160–170 nm (Rottman, 2000). These measurements by the SOLSTICE instrument on board the Upper Atmosphere Research Satellite (UARS) highlight the variation associated with the 11-y solar cycle and with the 27-d synodic rotation of the Sun. Three periods of clear 27-day rotational modulation are marked by symbols A, B, and C. Pairs of vertical lines mark periods of solar maximum in early 1992 and solar minimum in 1996.

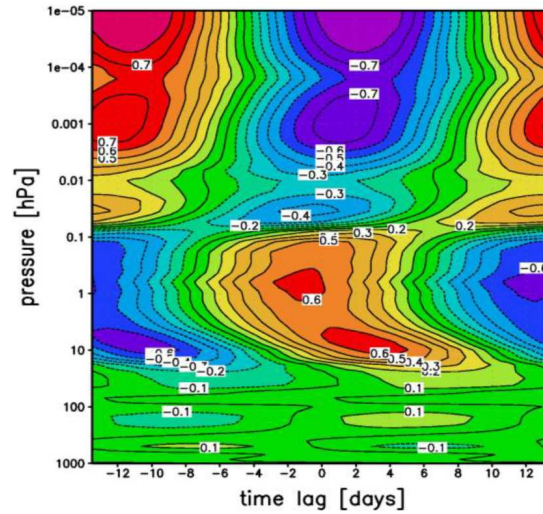


Fig. 16.10. Correlation coefficient between the ozone concentration and the 27-d solar variation as a function of atmospheric pressure [hPa] for different time lags [days] as calculated by the HAMMONIA model. One notes that, at 1 hPa (about 50 km altitude) for example, the highest correlation is found when ozone and solar radiation are in phase. At 10 hPa (about 30 km), the ozone signal with a 4-d phase lag is best correlated with the 27-d solar signal. Above 0.1 hPa (~ 65 km), the ozone signal appears to be out of phase with the solar periodic variation. From Gruzdev et al. (2009).

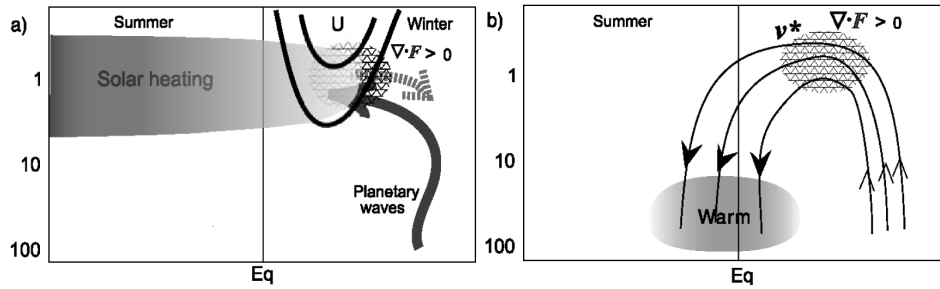


Fig. 16.11. Conceptual representation of a possible mechanism that links lower stratospheric variations in dynamical quantities with solar variability. Increased solar heating in the upper stratosphere, primarily in the summer hemisphere (highlighted on the left panel in dark gray), and consequently in the mean zonal wind (U), in the planetary wave propagation (arrow) and associated Eliassen-Palm flux (F) in the winter hemisphere tend to reduce the strength of the mean meridional (poleward) circulation with impacts on the zonal mean temperature structure. The small winter time "counter" meridional circulation associated with a solar-induced increase in stratospheric heating is represented in the right panel. Such disturbance (reduced upward motions in the tropics) should lead to a slight adiabatic warming of the lower equatorial tropopause. From Kodera and Kuroda (2002).

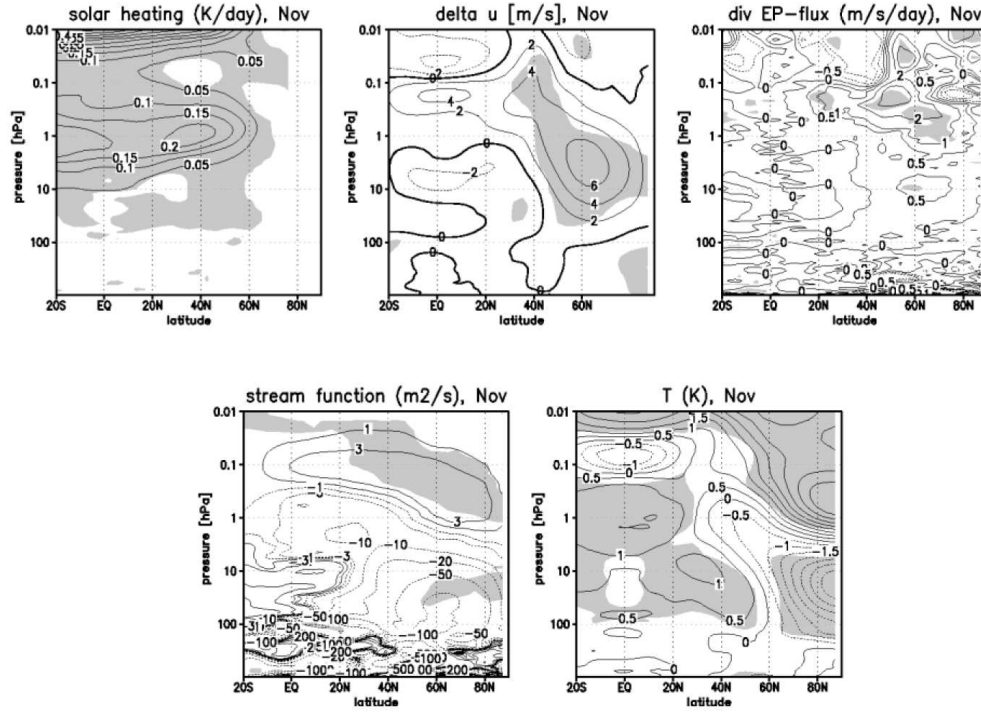


Fig. 16.12. Panels from the top left to the bottom right: Changes in the solar heating, mean zonal wind [m/s], Eliassen-Palm-Flux divergence (or momentum deposition from planetary scale waves) [m²/s] and temperature [K] during the month of November derived by the HAMMONIA model in response to increased solar irradiance from solar minimum to solar maximum conditions. Shaded areas show the regions in which the statistical significance exceeds 95%. From Schmidt et al. (2009).

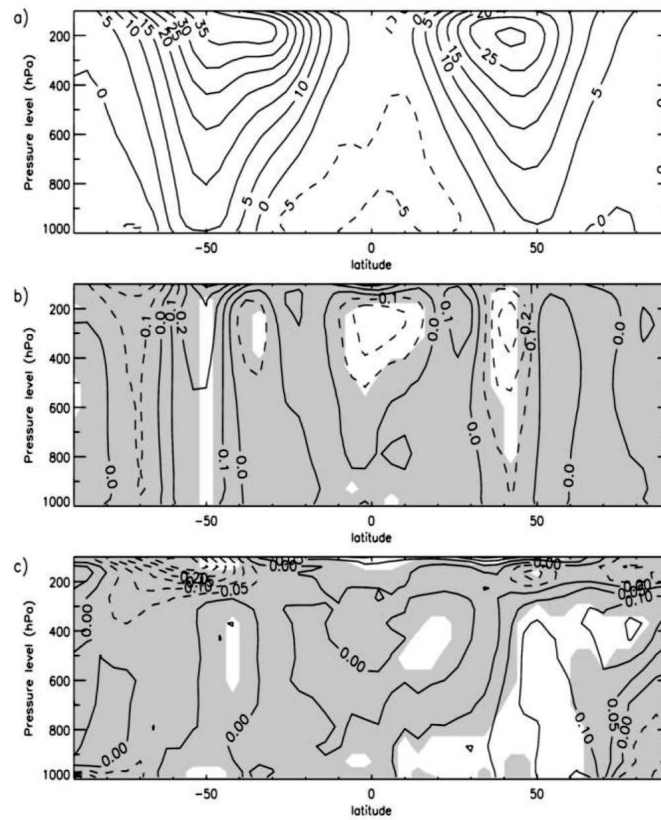


Fig. 16.13. *Top*: Tropospheric annually and zonally averaged zonal winds (m/s) for solar minimum conditions. *Lower panels*: Solar cycle changes (maximum-minimum) in annually and zonally averaged zonal winds (middle panel, in m/s) and zonal mean temperatures (bottom panel, in K). Unshaded regions are significant at the 95% level. From Marsh et al. (2007).

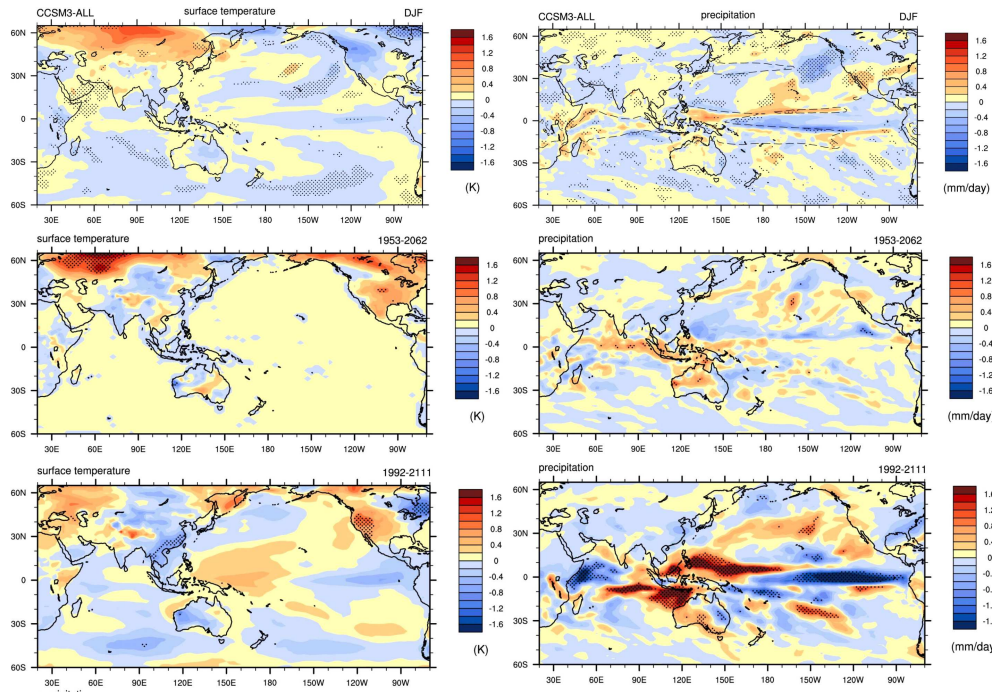


Fig. 16.14. Composites (*left*: temperature; *right*: precipitation) for simulated peaks in the 11-y solar cycle. Bottom-up coupled air-sea mechanism (*top panels*) and top-down stratospheric ozone mechanism (*middle panels*) are additive to strengthen convection in tropical Pacific and produce a stronger La Niña-like response to peaks in solar forcing (*bottom panels*). (From Meehl et al., 2009.)